TABLE OF CONTENTS

LIST OF TABLES

LIST OF FIGURES

XVIII

LIST OF ABBREVIATIONS

ARD	Automatic Relevance Determination
BC	Boundary Condition
CFD	Computational Fluid Dynamics
ESDU	Engineering Sciences Data Unit
GP	Gaussian Process
GPR	Gaussian Process Regression
LARCASE	Research Laboratory in Active Controls, Avionics and Aeroservoelasticity (*French*: Laboratoire de recherche en commande active, avionique et aéroservoélasticité)
LE	Leading Edge
MALE	Medium-Altitude Long-Endurance
MSL	Mean Sea Level
MUSCL	Monotonic Upwind Scheme for Conservation Laws
RANS	Reynolds-Averaged Navier-Stokes
RBF	Rational Basis Function
RQ	Rational Quadratic
RV	Random Variable
SE	Squared Exponential
SFC	Specific Fuel Consumption
SST	Shear Stress Transport

TCL/TK	Tool Command Language/Toolkit
UAV	Unmanned Aerial Vehicle
UGV	Unmanned Ground Vehicle
UUV	Unmanned Underwater Vehicle

LIST OF SYMBOLS AND UNITS OF MEASUREMENTS

A	Planar area
AR	Aspect ratio
b	Wing span
c	Chord length
$\bar{c}$	Mean aerodynamic chord length
C_D	Drag coefficient
C_l	Roll moment coefficient
C_L	Lift coefficient
C_L/C_D	Glide ratio
C_m	Pitching moment coefficient
C_n	Yaw moment coefficient
C_Y	Side force coefficient
D'	Drag force per unit span
D_ω	Cross-diffusion term
$\mathbb{E}$	Expectation
E_γ	Intermittency source term
f	Model response
$\mathbf{F}$	Body force
F_1	Blending function

g	Acceleration due to gravity
G_k	Production of turbulence kinetic energy
G_ω	Generation of specific turbulent dissipation
$\mathcal{GP}$	Gaussian distribution
i	Indexing term
I	Identity matrix
k	Turbulent kinetic energy
$k(\cdot, \cdot)$	Covariance function
K	Covariance matrix
L'	Lift force per unit span
m	Mass
$m(\cdot)$	Mean function
N	Number of data points
$\mathcal{N}$	Normal distribution
p	Pressure
P_γ	Intermittency source term
$P_{\theta t}$	Boundary layer momentum thickness source term
R	Range
Re	Reynolds number
Re_θ	Reynolds number based on boundary layer momentum thickness

$\widetilde{Re}_{\theta_t}$	Transition Reynolds number based on boundary layer momentum thickness
s	Standard error
S	Wing planar area
S_k	Turbulence kinetic energy source term
S_m	Rate of accumulation of mass in a fluid volume
S_ω	Specific turbulent dissipation source term
t	Time
$\bar{u}$	Mean component of velocity
u'	Fluctuating component of velocity
$\mathbf{u}$	Fluid velocity vector
V	Airspeed
W	Aircraft weight
$\mathbf{x}$	Input vector
$\hat{y}$	Predicted value in leave-one-out cross-validation
y^+	Nondimensional first cell wall distance
Y'	Spanwise side force
Y_k	Dissipation of turbulence kinetic energy
Y_ω	Dissipation of specific turbulent dissipation rate
α	Angle of attack
α_{RQ}	Scaling parameter in the rational quadratic kernel

γ	Intermittency
Γ	Gamma function
δ	Amplitude of displacement
δ_{ij}	Kronecker delta
∂	Partial derivative
ε	Turbulent dissipation
η	Propeller efficiency
θ	Boundary layer momentum thickness
θ	Twist angle
$\boldsymbol{\theta}$	Hyperparameter vector
λ	Taper ratio
λ_i	Length scale for parameter i
Λ	Sweep angle
μ	Dynamic viscosity
$\boldsymbol{\mu}$	Mean vector
μ_*	Predicted mean
μ_t	Eddy viscosity
ν	Degrees of freedom of a Matérn kernel
ρ	Fluid density
σ	Shear stress

σ_f	Scale factor
σ_n	Noise variance
σ_m	Individual length scale
Σ_*	Expected variance
$\bar{\bar{\tau}}$	Deviatoric stress tensor
ϕ	Standard normal cumulative density function
Φ	Standard normal probability density function
ω_f	Specific dissipation rate

INTRODUCTION

Over the past few decades, unmanned systems have been a key addition to military forces (Quintana, 2008). Unmanned aerial vehicles (UAV) constitute an important slice of the unmanned defense sector, having shown significant potential to strengthen the abilities of troops often by performing dangerous or repetitive tasks. The land- and water-based counterparts of UAVs, unmanned ground vehicles (UGVs) and unmanned underwater vehicles (UUV), are also important fields studied in unmanned robotics that have developed alongside UAVs.

The Hydra Technologies S45 Bàalam, a tactical surveillance and reconnaissance UAV, is used by the Research Laboratory in Active Controls, Avionics and Aeroservoelasticity (LARCASE) as part of a collaboration with Hydra Technologies with the aim of advancing knowledge on the design of fixed-wing UAVs of this category. Figures 0.1 and 0.2 show the top and side views of the Hydra S45 Bàalam, respectively. A fuselage pod houses surveillance equipment which makes up most of the payload, as well as two heavy-fuel two-stroke piston engines (6 HP front and 4.5 HP aft), each engine driving a two-bladed propeller (Munson, 2015). The modular design is advantageous for aerospace research activities in that components can be replaced with experimental designs easily. In the case of redesigned wings, the original wing can be removed from the shoulder-mounting slot and substituted for a new test wing.

Aerodynamic efficiency is critical in the performance of an aircraft because it directly impacts its range and endurance capabilities while determining fuel consumption and pollutant emissions (Mueller & DeLaurier, 2003). Trade-offs are necessary among the different requirements for high endurance and range at various design points of the flight envelope of the aircraft.

The purpose of the work presented in this thesis is to assess the potential benefits from three methods tested for improving the aerodynamic efficiency of a medium-altitude long-endurance (MALE) UAV wing. These three aerodynamic performance improvement methods investigated in this work are the following:

2

a.   Impact of a detachable blended winglet,

b.   Redesign of a three-dimensional base wing on a global level, and

c.   Morphing aptitudes that can change the airfoil shape in flight.
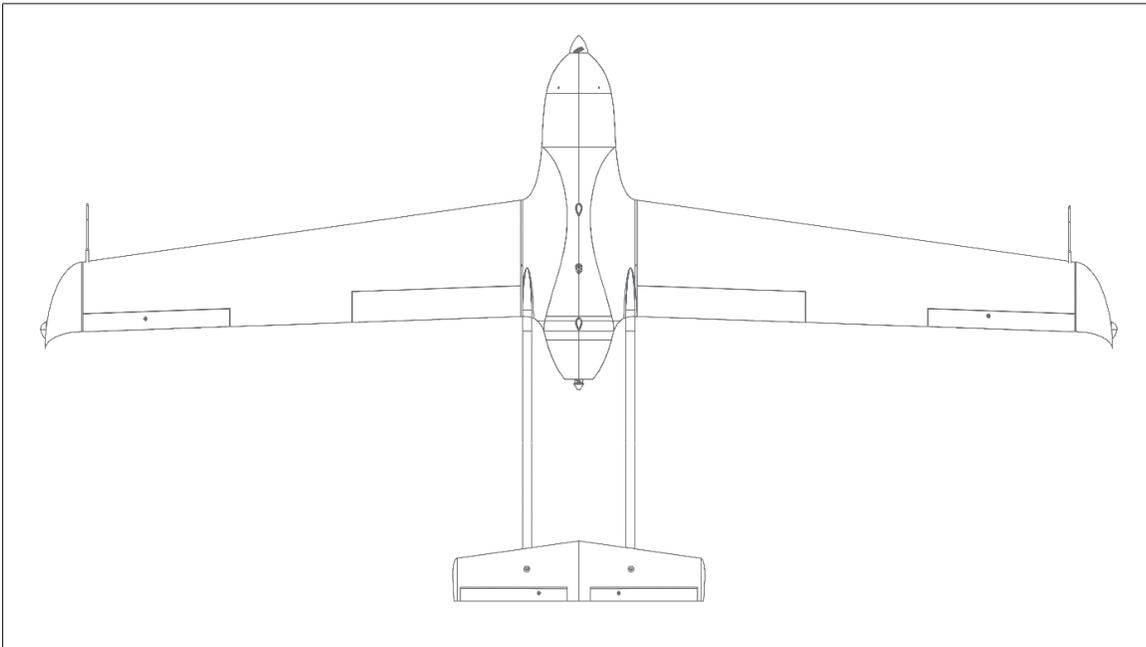
Figure 0.1   Top view of the Hydra S45 Bàalam
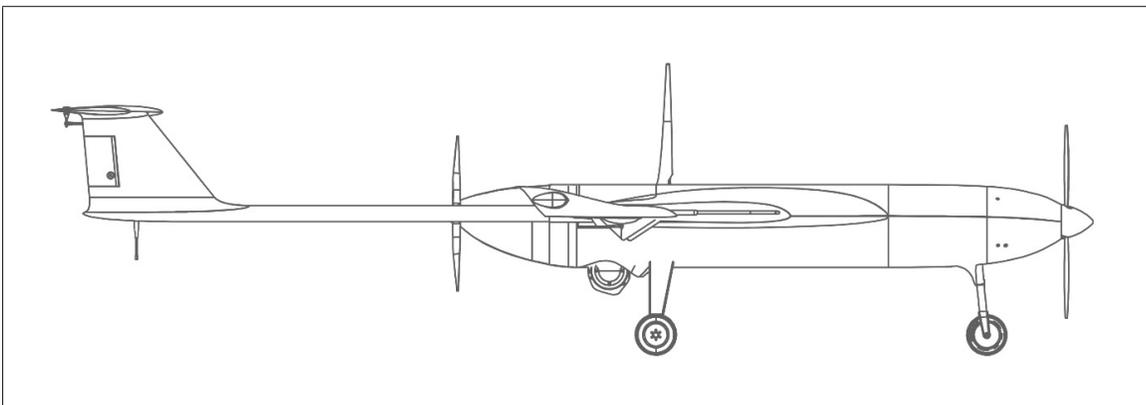
Figure 0.2   Side view of the Hydra S45 Bàalam

The baseline performance of the wing on the Hydra S45 Bàalam is first established so that comparisons can be made. Two types of design modifications for improving wing performance are then studied. Simulation-driven aerodynamic design optimization is used to perform surrogate-based modeling and optimization using Bayesian inference with high-fidelity results.

Chapter 1 gives a literature review to contextualize the work in this thesis. Chapter 2 provides the theoretical background needed to understand subsequent chapters. Chapter 3 presents a detailed analysis of the Hydra S45 Bàalam wing, which includes a study of the impact of the upswept blended winglet on this original wing. A parametrization method tailored to the design of the UAV is proposed in Chapter 4, then used to optimize both its range and endurance. In Chapter 5, the same optimization technique used in Chapter 4 is applied to a morphing wing in which the morphing process is represented through the use of sinusoidal displacements.

CHAPTER 1

BACKGROUND AND LITERATURE REVIEW

This chapter deals with past published works related to the objectives of the present work. A broad-brush summary and discussion of three-dimensional computational aerodynamics, optimization techniques, and surrogate-based modeling are given to provide context and rationale for the choices made in using the selected approaches. Major caveats against the approaches discussed are expressly mentioned. Published literature on the performance of wings in subsonic flow as well as those with morphing capabilities is also put forward so that comparisons of results can be made in later chapters.

1.1 3D Computational Aerodynamics

Computational fluid dynamics originated in the 1950s for the development of weapons (Edwards, 2012). Advancements in digital computing allowed the computation of fluid flows using panel methods from the 1960s. With Moore's law (Moore, 1998) proposed in 1965 and holding for most of the 20th century, computational power has significantly increased over the years, roughly doubling every two years. Such a trend has encouraged the development of computational flow solvers of increasing complexity and fidelity, particularly for aerospace design and development. The discussion in the following subsections is limited to methods applicable to three-dimensional geometries, although methods applicable to two-dimensional geometries such as airfoils also exist.

1.1.1 Lifting line theory

Lifting line theory was first proposed independently by Frederick Lanchester in 1909 and Ludwig Prandtl in 1918 (Von Kármán, 2004). The classical formulation provided a quantitative model for calculating the inviscid forces on a 3D wing. With time, this formulation has been extended to cover a broader range of applications including complex wing geometries, viscous flows and nonlinear effects such as turbulence.

In lifting line theory, a wing is represented by a series of finite vortex lines along the quarter-chord line, each of which sheds a downstream vortex. This representation is permissible through the circulation theory, also known as the Kutta-Joukowski theorem, which expresses the lift generated by an airfoil as a function of the fluid density, freestream fluid velocity, and circulation (Clancy, 1975).

The main limitations of lifting line theory are the neglect of viscous effects, the inability to model unsteady flows, the lack of availability of the aerodynamic moments, and the limitation to high aspect ratio wings. While viscous corrections can be applied to account for boundary layer physics, these corrections are generally based on empirical or semi-empirical models, which are not guaranteed to be fully reliable. The collapse of the lift distribution onto a line makes the computation of aerodynamic moments infeasible. Compressibility effects can be taken into account through the Prandtl-Glauert transformation (Chattot & Hafez, 2015).

1.1.2   Lifting surface theory

Lifting surface theory, or vortex-lattice method, closely resembles lifting line theory in that the wing is also represented by a system of discrete line vortices (McBain, 2012). The wing is represented by discrete vortex segments in both the spanwise and chordwise directions, making up a mesh-like lattice of horseshoe vortices (Lamar & Margason, 1971; Johnson, 1972; Katz & Plotkin, 2001). Matrix representation of the vortex strengths ensues from the array of vortices, such that Newton's method is often used to solve the system of equations.

The limitations of lifting surface theory are the same as those of lifting line theory, with the exception that moments can be computed with lifting surface theory because of the availability of chordwise information. The increased complexity relative to lifting surface theory introduces a slight additional cost in terms of computational requirements. The unsteady vortex-lattice method is an extension that can take into consideration non-stationary effects for a broader range of application (Simpson *et al.*, 2013).

1.1.3 Panel methods

As the previous two methods, panel methods are potential flow methods. Panel methods are used to determine the velocity distribution around a body submerged in a fluid, from which a pressure distribution can be inferred and integrated to compute the inviscid hydrodynamic moments and forces (Moran, 1984; McCormick, 1995). Singularities (point sources, sinks, vortices, doublets) are used to represent the boundaries of the body and the wake formation (Anderson Jr, 2010).

Modeling of the boundary layer and flow separation are only possible by coupling the inviscid potential flow solver with a boundary layer solver. Boundary layer treatment is most often based on the solution to the attached boundary layer problem, such that flow separation tends to be poorly modeled. Most panel methods are also limited to subsonic flows, although transonic (Oskam, 1985) and supersonic (Ehlers *et al.*, 1979) variants exist.

Panel methods can be complex to set up in that three-dimensional grids are required, increasing modeling difficulty. High-order panel methods which produce more accurate solutions relative to low-order methods for the same number of panels are very sensitive to gaps in surface paneling (Katz & Plotkin, 2001). The modeling complexity at the geometry generation level, wake model dependence, and poor flow separation prediction capabilities make panel methods useful in the conceptual design phase but less lucrative in the preliminary and advanced design phases.

1.1.4 Navier-Stokes solvers

Navier-Stokes solvers, based on the Navier-Stokes equations, now dominate in the field of high-fidelity computational aerodynamics. In this approach, equations for the conservation of mass, momentum, and energy are solved to satisfy the laws of physics (Galdi, 2011). Solvers based on the Euler equations, which are the Navier-Stokes formulation for a fluid with no viscosity (Elger & Roberson, 2013), were favoured in the early 1980s. The subsequent popularity of the discretized Navier-Stokes equations solved numerically was attributable to advances in

computational mathematics, which include convergence acceleration, vector and parallelized computing, grid adaptation techniques, and high-performance computing using clusters.

Because of the complex nature of the Navier-Stokes equations, several classes of solutions have evolved from them. Direct numerical simulations, for which the discretized Navier-Stokes equations are solved directly, are the most computationally expensive as they require the resolution of all scales of turbulences up to the finest ones known as the Kolmogorov microscales (Moin & Mahesh, 1998). The number of floating-point operations grows as the cube of the Reynolds number (Re), making the computational cost far too high for practical applications not related to turbulence research.

Large eddy simulations are less expensive computationally relative to direct numerical simulations. As the name suggests, large eddies, which are dynamically influential, are resolved in this type of simulation. The remaining smaller eddies are modeled rather than resolved to reduce the computational cost significantly. However, massively parallel computing is still required per evaluation. Vortices and acoustic waves are calculated, making the solutions well-suited for flow studies involving acoustics, multiphase flows, reactive flows (Pitsch, 2006) and fluid-structure interactions (Münsch & Breuer, 2011).

Reynolds-averaged Navier-Stokes (RANS) solvers reduce computational requirements even further than large eddy solvers by modeling all scales of turbulence. Over a hundred models have been proposed, each tailored to a particular type of flow (Leschziner, 2010). Commonly used turbulence models in aerospace include the k-ε and k-ω models (or a blend thereof), which are linear eddy-viscosity models in that they are based on the Boussinesq hypothesis (Hinze, 1975) which introduces the concept of eddy viscosity as a flow variable to partly alleviate the process of modeling turbulence.

In terms of memory requirements, direct numerical simulations and large eddy simulations are best conducted on computer clusters. RANS simulations, however, can be run on high-end desktop computer to a certain limit determined by the mesh density, the number format of the solution (single or double precision) and the order of solution.

1.1.5 Lattice Boltzmann method

The Lattice Boltzmann equation (Chen & Doolen, 1998) is an alternative to the Navier-Stokes equations for simulating fluids in motion by using statistical mechanics. The continuous Boltzmann equation describes the evolution of particle properties, namely mass and energy, using probability distribution functions. In the Lattice Boltzmann method, this equation is discretized and applied at the nodes of a lattice representing particles. Motion is interpreted as a streaming process followed by a collision process. In the continuum limit, a Chapman-Enskog expansion links lattice variables to macroscopic flow variables, leading to the recovery of the incompressible form of the Navier-Stokes equation (Succi, 2001).

In relation to aerospace applications, high-fidelity solutions for icing applications have been obtained successfully on airfoils using Lattice Boltzmann solvers (König *et al.*, 2015) and with multiphase flows (Luo, 2000). For complex three-dimensional flows, Lattice Boltzmann solutions are possible, albeit impractical. Drawbacks include tricky boundary conditions, limited gridding schemes, and the difficulty in taking curvature into account. While Lattice Boltzmann techniques appear to have very promising potential, more advancements are needed in the field to increase the practical relevance of the method. Research-oriented open-source codes such as OpenLB (Heuveline & Latt, 2007) and Palabos (Latt) are currently more widespread than commercial codes.

1.1.6 Conclusion on aerodynamic solvers

From the discussions in the previous subsections on the various methods for advanced three-dimensional aerodynamic calculations, it is deemed that the most tenable approach for modeling the Hydra S45 Bàalam wing is through the Reynolds-averaged Navier-Stokes equations, both for benchmarking its performance and for optimization processes. They are capable of providing the highest accuracy and most detailed solutions for an associated reasonable computational cost based on knowledge of the computing resources available at the LARCASE and the time frame of the thesis. The development of an advanced RANS CFD tool is also desirable

for use in conjunction with computational structural dynamics for future in-depth aeroelastic studies (Beckert, 2000). More computationally demanding techniques would be prohibitively expensive to provide a level of detail in the simulations that is only partly relevant to the study of external aerodynamics.

1.2 Optimization Techniques

Single-objective optimization problems are generally presented in a standard form as outlined in Equation (1.1). The objective function f, which is to be minimized, depends on a vector of parameters $\mathbf{x}$. In a constrained optimization problem, inequality constraints $g_j(\mathbf{x})$ and/or equality constraints $h_k(\mathbf{x})$ can be applied to place limits on the design space. Design variables tend to have ranges expressed as lower and upper optimization bounds written as $\mathbf{x}_{iL}$ and $\mathbf{x}_{iU}$.

$$
\begin{aligned}
&\text{Minimize: } f(\mathbf{x}) \\
&\text{Subject to: } g_j(\mathbf{x}) \leq 0 \qquad j = 1, m \\
&\qquad\qquad\quad h_k(\mathbf{x}) = 0 \qquad k = 1, p \\
&\qquad\qquad\quad x_{iL} \leq x_i \leq x_{iU} \quad i = 1, n
\end{aligned}
\tag{1.1}
$$

Optimization algorithms can be classified into two main classes, local and global. The primary intent of this classification is to distinguish the effectiveness of algorithms in dealing with multimodal objectives, as is discussed in the subsections that follow.

1.2.1 Local optimization algorithms

Local optimization algorithms are, for the most part, gradient-based methods. They can solve multidimensional problems efficiently with minimal tuning. These algorithms usually have an iterative two-step process of finding a search direction then advancing in that direction until no more improvement can be found (Govan, 2006).

A major disadvantage of local optimization algorithms is their reliance on gradient information. Gradients can be expensive to compute, assuming they exist and are continuous everywhere. Finite difference methods are often used to calculate gradients, which only provide approximations for the partial derivatives of f. On some occasions, such as in the case of linear finite element analysis solvers, gradient information can be obtained directly, drastically reducing the time associated with gradient computation while also increasing the accuracy of those gradients. Gradient-free local optimization methods also exist, and include Powell's algorithms, coordinate descent and the Nelder-Mead method (Conn *et al.*, 2009).

1.2.2 Global optimization algorithms

Global optimization methods are particularly appropriate when f may have multiple local optima. If a local algorithm is in the neighbourhood of a local minimum different from the global minimum, it will converge to that local minimum instead of the sought-after global minimum (Floudas *et al.*, 2013).

Evolutionary algorithms constitute a large portion of global optimization algorithms and are heuristic/metaheuristic algorithms. Genetic and particle swarm algorithms are commonly used in engineering optimization. Genetic algorithms begin by establishing the fitness of a population of design points, selecting the best of those design points, and creating a new generation through a cross-over process in which attributes of the best design points are mixed. Particle swarm methods share many similarities with genetic algorithms in the way that they operate. However, information is propagated in a different manner: only the global best value influences the other members of the swarm. Overall, evolutionary algorithms have a high computational cost (because of the large number of evaluations required), handle constraints with difficulty, and require problem-dependent tuning (Back, 1996).

Alternatively, deterministic and stochastic approaches can be used in global optimization. Deterministic methods focus on guaranteeing that the reported optimum is genuinely the global

one. Stochastic methods make use of random variables to perform function minimization in the presence of randomness such as noise.

A last interesting approach is using the response surface methodology. Relationships between design variables and response variables are investigated and statistically described to obtain an approximative statistical model of how response variables behave, effectively creating response surfaces using a set of parameter combinations with known responses.

1.2.3 Conclusion on optimization techniques

In § 1.1.6, it was established that a Reynolds-averaged Navier-Stokes approach would be the most effective in the context of this thesis. Minimizing an objective function evaluated using this moderately expensive technique can only be achieved if a reasonably low number of function evaluations is required. The nature of f is also often not well known: it is not known beforehand whether f is continuous, or if it is unimodal or multimodal. A response surface approach built on Bayesian statistics is presented in the next section because this approach is deemed to offer the most flexibility to leverage high-fidelity data.

1.3 Surrogate-Based Modeling

Simulation-driven engineering has had an increasingly large share of the engineering design process over the last two decades with advances in computing capabilities. Optimization methods applied to lengthy simulations tend to require an inordinate amount of time, which has prompted the development of surrogate modeling (Koziel & Leifsson, 2013). Mathematical approximations are used to estimate the unknown response f of a system for a combination of design variables from known behaviour.

The strength of surrogate models lies in their ability to handle the implicitness of f in that f is treated as a black-box function. The mapping between design variables and responses is viewed as a black box to be characterized (Forrester *et al.*, 2008). The availability of a quick

predictive model is particularly handy when more than one output or optimization result is of interest.

The simplest surrogates are built using polynomial schemes, for which a first order polynomial is equivalent to linear regression. The polynomial consists of a summed series of terms in the design variables weighted by coefficients estimated using a least squares approach. Polynomial surrogates are very prone to overfitting which may introduce artificial oscillations of the response surface, particularly when high-order terms are used. Higher-order polynomials have a greater the number of weights to be estimated; because more samples than weights are needed to determine these weights, a sufficiently large number of samples is necessary (Stein, 2012).

Radial basis functions are an alternative to polynomials to construct surrogates. Functions are used instead of polynomials to estimate f. Artificial neural networks and Gaussian process regression (GPR, or Kriging) are popular algorithms that are built upon radial basis functions. Such methods require hyperparameter tuning, which can be difficult. When hyperparameter tuning for basis function methods is achieved using maximum likelihood theory, the resulting model is called a maximum likelihood scheme (Rasmussen & Williams, 2004).

Artificial neural networks are parametric models while Gaussian process models are non-parametric. In non-parametric models, the model structure is not predefined: parameters can be infinite in number and increase with the number of data points (Härdle, 1990). Non-parametric models perform better in the presence of outliers and non-linearities. Covariance-learning is a strength of all Kriging algorithms, although the use of covariance matrices is a restriction on the maximum size of the data set because of operations such as matrix inversion (Wang, 2016). Training a Gaussian process model generally requires more time relative to an artificial neural network, but is often capable of yielding a more accurate surrogate (Kocijan & Petelin, 2011).

In conclusion, Gaussian process models are chosen to develop surrogate models in subsequent chapters because they appear to provide more flexibility for working with results obtained through numerical simulations, which are inherently affected by numerical errors.

1.4 Subsonic Aerodynamic Performance of Aircraft Wings

It is useful, at this point, to consider the usual practices in wing design and existing knowledge on the behaviour of aircraft wings in incompressible flows. Wings generate most, if not all, of the lift, to sustain flight. The significant amount of drag associated with lift production has made wing design a primary focus in aircraft design: according to a study focusing on a similar-sized MALE UAV by Panagiotou *et al.* (2014), the contribution of the wing to the total aircraft drag is around 40 % during loiter, and ranges between 30 % and 70 % during other phases of flight, depending on the angle of attack. The impact of key design parameters and winglets is examined in this section, and relevant measures of merit are stated. Research in morphing wing aerodynamics is discussed in the final portion of this section.

1.4.1 Geometric parameters

Four parameters that influence the design of a wing are explored in the following subsections. Aspect ratio, taper ratio, and sweep angle describe the planform, while the twist angle impacts the cross-section of the wing. Another parameter, the dihedral angle, is not included as it is primarily concerned with lateral stability; it is best left to a later phase of the design. Additionally, dihedral effects can be mitigated by manipulating the position of the wing relative to the aircraft centre of gravity.

1.4.1.1 Aspect ratio

The wing aspect ratio is the ratio of its span to its mean chord, and is a measure of how stretched or slender a wing is. An equivalent alternative expresses the aspect ratio as the ratio of the squared span to the wing area (Torenbeek, 2013). Sóbester & Forrester (2014) briefly argue that, based on the Lanchester-Prandtl lifting line theory, the aspect ratio is representative of the reciprocal induced drag. This inverse relationship exists because more stretched wings produce weaker tip vortices, leading to lower induced drag. Nicolai & Carichner (2001) add that the zero-lift drag coefficient, which is deemed a constant component of the total drag, is

only slightly impacted by the aspect ratio since most of the drag on the wing is skin friction drag. Low aspect ratio wings are structurally more efficient owing to the shorter moment arms for a given load, resulting in smaller bending moments.

1.4.1.2 Taper ratio

The taper ratio is the ratio of the tip chord to the root chord. A delta wing is obtained for a taper ratio of zero, while a rectangular wing is obtained for a taper ratio of one. It is known that a near-elliptical lift distribution is obtained for a taper ratio of 0.35 (Nicolai & Carichner, 2001). The high interest in achieving an elliptical lift distribution stems from the knowledge that minimum induced drag is obtained at this condition (Munk, 1923; Jones, 1950). Beyond its use in tailoring the lift distribution, wing taper can be used to shift the load distribution towards the wing root to reduce moments to be sustained and thus the weight of the wing (Sóbester & Forrester, 2014).

1.4.1.3 Sweep angle

Wing sweep is a feature in which a wing is angled relative to the longitudinal axis. Sweep angle can be defined as a measure of leading-edge sweep or of quarter-chord sweep, or otherwise, depending on the choice of definition. It does not have a high impact on aerodynamics in the low subsonic regime, and has more often found use in transonic and supersonic applications to delay shock wave formation. Aft sweep can be used to improve the contribution of the wing to directional stability (Sóbester & Forrester, 2014). Forward sweep presents an advantage in its tendency to stall the inboard portion of the wing first (Torenbeek, 2013), preserving aileron functionality and allowing recovery. However, forward sweep suffers from aeroelastic divergence, in which the local angle of attack increases from the wing root to the wing tip owing to elastic twist (Nicolai & Carichner, 2001). Wing sweep heavily impacts the position of the aerodynamic centre of the aircraft, which in turn impacts the bending moment and thus the structural weight.

1.4.1.4 Twist angle

Wing twist is a means of increasing the local lift on a chosen section of the wing. Two types of twist exist, geometric twist and aerodynamic twist. Geometric twist is achieved through a rotation of the local airfoil cross-section, usually about the quarter-chord point. In contrast, aerodynamic twist is achieved by changing airfoil section properties such as thickness or camber along the span (Kuethe & Chow, 1997). Wing twist inherently improves the stall characteristics of a wing, as the wing becomes more likely to stall root first (Sóbester & Forrester, 2014). Linear twist, particularly geometric twist, is most commonly used for ease of manufacturing.

1.4.2 Winglets

Winglets are wingtip devices used on fixed-wing aircraft to reduce the drag contribution of wingtip vortices. Total drag on a three-dimensional body comprises parasite drag and induced drag. For a flying wing in a low-speed subsonic regime, the parasite drag sources are only skin friction drag and pressure drag, which, together, are also called the profile drag. Winglets target induced drag due to tip vortices in particular. Tip vortices are a result of flow leakage at the wing tips. A pressure imbalance between the upper and lower surfaces of the wing is set up because the flow is deflected inwardly on the upper surface, or pressure side, and outwardly on the lower surface, or suction side, leading to the formation of a vortex (McLean, 2012). This pressure difference, while necessary for the generation of lift, also causes air from the suction side to flow to the pressure side, thereby reducing the effective angle of attack. The lift vector becomes tilted, giving rise to a force component in the opposite direction of the flow called the induced drag (Anderson Jr, 2010).

Research on wingtip devices began in the 1970s at NASA with the experimental testing of end plates to reduce the intensity of tip vortices (Hemke, 1928; Mangler, 1938) before modern-day winglets. Whitcomb (1976, 1981) pioneered winglet research by proposing and publishing results for his designs, in which he defined geometric parameters to characterize winglet shape,

such as cant, taper, sweep, and toe-out angle. Promptly after Whitcomb's propositions, Heyson *et al.* (1977) used a vortex lattice method to conduct a parametric study on winglet performance, where they established that, for a given increase in bending moment, a greater reduction in induced drag could be achieved by using a winglet rather than extending the wing tip. They concluded that winglets provide the highest improvement for near-vertical geometries and for high wing loadings near the wing tip.

As the technology readiness level of winglets evolved, numerous patents were filed for novel concepts aimed at wingtip vortex intensity reduction. These patents include blended winglets to eliminate junction discontinuity and vortex concentration at the dihedral corner (Finch, 1978), movably mounted winglets to control the angle of attack and bending moment (Daude, 1984), highly sweptback winglets with low aspect ratio to prevent flow break-away at high lift coefficients (Jupp & Rees, 1987), spiroid wingtips that loop until they fall back onto the wing (Gratzer, 1992), elliptical winglets to enforce continuous curvature (Felker, 2002), and multi-winglet variants to attempt to further break down the wingtip vortex (La Roche & Palffy, 1996; Smith *et al.*, 2001).

Winglet design garnered attention from sailplane designers such as Maughmer (2003, 2006), who used a multiple lifting-line method and a full panel method with relaxed-wake modeling in his works. He concluded that winglet design is a trade-off study because a reduction in induced drag is achieved for a larger wetted area, which is in turn accompanied by an increase in profile drag.

The performance of a particular winglet is contingent on its design and the flight conditions. As such, optimized designs vary greatly between applications and few generalities exist. Whitcomb (1976) suggested that a toe-out angle is needed for good winglet performance, and obtained up to 9 % improvement in lift-to-drag ratio and 20 % reduction in induced drag at *Re* of 5.25×10^6, while a wingtip extension provided only 4 % improvement on the lift-to-drag ratio for the same change in root bending moment. Smith *et al.* (2001) tested multi-winglets at *Re* from 161,000 to 300,000 and achieved up to 15-30 % improvement in lift-to-drag ratio

relative to their baseline NACA 0012 wing, observing that dihedral spread helped distribute the vortex. Takenaka *et al.* (2008) performed an optimization in which they minimized the block fuel and maximum takeoff weight to indirectly optimize a winglet in transonic flow using an Euler code. They observed that an abrupt transition encouraged wave drag at the wing-winglet junction, and noted that span length and cant angle held the most influence in their study. A blended winglet was obtained as optimization result, with the winglet leading edge positioned aft of the wing leading edge – corroborating the observation made by Conley (1980) on the design of the Learjet that a toe-out angle is important. Marchman *et al.* (1978) established that symmetric winglets are the best suited for general aviation, but have reduced effectiveness on tapered wings. Eppler (1997) showed that positive dihedral yields superior improvements relative to negative dihedral by using a new theory for aerodynamic calculations rather than classical theories with rigid wake models, which yield identical results for both cases.

1.4.3   Performance parameters

It is necessary to establish measures of merit to assess how desirable the aerodynamics of each test wing is so that the best wing is obtained at the end of the design process. Aircraft can be optimized for various parameters, such as range, endurance, and fuel consumption. Range and endurance appear to be particularly well-suited parameters to optimize for a surveillance UAV, whose task is to remain in the air for as long as possible while covering the most ground. The mathematical implementation for maximized range and endurance for propeller aircraft is reviewed in the next two subsections.

1.4.3.1   Range

Equations can be written to relate the specific fuel consumption (*SFC*), propeller efficiency η and power for a propeller-driven aircraft. For steady, level flight, where an equilibrium of forces exists such that lift equals weight and drag equals thrust, those equations can be simplified to obtain the Breguet range equation (Roskam & Lan, 1997),

$$R = \frac{\eta}{SFC} \frac{C_L}{C_D} \ln \frac{W_0}{W_1} \tag{1.2}$$

in which it is assumed that the lift-to-drag ratio (C_L/C_D) can be considered constant, W_0 is the weight with full fuel tanks, and W_1 is the weight with empty fuel tanks. A distinct and direct relationship is observed between the range and the lift-to-drag ratio, making the latter a suitable measure of merit when maximized.

1.4.3.2 Endurance

Similarly, the Breguet endurance formula can be obtained (Roskam & Lan, 1997),

$$E = \frac{\eta}{SFC} \frac{C_L^{3/2}}{C_D} (2\rho_\infty S)^{1/2} (W_1^{-1/2} - W_0^{-1/2}) \tag{1.3}$$

in which ρ_∞ is the freestream fluid density, and S is the planar area of the wings. Maximum endurance is obtained for a propeller-driven aircraft when the power required is minimum, such that the rate of fuel consumption is also minimum. From Equation (1.3), it becomes evident that the driving factor linked to aerodynamic wing design is $C_L^{3/2}/C_D$.

1.4.4 Morphing Wings

The concept of morphing refers to the active changing of the vehicle shape in flight. However, control surfaces are generally not considered as morphing processes because they are aimed at controlling the attitude of an aircraft and not at improving the aerodynamic or structural design of the flight vehicle. UAVs have proved to be more amenable to morphing aircraft research, as is the case for this work. Barbarino *et al.* (2011) provide a detailed and comprehensive review of morphing aircraft, to which the reader is referred for a synthesis of research conducted on aircraft with morphing capabilities up to that point, prior to which Rodriguez (2007) published a survey of morphing aircraft technology. Weisshaar (2013) provides a historical perspective

on morphing aircraft systems, and emphasizes with evidence from past studies that morphing aircraft are not necessarily overly expensive, heavy, or reliant on special materials or elaborate mechanisms.

More recently, Mestrinho *et al.* (2011) presented the design optimization of a small UAV with a variable-span morphing wing operating at speeds of 11–40 m/s. Their results showed that near the maximum speed, a drag reduction of up to 20 % could be obtained for the morphing wing relative to the non-morphing wing. Falcão *et al.* (2011) analyzed a servo-actuated articulated winglet capable of rotating about the vertical and aircraft longitudinal axes to actively manipulate the toe and cant angles of the winglet, respectively. The motivation behind this morphing approach is that winglet efficacy depends heavily on wing loading which varies during the different phases of flight. The proposed concept was applied to a UAV, and a notable reduction in stall speed was reported accompanied by a takeoff ground roll reduction of 20 %, leading to a shorter takeoff distance. Smith *et al.* (2014) conducted computational and experimental analyses for a commercial aircraft wing with two outboard sections of the wings capable of twist and dihedral variations. Their aerostructural investigations clearly indicated that a trade-off is necessary: larger dihedral angles cause a loss of lift and potentially increase drag, but reduce bending stress. For the outer-wing twist, they observed that the lift-to-drag ratio could be improved to some extent at the expense of an increased root bending moment.

Yokozeki *et al.* (2014) proposed a seamless deformable aileron made using corrugated structures in the trailing edge region. They demonstrated the feasibility of the design using nonlinear finite element analysis. Wind tunnel testing of a model was performed at Reynolds numbers of 5×10^5 to 1.5×10^6, and results showed that a greater increase in lift is obtained relative to the traditional hinged-aileron counterpart when the aileron incidence is increased. Zhang *et al.* (2014) designed a distributedly actuated morphing wing to continuously vary the camber. They investigated the axial driving force and deformations that could be obtained from telescopic tube actuators analytically and experimentally. The large axial driving force and high power density of the actuators proved to be a successful means of implementing variable camber in a morphing wing. Lyu & Martins (2015) studied morphing trailing-edge wings to reduce

fuel consumption of transport aircraft. They obtained a 1 % reduction in drag at on-design conditions and a 5 % reduction in drag closer to off-design conditions.

A wide scope of studies has been done at the LARCASE on the topic of morphing wings, including controller design and optimization for a wing with a shape memory alloys (Grigorie *et al.*, 2012a,b). In closer relation to the work presented in this thesis, aerodynamic studies to delay the onset of transition by changing the airfoil shape using actuators were performed. The morphing concept entailed the deformation of a flexible portion of the upper surface of the wing. An ATR-42 reference wing was studied in the series of morphing studies conducted at the LARCASE, in which an airfoil optimization study predicted a drag reduction of up to 26.73 % and a transition point delay of up to 24.81 %. The optimization was carried out using a genetic algorithm using results from the 2D flow solver XFOIL (Drela, 1989). Experimental results later showed that improvements on the ATR-42 airfoil were greater in practice than predicted numerically (Koreanschi *et al.*, 2015).

The airfoil on the Hydra S4 Ehécatl UAV wing was subsequently studied using the same approach, yielding drag reductions of up to 21.7 % and transition delay of 18.7 % of the chord at Mach 0.2 for a constrained lift value (Sugar Gabor *et al.*, 2013b). The genetic algorithm for optimization was supplemented with a Broyden-Fletcher-Goldfarb-Shanno gradient-descent algorithm and used in conjunction with a lifting-line solver tailored to this morphing design to calculate 2.5D flow solutions (Sugar Gabor *et al.*, 2013a,c). Lift-to-drag ratio maximization yielded up to 4 % improvement relative to the baseline wing (Sugar Gabor *et al.*, 2015). A vortex lattice solver was also developed for the analysis of this type of morphing wing (Sugar Gabor *et al.*, 2016). Two optimization procedures were completed. The baseline wing was redesigned in the first optimization, and an increase in wing span from 4.2 m to 5 m reduced the total drag coefficient by up to 10 % by reducing the induced drag despite the observed profile drag increase. The second optimization stage consisted of a morphing optimization of the redesigned wing to counter the profile drag increase incurred in the first optimization stage. The morphing aptitudes allowed a further reduction in drag coefficient between 1 % and 4.5 %.

A morphing aileron for commercial aircraft was studied, targeting boundary layer behaviour with the objective of delaying flow separation. For two aileron deflection angles, it was found that the lift coefficient of the airfoil increased by up to 17 % for the upward deflection and by up to 19 % for the downward deflection (Koreanschi *et al.*, 2014). These results were validated using experimental boundary layer measurements obtained using infrared thermography (Koreanschi *et al.*, 2016a). Successful transition delay was observed experimentally by over 10 % to no detriment to the lift coefficient (Koreanschi *et al.*, 2016b).

For the implementation of designs involving flexible, deformable or composite skins, the reader is referred to Thill *et al.* (2008), who discuss morphing skins for engineering applications in detail.

CHAPTER 2

COMPUTATIONAL TOOLS

This chapter addresses the underlying theory of the computational tools used in the present work for simulation and optimization.

2.1 Outline

An outline of the research methodology is shown through flowcharts in Figure 2.1. The left-most flowchart shows the process from start to finish for a CFD-based optimization process, which includes three subprocesses which are then expanded separately as new flowcharts on the right. This chapter is dedicated to explaining the steps shown in the flowcharts.

2.2 Reynolds-Averaged Navier-Stokes Solver

High-fidelity results for flow fields can be obtained through computational fluid dynamics solvers. To conduct CFD simulations, the commercial software package ANSYS Fluent (V6) was used. The next subsections present the principles which are of relevance to this study.

2.2.1 Governing equations

The Navier-Stokes equations, which are a set of momentum conservation equations, are the foundation of modern-day CFD solvers. They are a formulation of Newton's second law of motion ("$F = ma$") applied to a volume of fluid which, by themselves, do not constitute a system of equations that can fully describe a flow field; the continuity equation for the conservation of mass is also necessary at the very least, so that velocity components and pressure can be calculated.

Depending on the type of flow at hand, other equations may also be needed for an accurate representation of the physics of the problem. In the case of compressible flows, for example,

24
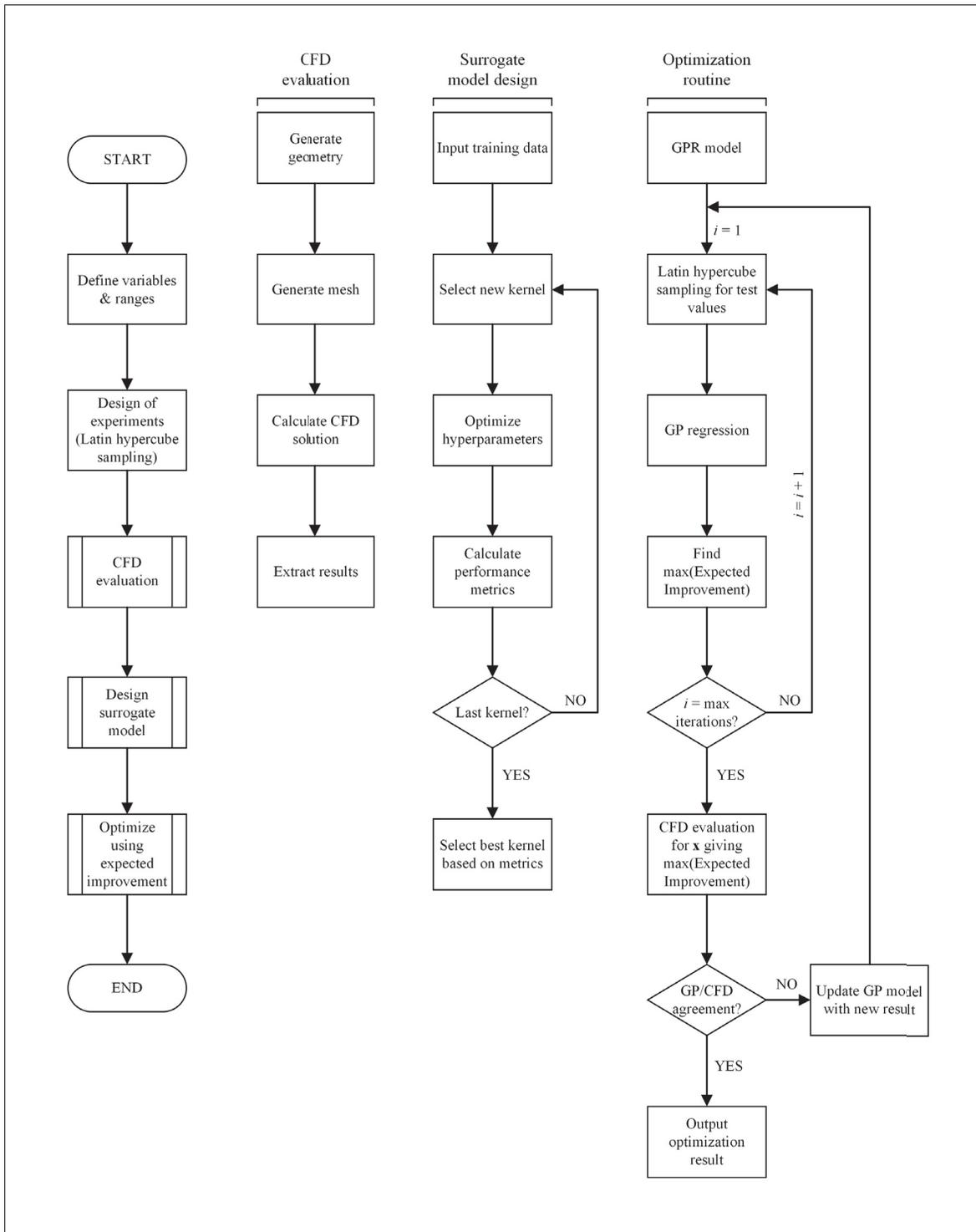
Figure 2.1   Outline of the research methodology

conservation of energy needs to be applied through the First Law of Thermodynamics to establish the density field. Additional variables, temperature and viscosity, are then also updated through the ideal gas law and Sutherland's Law, respectively. Other examples of flows that require supplementary equations are reacting flows and multiphase flows.

2.2.1.1   Conservation of mass

The Navier-Stokes and continuity equations govern all Newtonian fluid flows provided that the medium under consideration is a continuum. The law of conservation of mass applied to a volume of fluid in an inertial reference frame dictates that inflow less the outflow through the volume, represented by S_m, must equal the rate of accumulation or loss of mass in this volume. From this notion, the conservation form of the continuity equation can be derived by considering mass flow through all faces of the fluid volume in a chosen coordinate system. Mathematically,

$$\frac{\partial \rho}{\partial t} + \nabla \cdot (\rho \mathbf{u}) = S_m \tag{2.1}$$

in which ρ is the local fluid density, and $\mathbf{u}$ is the fluid velocity vector. The first term on the left-hand side is the local derivative of the density, while the second term is the divergence of the mass flow rate. Physically, the divergence of a vector field represents the rate of change of the vector quantity through a scalar field. For an infinitesimally small control volume of fixed mass, the divergence term can be interpreted as the rate of change of the volume of fluid. In the case of an incompressible fluid, mass density is constant; consequently, the volume of each fluid element is also constant, leading to a divergence-free flow and the simplification of the continuity equation to $\nabla \cdot \mathbf{u} = S_m$.

2.2.1.2   Conservation of momentum

The same approach can be used to consider the conservation of momentum. Newton's second law of motion is used in the sense that force is treated as the time rate of change of momentum. Mathematically, the law of conservation of momentum (Batchelor, 1970) is given by

$$\frac{\partial}{\partial t}(\rho \mathbf{u}) + \nabla \cdot (\rho \mathbf{uu}) = -\nabla p + \nabla \cdot \left(\bar{\bar{\tau}}\right) + \rho \mathbf{g} + \mathbf{F} \tag{2.2}$$

The first term on the left-hand side of equation (2.2) is the local derivative of the mass flux (mass flow rate per unit area), while the second term is the convective derivative which factors in changes in the fluid element by virtue of its motion. The first term on the right-hand side is the volumetric stress tensor responsible for the hydrostatic force. The second term is the divergence of the deviatoric stress tensor $\bar{\bar{\tau}}$, which takes viscosity into account to generate a viscous force. The third and fourth terms are gravitational and body forces, respectively.

The stresses in the deviatoric stress tensor are generally considered as functions of dynamic viscosity and the velocity gradients for a Newtonian fluid (ANSYS Inc., 2016):

$$\bar{\bar{\tau}} = \mu \left[\left(\nabla \mathbf{u} + \nabla \mathbf{u}^T \right) - \frac{2}{3} (\nabla \cdot \mathbf{u}) \bar{\bar{I}} \right] \tag{2.3}$$

The second term in the square brackets is obtained through Stoke's hypothesis. The main diagonal terms in the deviatoric stress tensor are the normal stresses while the other terms are the shear stresses acting on the fluid element.

For an incompressible three-dimensional fluid flow, a system of four equations is obtained using equations (2.1) and (2.2) to solve for four unknowns, namely pressure and three velocity components.

The velocity-velocity dyad $\mathbf{uu}$ in equation (2.2) causes the Navier-Stokes equations to be non-linear partial differential equations, making analytical solutions possible only for simplified

cases. For turbulent flows, the only known feasible approach to solving the Navier-Stokes equations is numerically. The equations can be solved by dividing a fluid domain into a collection of small control volumes and solving them for each control volume. Equations (2.1) and (2.2) are in conservation form, which is the most suitable form since they are already expressed for a control volume. A finite volume method is used in most CFD codes, including FLUENT, because of its applicability to a wide range of problems and suitability when complex geometries are at hand. Additionally, conservation equations are solved exactly for the control volumes that constitute the fluid domain. (Versteeg & Malalasekera, 2007)

2.2.2   Reynolds averaging

Resolution of all scales of turbulence is generally prohibitive in terms of computational requirements except for very low Reynolds numbers. A convenient alternative to using the conservation equations directly is to use Reynolds decomposition to obtain the Reynolds-averaged Navier-Stokes equations. In Reynolds decomposition, instantaneous quantities are decomposed into a mean and a fluctuating component (Wallin, 2000):

$$u_i = \overline{u_i} + u_i'$$
(2.4)

where the Einstein summation convention is used with tensor notation, and the bar symbol indicates the statistically-averaged value. The Reynolds-averaged continuity and momentum equations (2.1) and (2.2) thus become,

$$\frac{\partial \rho}{\partial t} + \frac{\partial}{\partial x_i}(\rho u_i) = 0$$
(2.5)

$$\frac{\partial}{\partial t}(\rho u_i) + \frac{\partial}{\partial x_j}(\rho u_i u_j) = \frac{\partial p}{\partial x_i} + \frac{\partial}{\partial x_j}\left[\mu\left(\frac{\partial u_i}{\partial x_j} + \frac{\partial u_j}{\partial x_i} - \frac{2}{3}\delta_{ij}\frac{\partial u_i}{\partial x_i}\right) + \frac{\partial}{\partial x_j}\left(-\rho\overline{u_i'u_j'}\right)\right]$$
(2.6)

2.2.3 Boussinesq hypothesis

The Reynolds stresses appear as $-\rho\overline{u_i'u_j'}$ in equation (2.6). The Boussinesq hypothesis (Hinze, 1975) is used to calculate those terms to close the RANS equations in several turbulence models. The Reynolds stresses are calculated as functions of the velocity gradients and the turbulent (or eddy) viscosity μ_t:

$$-\rho\overline{u_i'u_j'} = \mu_t\left(\frac{\partial u_i}{\partial x_j} + \frac{\partial u_j}{\partial x_i}\right) - \frac{2}{3}\left(\rho k + \mu_t\frac{\partial u_k}{\partial x_k}\right)\delta_{ij} \tag{2.7}$$

wherein the turbulent kinetic energy term k appears from the contraction of a $u_i u_i$ product. This contraction introduces a Kronecker delta term, where $\delta_{ij} = 0$

2.2.4 Turbulence modeling

Several linear eddy viscosity models have been proposed based on the Boussinesq assumption to close the RANS equations. Turbulence models can be categorized based on the number of equations they use to model turbulent phenomena. Popular models include the one-equation Spalart-Allmaras model (Spalart & Allmaras, 1992), the two-equation k-ε (Launder & Spalding, 1972), k-ω (Wilcox, 1998) and shear stress transport (SST) (Menter *et al.*, 1994) models, and the four-equation transitional SST model (Menter *et al.*, 2006).

The possibility of modeling laminar-to-turbulent transition of the boundary layer of the wing is of interest in this thesis because of the flow regime encountered by the S45 Bàalam wing, as is later discussed in § 3.3. One anticipated contributing element to improving aerodynamic performance of a test wing using active morphing is the delay of transition to turbulence; as such, the k-ω SST turbulence model has been selected for its coupling capabilities in ANSYS Fluent with the γ-Re_θ transition model.

The transport equations for the k-ω SST turbulence model are the following (Menter *et al.*, 1994):

$$\frac{\partial}{\partial t}(\rho k) + \frac{\partial}{\partial x_i}(\rho k u_i) = \frac{\partial}{\partial x_j}\left(\left(\mu + \frac{\mu_t}{\sigma_k}\right)\frac{\partial k}{\partial x_j}\right) + G_k + Y_k + S_k \tag{2.8}$$

$$\frac{\partial}{\partial t}(\rho \omega) + \frac{\partial}{\partial x_i}(\rho \omega u_i) = \frac{\partial}{\partial x_j}\left(\left(\mu + \frac{\mu_t}{\sigma_\omega}\right)\frac{\partial \omega}{\partial x_j}\right) + G_\omega + Y_\omega + S_\omega + D_\omega \tag{2.9}$$

In Equations (2.8) and (2.9), the G terms are production terms. G_k represents the production of turbulence kinetic energy k caused by mean velocity gradients, and G_ω represents the generation of the specific turbulent dissipation rate ω, where ω is a measure of the time rate at which k dissipates into thermal internal energy per unit volume. Similarly, Y_k and Y_ω are dissipation terms representing the dissipation of k and ω owing to turbulence, respectively, and S_k and S_ω are user-defined source terms. D_ω is the cross-diffusion term, expressed as follows:

$$D_\omega = 2(1 - F_1)\frac{\rho \sigma_{\omega 2}}{\omega}\frac{\partial k}{\partial x_j}\frac{\partial \omega}{\partial x_j} \tag{2.10}$$

in which the blending function F_1 appears. F_1 serves to activate the k-ω model in the near-wall region and the k-ε model in the surrounding region, achieving a continuous blend between the two models throughout the flow field thereby allowing each model to be active where they perform best.

2.2.5 Transition modeling

Menter's two-equation k-ω SST model can be extended and coupled to include transition modeling to yield a model known as the Langtry-Menter four-equation Transitional SST model (Menter *et al.*, 2006). This model is also called the γ-Re_θ model in reference to the variables used in modeling transition, γ being the intermittency which defines the percentage of time that the boundary layer is turbulent, and $\widetilde{Re_{\theta_t}}$ being the transition Reynolds number based on boundary layer momentum thickness. Past $\widetilde{Re_{\theta_t}}$ in the boundary layer, intermittency begins to increase, marking the onset of laminar-to-turbulent transition.

The transport equations for the γ-Re_θ transition model are as follows:

$$\frac{\partial(\rho\gamma)}{\partial t} + \frac{\partial(\rho u_j \gamma)}{\partial x_j} = P_\gamma - E_\gamma + \frac{\partial}{\partial x_j}\left[\left(\mu + \frac{\mu_t}{\sigma_\gamma}\right)\frac{\partial\gamma}{\partial x_j}\right] \qquad (2.11)$$

$$\frac{\partial\left(\rho\widetilde{Re}_{\theta_t}\right)}{\partial t} + \frac{\partial\left(\rho u_j \widetilde{Re}_{\theta_t}\right)}{\partial x_j} = P_{\theta t} + \frac{\partial}{\partial x_j}\left[\sigma_{\theta t}\left(\mu + \mu_t\right)\frac{\partial\widetilde{Re}_{\theta_t}}{\partial x_j}\right] \qquad (2.12)$$

P_γ and E_γ are source terms in the γ-equation, and $P_{\theta t}$ is the source term in the $\widetilde{Re}_{\theta_t}$-equation.

An important requirement intrinsic to each turbulence model is the y^+ requirement, which determines the minimum height of the first cells from the walls for an accurate solution to be obtained. For the k-ω SST model, the recommended value is, with little impact, anywhere between 0.001 and 1, (ANSYS Inc., 2016).

2.2.6   Computational grid

To solve the Navier-Stokes equations using the finite volume method, a grid is constructed to spatially discretize the fluid domain. A multi-block 3D structured grid is generated in ICEM CFD such that element faces are either aligned or normal to the flow direction to minimize the spatial discretization error and error due to numerical diffusion. A high-quality mesh produces more accurate solutions and improves the convergence rate compared to a poorer quality mesh.

Figure 2.2 shows the grid used to perform the CFD simulations in ANSYS Fluent. The dimensions of the fluid domain are selected far enough from the wing to ensure that the fluid has returned to freestream conditions at the edges of the grid despite the perturbation in the flow field caused by the presence of the wing. Far-field planes are modeled 7 metres ahead and 14 metres behind the origin defined at the leading edge of the wing root. These far-field planes are 14 metres high and 7 metres wide, such that flow at the boundaries can be considered unperturbed by the presence of the wing. The outlet of the fluid domain is placed further than the other boundaries to allow the vortex developing at the wing tip to travel downstream.

An H-grid topology is used in creating the rectangular domain. To finely resolve the boundary layer gradients, an O-grid is used around the wing to create a radially-oriented curvilinear distribution of element edges which become progressively smaller (Figure 2.3) as they approach the wing surface. The mesh is also denser at the wing-tip to properly capture the effects of vortices that develop at the wing tip on account of flow leakage.

The rate of change of element sizes is carefully controlled to prevent sudden jumps which can cause a reduction in the order of accuracy of the solution. To prevent backflow and mass imbalance issues at the domain edges behind the wing, which were observed to occur during the development of the meshing procedure, larger cells with higher aspect ratio are used near the domain edges close to the outlet.
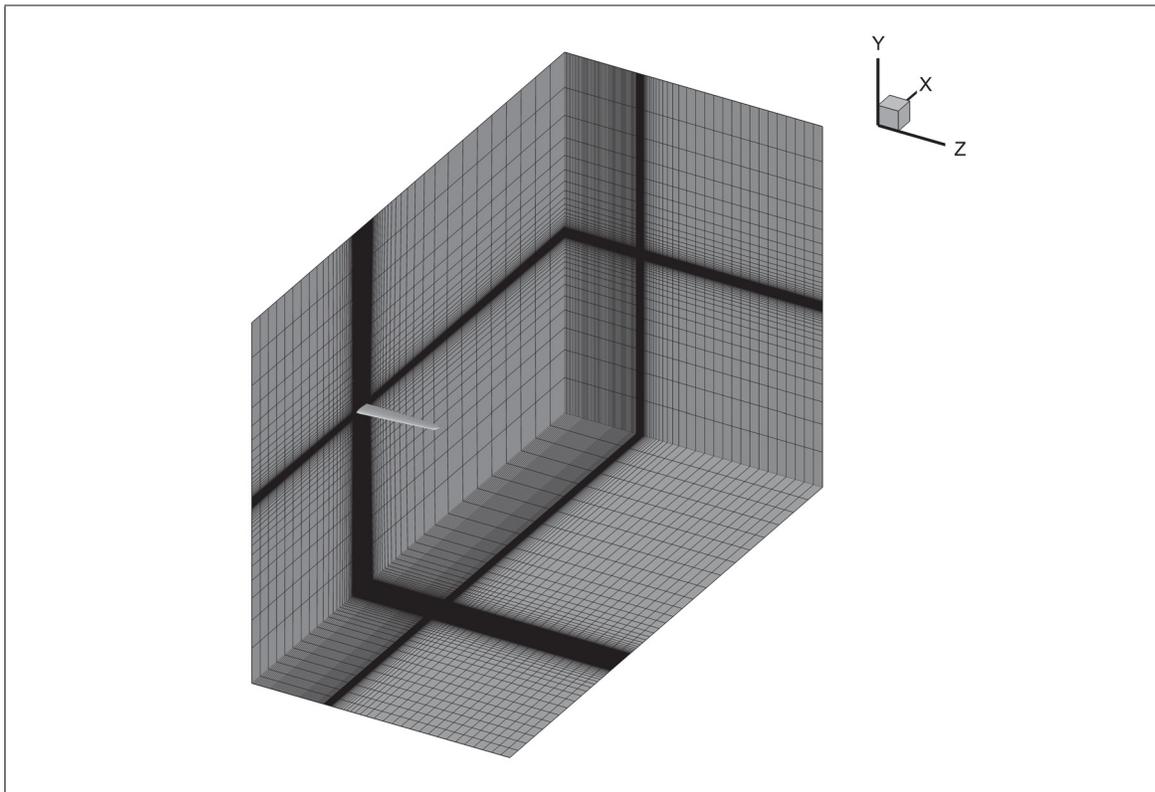
Figure 2.2   Finite volume mesh for CFD simulations
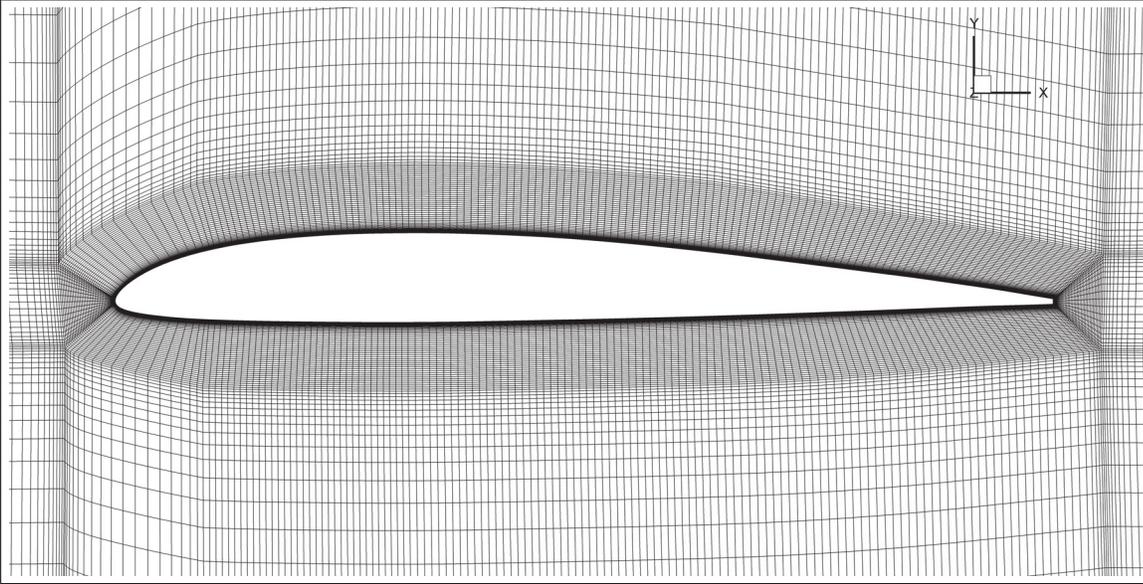
Figure 2.3　Boundary layer mesh for CFD simulations

A grid sensitivity study was conducted to determine the mesh density required to produce final results of acceptable fidelity. Five grids of varying resolution were tested at two angles of attack, $0°$ and $12°$ at a Reynolds number of 1.0×10^6, which is the flight condition used in Chapters 3 and 4, and close to the upper Re limit of 1.07×10^6 in terms of flight envelope. A $y^+ < 1$ was maintained regardless of the grid under test for the turbulence and transition models to work properly, as mentioned in the previous sub-section. The variations with mesh density of C_L, C_D, C_L/C_D, and laminar-to-turbulent transition location X/c at two spanwise locations Z/b of 0.3 and 0.7 are shown in Tables 2.1 and 2.2. These results are also plotted in Figures 2.4–2.7. In each series of simulations at $0°$ and $12°$, it is observed that the most dense mesh marginally affects the results, which vary asymptotically as the the number of cells is increased. The values obtained using the fourth grid relative to those obtained using the fifth and most dense grid are shown in Table 2.3 as percentages. The differences in the compared values for the two finest grids are below 2 % for all the values tested, such that the fourth mesh density is deemed to produce sufficiently accurate results.

Based on the grid sensitivity study discussed, the number of cells used for each series of simulations conducted in this thesis is shown in Table 2.4.

Table 2.1   Grid sensitivity results at $\alpha = 0°$ and $Re = 1.0 \times 10^6$

Number of cells	C_L	C_D	C_L/C_D	X/c at $Z/b = 0.3$	X/c at $Z/b = 0.7$
1,000,442	0.2377	0.007605	31.26	0.4165	0.1500
1,475,928	0.2273	0.007224	31.46	0.6395	0.5981
2,274,424	0.2218	0.006996	31.71	0.6911	0.7015
3,853,252	0.2170	0.006792	31.94	0.7285	0.7200
6,578,640	0.2155	0.006734	32.01	0.7313	0.7215

Table 2.2   Grid sensitivity results at $\alpha = 12°$ and $Re = 1.0 \times 10^6$

Number of cells	C_L	C_D	C_L/C_D	X/c at $Z/b = 0.3$	X/c at $Z/b = 0.7$
1,000,442	1.403	0.07423	18.90	0.0643	0.0615
1,475,928	1.342	0.07054	19.02	0.0805	0.0975
2,274,424	1.297	0.06759	19.19	0.1176	0.1156
3,853,252	1.266	0.06546	19.34	0.1275	0.1367
6,578,640	1.253	0.06466	19.38	0.1280	0.1366

Table 2.3   Grid sensitivity as percentages at $\alpha = 0°$ and $12°$ at $Re = 1.0 \times 10^6$

α	C_L	C_D	C_L/C_D	X/c at $Z/b = 0.3$	X/c at $Z/b = 0.7$
0°	-0.67	-0.87	0.19	0.38	0.21
12°	-1.05	-1.25	0.19	0.39	-0.02

Table 2.4   Mesh sizes for CFD simulations

Simulation series	Number of cells
S45 original wing, w/o winglet	3,873,252
S45 original wing, with winglet	4,883,040
S45 wing optimization, w/o winglet	3,873,252
S45 morphing wing optimization, w/o winglet	3,971,016
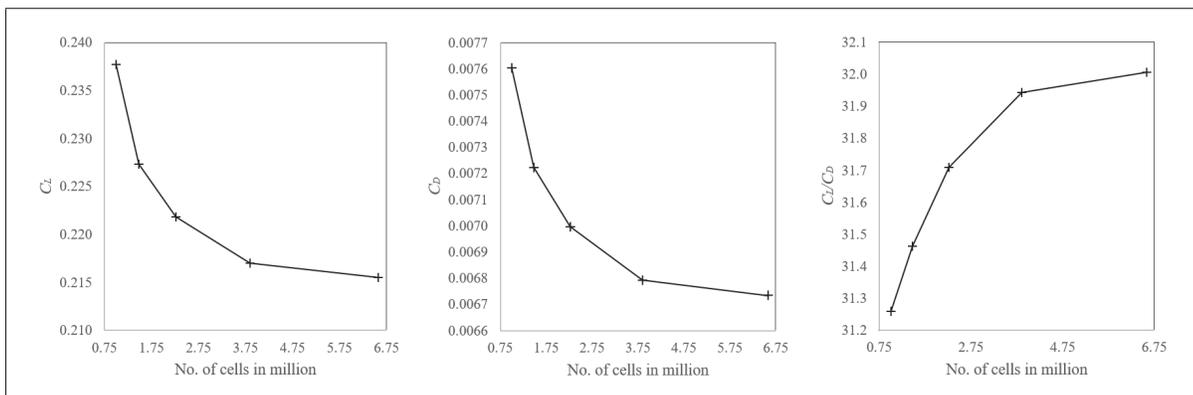
Figure 2.4   Grid sensitivity plots at $\alpha = 0°$ and $Re = 1.0 \times 10^6$
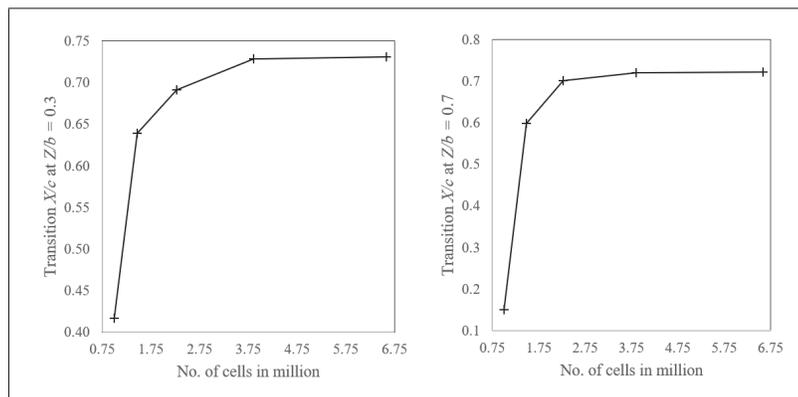
Figure 2.5   Grid sensitivity plots for transition point at $\alpha = 0°$ and $Re = 1.0 \times 10^6$
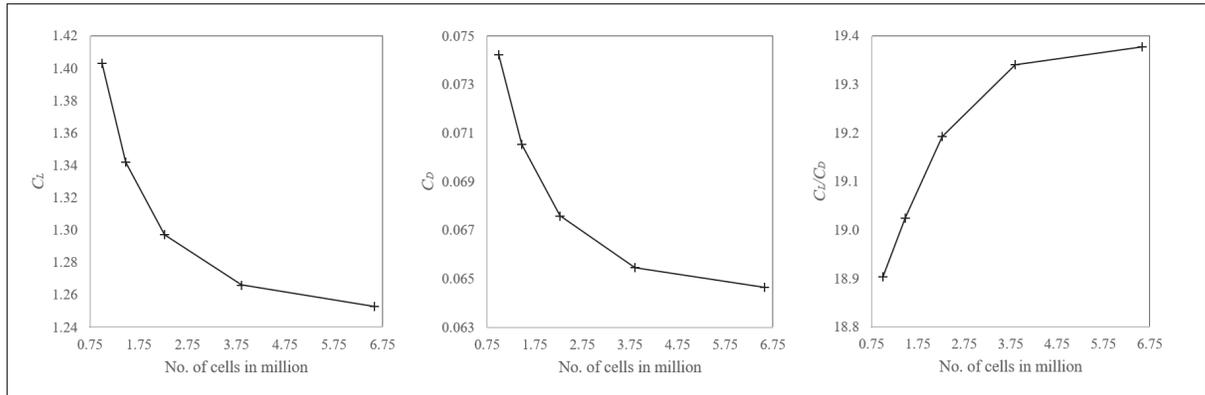
Figure 2.6   Grid sensitivity plots at $\alpha = 12°$ and $Re = 1.0 \times 10^6$
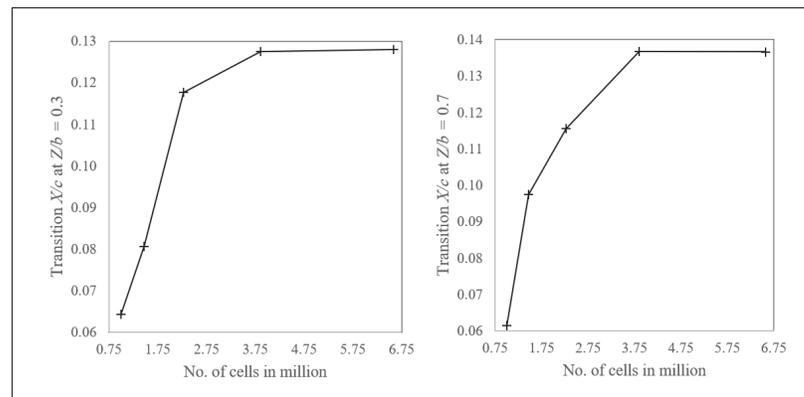
Figure 2.7   Grid sensitivity plots for transition point at
$\alpha = 12°$ and $Re = 1.0 \times 10^6$

2.2.7   Boundary conditions

Boundary conditions (BCs) are required to solve the difference equations for each fluid volume. Figure 2.8 shows some of the BCs enforced. A symmetry BC is placed at the right- and left-wing junction, imposing that all property values be the same at -Z as those at Z, effectively allowing the simulation to be calculated for only one wing. A velocity inlet allows mass flow into the domain at the test velocity, while a pressure outlet allows mass flow out of the domain. Slip walls are imposed on the sides of the far-field to improve convergence, which was observed to be difficult with the transition SST model, particularly with pressure outlets specified for the sides of the far-field. Finally, a no-slip wall BC is enforced at the surface of the wing such that

the fluid velocity at the surface is zero. A turbulence intensity of 1 %, turbulent viscosity ratio of 10, and an intermittency value of 1 are used at the inlet as turbulence BCs.
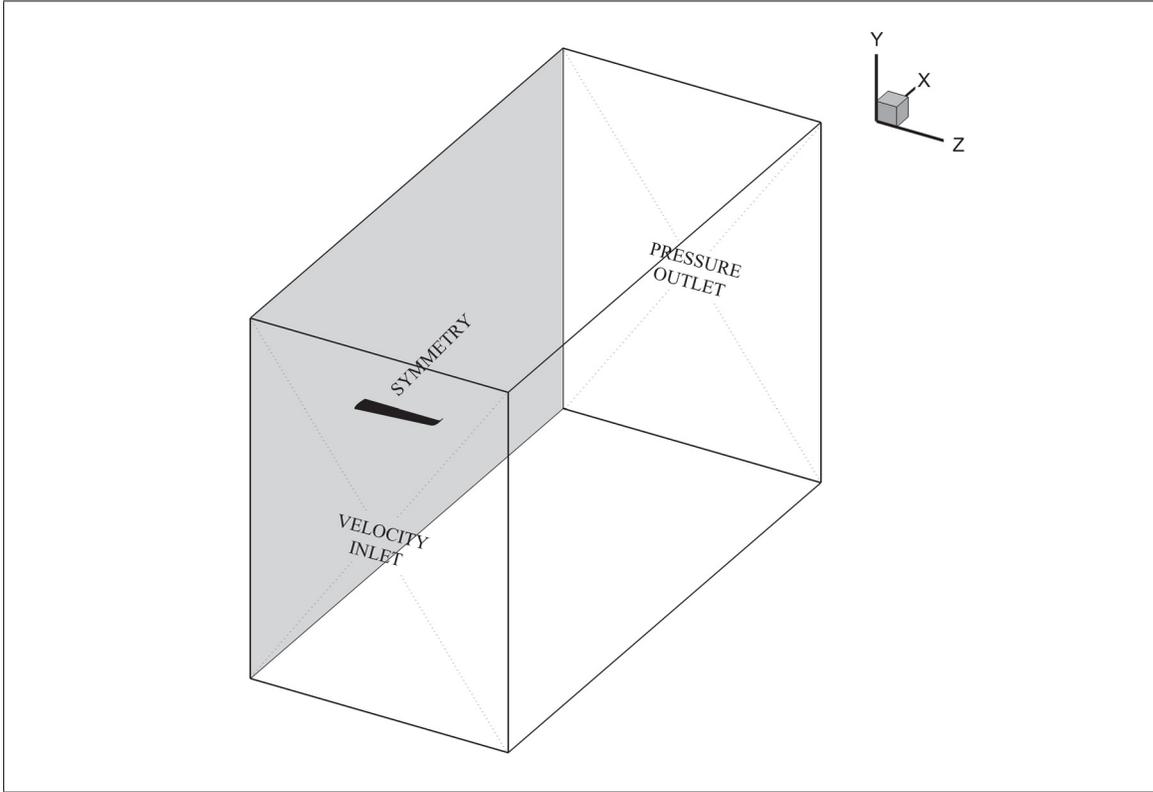
Figure 2.8   Boundary conditions for CFD simulations

2.3   Gaussian Processes

In surrogate-based modeling, approximations for $f(\mathbf{x})$ are sought, where the design variables $\mathbf{x} \in D \in \mathbb{R}^k$ in a k-dimensional design space D. A regression model is constructed based on a training data set from which properties of f are learned,

$$D = \{(\mathbf{x}_i, f(\mathbf{x}_i)), \quad i = 1 : N\} \tag{2.13}$$

The training data set consists of outputs denoted by $\mathbf{f}$ corresponding to the series of inputs $\mathbf{X}$.

A Gaussian Process (GP) model is a probabilistic statistical model which treats the deterministic response $f(\mathbf{x})$ as a realization of a random variable (RV). It is a Gaussian distribution over functions in that the mean and variance are functions of $\mathbf{x}$.

2.3.1 Gaussian process regression models

GP models have the advantage of being capable of dealing with noisy data. The noise-free formulation is presented before introducing the formulation for noisy data. The noisy formulation is particularly interesting because it allows the GP model to better generalize the behaviour of f while preventing overfitting by forcing the response surface to go through the data points. Because evaluations of f are obtained using CFD, deviations can occur from the true response induced by differing residual levels from solution to solution. The simple noise term used, called a nugget, is known to improve the quality of GP models.

2.3.1.1 Noise-free formulation

If f is assumed to be a GP, then its prior can be denoted by

$$f(\mathbf{x}) \sim \mathcal{GP}\left(m(\mathbf{x}), k(\mathbf{x}, \mathbf{x}')\right) \tag{2.14}$$

where $m(\mathbf{x})$ is the mean function and $k(\mathbf{x}, \mathbf{x}')$ is the covariance function quantifying the similarity between $\mathbf{x}$ and $\mathbf{x}'$ (Rasmussen & Williams, 2004), given by

$$m(\mathbf{x}) = \mathbb{E}[f(\mathbf{x})] \tag{2.15}$$

$$k(\mathbf{x}, \mathbf{x}') = \mathbb{E}\left[\left(f(\mathbf{x}) - m(\mathbf{x})\right)\left(f(\mathbf{x}') - m(\mathbf{x}')\right)^T\right] \tag{2.16}$$

The multivariate Gaussian distribution of this GP is then

$$\mathbf{f} \sim \mathcal{N}(\boldsymbol{\mu}, \mathbf{K}) \tag{2.17}$$

where $\boldsymbol{\mu}$ is the mean function and $\mathbf{K}$ is the positive semidefinite covariance matrix,

$$\mathbf{K} = \begin{bmatrix} k(\mathbf{x}_1, \mathbf{x}_1) & k(\mathbf{x}_1, \mathbf{x}_2) & \dots & k(\mathbf{x}_1, \mathbf{x}_n) \\ k(\mathbf{x}_2, \mathbf{x}_1) & k(\mathbf{x}_2, \mathbf{x}_2) & \dots & k(\mathbf{x}_2, \mathbf{x}_n) \\ \vdots & \vdots & \ddots & \vdots \\ k(\mathbf{x}_n, \mathbf{x}_1) & k(\mathbf{x}_n, \mathbf{x}_2) & \dots & k(\mathbf{x}_n, \mathbf{x}_n) \end{bmatrix} \tag{2.18}$$

The regression problem seeks a value of f for a particular $\mathbf{x}$ at which $f(\mathbf{x})$ is unknown, denoted by $\mathbf{f}_*$ for several desired function outputs for inputs $\mathbf{x}_*$. If it is assumed that the test values are drawn from the same distribution as the training data, a joint Gaussian is obtained:

$$\begin{bmatrix} \mathbf{f} \\ \mathbf{f}_* \end{bmatrix} \sim \mathcal{N}\left(\begin{bmatrix} \boldsymbol{\mu} \\ \boldsymbol{\mu}_* \end{bmatrix}, \begin{bmatrix} \mathbf{K} & \mathbf{K}_* \\ \mathbf{K}_*^T & \mathbf{K}_{**} \end{bmatrix} \right) \tag{2.19}$$

where

$$\mathbf{K}_* = \begin{bmatrix} k(\mathbf{x}_*, \mathbf{x}_1) & k(\mathbf{x}_*, \mathbf{x}_2) & \dots & k(\mathbf{x}_*, \mathbf{x}_N) \end{bmatrix} \tag{2.20}$$

$$\mathbf{K}_{**} = k(\mathbf{x}_*, \mathbf{x}_*) \tag{2.21}$$

Using the standard rules for the conditioning of Gaussians (Schur complements and the matrix inversion lemma), the posterior predictive density is

$$p\left(\mathbf{f}_* \mid \mathbf{X}_*, \mathbf{X}, \mathbf{f}\right) = \mathcal{N}\left(\mathbf{f}_* \mid \boldsymbol{\mu}_*, \boldsymbol{\Sigma}_*\right) \tag{2.22}$$

from which the mean and variance for $\mathbf{x}_*$ inputs can be found,

$$\boldsymbol{\mu}_* = \mathbf{K}_*^T \mathbf{K}^{-1} \mathbf{f} \tag{2.23}$$

$$\boldsymbol{\Sigma}_* = \mathbf{K}_{**} - \mathbf{K}_* \mathbf{K}^{-1} \mathbf{K}_*^T \tag{2.24}$$

The expected value of $\mathbf{f}_*$ is $\boldsymbol{\mu}_*$, which has variance $\boldsymbol{\Sigma}_*$.

2.3.1.2 Noisy formulation

In a case where the data available is noisy, the underlying function with noise can be written as

$$y = f(\mathbf{x}) + \epsilon, \quad \epsilon \sim \mathcal{N}\left(0, \sigma_y^2\right) \tag{2.25}$$

where the noise is Gaussian with zero mean and variance σ_y^2. The resulting covariance between the noisy responses becomes

$$\mathrm{cov}\left[y_p, y_q\right] = k\left(\mathbf{x}_p, \mathbf{x}_q\right) + \sigma_y^2 \delta_{pq} \tag{2.26}$$

The Dirac delta function $\delta_{pq} = \mathbb{I}(p = q)$ means that the noise term only influences the diagonal terms of the covariance matrix. The covariance matrix, previously $\mathbf{K}$, becomes $\mathbf{K} + \sigma_y^2 \mathbf{I}_N$ with the introduction of noise and is denoted by $\mathbf{K}_y$. The joint density is then

$$\begin{bmatrix} \mathbf{y} \\ \mathbf{f}_* \end{bmatrix} \sim \mathcal{N}\left(\begin{bmatrix} \boldsymbol{\mu} \\ \boldsymbol{\mu}_* \end{bmatrix}, \begin{bmatrix} \mathbf{K}_y & \mathbf{K}_* \\ \mathbf{K}_*^T & \mathbf{K}_{**} \end{bmatrix}\right) \tag{2.27}$$

and the corresponding posterior predictive density is

$$p\left(\mathbf{f}_* \mid \mathbf{X}_*, \mathbf{X}, \mathbf{y}\right) = \mathcal{N}\left(\mathbf{f}_* \mid \boldsymbol{\mu}_*, \boldsymbol{\Sigma}_*\right) \tag{2.28}$$

from which the mean and variance for $\mathbf{x}_*$ inputs can be found,

$$\boldsymbol{\mu}_* = \mathbf{K}_*^T \mathbf{K}_y^{-1} \mathbf{f} \tag{2.29}$$

$$\boldsymbol{\Sigma}_* = \mathbf{K}_{**} - \mathbf{K}_* \mathbf{K}_y^{-1} \mathbf{K}_*^T \tag{2.30}$$

2.3.1.3 Implementation

It is preferable not to invert $\mathbf{K}_y$ directly for numerical stability reasons. Instead, a Cholesky decomposition is used,

$$\mathbf{K}_y = \mathbf{L}\mathbf{L}^T \tag{2.31}$$

such that

$$\mathbf{X} \sim \boldsymbol{\mu} + \mathbf{L}\mathcal{N}(\mathbf{0}, \mathbf{I}) \tag{2.32}$$

The intermediate variable $\boldsymbol{\alpha}$ is used,

$$\boldsymbol{\alpha} = \mathbf{K}_y^{-1}\mathbf{y} = \mathbf{L}^{-T}\mathbf{L}^{-1}\mathbf{y} \tag{2.33}$$

The mean and variance of a predicted value are then calculated as

$$\mathbb{E}[f_*] = \mathbf{k}_*^T\boldsymbol{\alpha} \tag{2.34}$$

$$\mathrm{var}[f_*] = k_{**} - \mathbf{k}_*^T\mathbf{L}^{-T}\mathbf{L}^{-1}\mathbf{k}_* \tag{2.35}$$

where $\mathbf{k}_* = \begin{bmatrix} k(\mathbf{x}_*, \mathbf{x}_1), \ldots, k(\mathbf{x}_*, \mathbf{x}_N) \end{bmatrix}$ and $\mathbf{k}_{**} = k(\mathbf{x}_*, \mathbf{x}_*)$

2.3.2 Covariance functions

In the previous section, several references were made to the covariance terms or covariance function. Also called the kernel, the covariance function of a GP is the crux of the model and determines the predictive performance achievable.

For a problem whose underlying driving parameters are unknown, automatic relevance detection (ARD) kernels are expedient to identify the more influential variables by learning individual length scale hyperparameters λ_d for each of the d input variables. The value for λ_d is representative of the relevance of input variable d: a large length scale suggests that d has a low impact because its reciprocal is small. Since covariance is a measure of similarity between two points, a term that frequently appears in covariance functions is the Euclidean distance between those two points.

2.3.2.1 ARD squared exponential kernel

The ARD squared exponential kernel (SE) is the multi-length scale formulation for one of the most commonly used kernels, the squared exponential kernel, also known as the radial basis function (RBF) kernel. Its Euclidean distance in the form of $(\mathbf{x}_i - \mathbf{x}_j)^2$, and σ_f is a scale

factor and σ_m is the length scale for the mth design parameter. This kernel is very smooth, and infinitely differentiable (Snoek *et al.*, 2012). Mathematically,

$$k\left(\mathbf{x}_i,\mathbf{x}_j \mid \boldsymbol{\theta}\right) = \sigma_f^2 \exp\left[-\frac{1}{2}\sum_{m=1}^{d}\frac{\left(\mathbf{x}_{im} - \mathbf{x}_{jm}\right)^2}{\sigma_m^2}\right] \tag{2.36}$$

2.3.2.2 ARD Matérn kernel

The Matérn kernel has the general form

$$k(r) = \frac{2^{1-\nu}}{\Gamma(\nu)}\left(\sqrt{2\nu}r\right)^{\nu}K_{\nu}\left(\sqrt{2\nu}r\right) \tag{2.37}$$

where the Euclidean distance r is given by $\frac{\|\mathbf{x}-\mathbf{x}'\|}{l}$, $\nu > 0$, length scale $l > 0$, and modified Bessel function K_{ν}. The kernel has several variants, depending which order of ν is used, with the degrees of freedom, ν, defining the roughness of the random functions in that they are $(\nu - 1)$ times differentiable.

The ARD Matérn 3/2 kernel is once differentiable, and can be written as

$$k\left(\mathbf{x}_i,\mathbf{x}_j \mid \boldsymbol{\theta}\right) = \sigma_f^2\left(1 + \sqrt{3}r\right)\exp\left(-\sqrt{3}r\right) \tag{2.38}$$

while the ARD Matérn 5/2 kernel is twice differentiable (Snoek *et al.*, 2012), and can be written as

$$k\left(\mathbf{x}_i,\mathbf{x}_j \mid \boldsymbol{\theta}\right) = \sigma_f^2\left(1 + \sqrt{5}r + \frac{5}{3}r^2\right)\exp\left(-\sqrt{5}r\right) \tag{2.39}$$

where the Euclidean distance r between $\mathbf{x}_i$ and $\mathbf{x}_j$ is given by

$$r = \sqrt{\sum_{m=1}^{d} \frac{\left(\mathbf{x}_{im} - \mathbf{x}_{jm}\right)^2}{\sigma_m^2}} \tag{2.40}$$

2.3.2.3 ARD rational quadratic kernel

The ARD rational quadratic (RQ) kernel function is defined by the following expression (Murphy, 2012):

$$k\left(\mathbf{x}_i, \mathbf{x}_j \mid \boldsymbol{\theta}\right) = \sigma_f^2 \left(1 + \frac{1}{2\alpha_{RQ}} \sum_{m=1}^{d} \frac{\left(\mathbf{x}_{im} - \mathbf{x}_{jm}\right)^2}{\sigma_m^2}\right)^{-\alpha_{RQ}} \tag{2.41}$$

The rational quadratic kernel is an infinite sum of RBF kernels with different length scales, in which α_{RQ} is a scale mixture parameter.

2.3.3 Hyperparameter optimization

Hyperparameters that govern a Gaussian random field can be optimized using a maximum likelihood method. Likelihood takes into account all the available evidence about $\mathbf{x}$, and is a function of the hyperparameter(s) $\boldsymbol{\theta}$. This likelihood is more specifically termed a marginal likelihood to emphasize that the model is non-parametric (Rasmussen & Williams, 2004).

When the likelihood function is maximized, a maximum likelihood estimate is obtained. In practice, it is preferable to maximize the logarithm of the likelihood function, which is completely equivalent and computationally easier to maximize (Stein, 2012, p. 269):

$$\log p(\mathbf{y} \mid \mathbf{x}, \boldsymbol{\theta}) = -\frac{1}{2}\mathbf{y}^T \mathbf{K}^{-1}\mathbf{y} - \frac{1}{2}\log|\mathbf{K}| - \frac{N}{2}\log 2\pi \tag{2.42}$$

where the first term on the right-hand side is the complexity penalty term and the second term is the data-fitting term.

2.3.4   Performance metrics

To measure how well a GPR model performs, two performance metrics are calculated during a leave-one-out cross-validation process. As the name indicates, a sample is removed from the data set, then predicted for using a GPR model constructed without that sample. The mean-square error (*MSE*) is used,

$$MSE = \frac{1}{N} \sum_{i=1}^{N} (\hat{y}_i - y_i)^2 \tag{2.43}$$

in conjunction with the maximum percent error, where each value is calculated as

$$\% \, Error = \frac{|\hat{y}_i - y_i|}{y_i} \times 100 \tag{2.44}$$

2.3.5   Optimization using expected improvement

With a tuned GPR model in place, a criterion called expected improvement can be used as figure of merit for an optimization process. If the uncertainty at an unknown $y(\mathbf{x})$ is treated as the realization of a normally distributed RV Y described by a given GPR model, a normal density function with a mean and standard deviation is obtained for $y(\mathbf{x})$. If $f_{min} = \min\left(y^{(1)}, \ldots, y^{(n)}\right)$ is the current best function value (minimum), then the probability that the value of f will be "better" (or lower) than f_{min} while within the bounds of the standard error can be calculated (Jones, Schonlau, & Welch, 1998),

$$\mathbb{E}\big[I(\mathbf{x})\big] \equiv \mathbb{E}\big[\max(f_{min} - Y, 0)\big] \tag{2.45}$$

$$\mathbb{E}\big[I(\mathbf{x})\big] = (f_{min} - \hat{y}) \, \Phi\left(\frac{f_{min} - (\hat{y})}{s}\right) + s\phi\left(\frac{f_{min} - (\hat{y})}{s}\right) \tag{2.46}$$

where $\mathbb{E}\big[I(\mathbf{x})\big]$ is the expectation of the improvement at the point $\mathbf{x}$, $\hat{y}$ is the predicted value at $\mathbf{x}$ based on the GPR model, Φ is the standard normal cumulative density function, ϕ is the standard normal probability density function, and s is the standard error (Jones *et al.*, 1998).

CHAPTER 3

AERODYNAMIC PERFORMANCE OF THE ORIGINAL WING

To propose any improvements to an existing design, it is necessary to first establish the baseline performance of this design. In this chapter, the original wing on the Hydra S45 Bàalam is modeled and studied so that its aerodynamics can be better understood. More specifically, the performance of the wing, with and without the detachable upswept blended winglet that is part of the original S45 model, is investigated.

3.1 Geometric Representation

The aerodynamic characteristics of a wing can be studied independently from the rest of an aircraft by considering its equivalent Engineering Sciences Data Unit (ESDU) wing planform (ESDU, 1976). Using this representation, the wing is straightened to remove cranks, if any, and extended into the fuselage by extrapolation. For an already straight-tapered wing planform, such as that of the Hydra S45 Bàalam (excluding the winglet), this results in a straightforward linear extrapolation to the centre plane of the full aircraft. The resulting equivalent wing is shown in Figure 3.1. Mathematically, this linear extrapolation can be expressed as,

$$c_{root,0} = c_{tip} + \frac{b}{b_{wing}} \left(c_{root} - c_{tip} \right)$$

(3.1)

The area and span of one equivalent wing are thus, respectively,

$$b_{1/2} = b_{fus} + b_{wing}$$
$$S_{1/2} = A_{fus} + A_{wing}$$

(3.2)

The values of relevant physical parameters for the Hydra S45 Bàalam are summarized in Table 3.1 and correspond to those indicated in Figure 3.1.
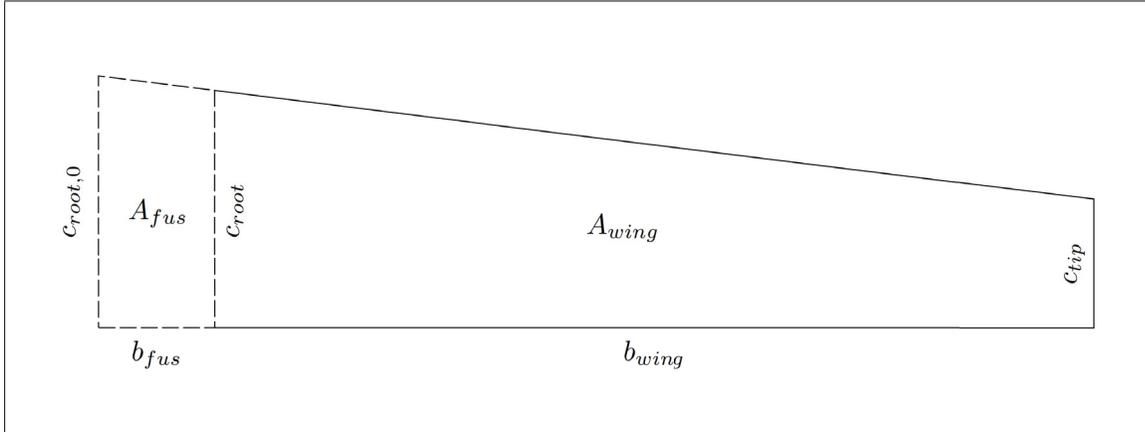
Figure 3.1   ESDU representation for a straight-tapered wing

Table 3.1   Geometric parameters for the Hydra S45
Bàalam

Symbol	Parameter	Value
b_{fus}	Fuselage radius (m)	0.323
b_{wing}	Span of one real wing (m)	2.450
$b_{1/2}$	Span of one equivalent wing (m)	2.773
$c_{root,0}$	Extrapolated root chord (m)	0.702
c_{root}	Root chord (m)	0.665
c_{tip}	Tip chord (m)	0.359
A_{fus}	Extrapolated fuselage area (m^2)	0.220
A_{wing}	Area of one real wing (m^2)	1.252
$S_{1/2}$	Area of one equivalent wing (m^2)	1.472

The shape of a wing can be further described by additional dimensionless geometric parameters. Two dimensionless characteristics often encountered in aerodynamic wing design are the

taper and aspect ratios, respectively defined using the full span b and planform area of both wings S as,

$$\lambda = \frac{c_{tip}}{c_{root,0}} \tag{3.3}$$

$$AR = \frac{b^2}{S} \tag{3.4}$$

A set of angles is used to describe the position of the wing tip relative to the wing root and to account for the three-dimensionality of a wing. Of interest are the sweep and dihedral angles, although others exist. The wing sweep angle (Λ) is most commonly defined as the angle that the quarter-chord line of the wing ($c/4$) makes with the lateral axis of the aircraft; however, it is occasionally defined relative to the line traced by the leading edge of the wing (LE). The dihedral angle (Γ) is the angle that displaces a wing upward and out of the horizontal plane. The values for all relevant supplementary parameters are summarized in Table 3.2.

Table 3.2   Dimensionless parameters for
the Hydra S45 Bàalam

Symbol	Parameter	Value
λ	Taper ratio	0.512
AR	Aspect ratio	10.14
$\Lambda_{c/4}$	Quarter-chord sweep angle ($^\circ$)	4.8
Λ_{LE}	Leading-edge sweep angle ($^\circ$)	6.4
Γ	Dihedral angle ($^\circ$)	0

A final parameter which describes the wing is the mean aerodynamic chord ($\bar{c}$), which is used as reference length to calculate the chord-based Reynolds number. For a constant taper wing (ESDU, 1976), equation (3.5) is obtained:

$$\frac{\bar{c}}{c_{root,0}} = \frac{2}{3}\frac{1+\lambda+\lambda^2}{1+\lambda}$$

(3.5)

to obtain $\bar{c}$ as 0.55 m.

An isometric view of the 3D wing to be analyzed is shown in Figure 3.2, with the Cartesian coordinate system displayed. The same definition of coordinate axes is used throughout this work, and the origin is placed at the leading edge of the wing root.
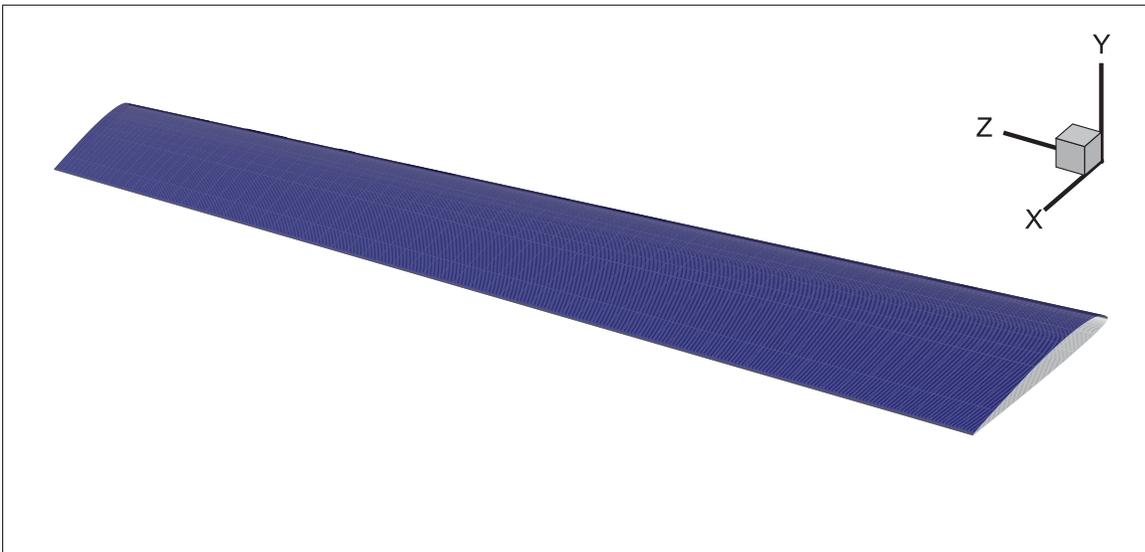
Figure 3.2   Isometric view of the 3D wing to be analyzed

3.2   Representation of the Upswept Blended Winglet

The winglet on the Hydra S45 Bàalam is swept upward and backward. The local chord length of the winglet decreases from the interface with the main wing gradually until it vanishes into a point. Owing to the strong curvature which leads to high rates of change in the geometry, the variation of parameters along the span of the winglet was deemed the most efficient way of detailing the winglet geometry. Spanwise distributions are plotted in Figure 3.3 for the chord length, and for the leading-edge sweep angle and dihedral angle in Figure 3.4. The values are normalized using the span of the winglet ($b_{winglet}$) of 0.206 m.
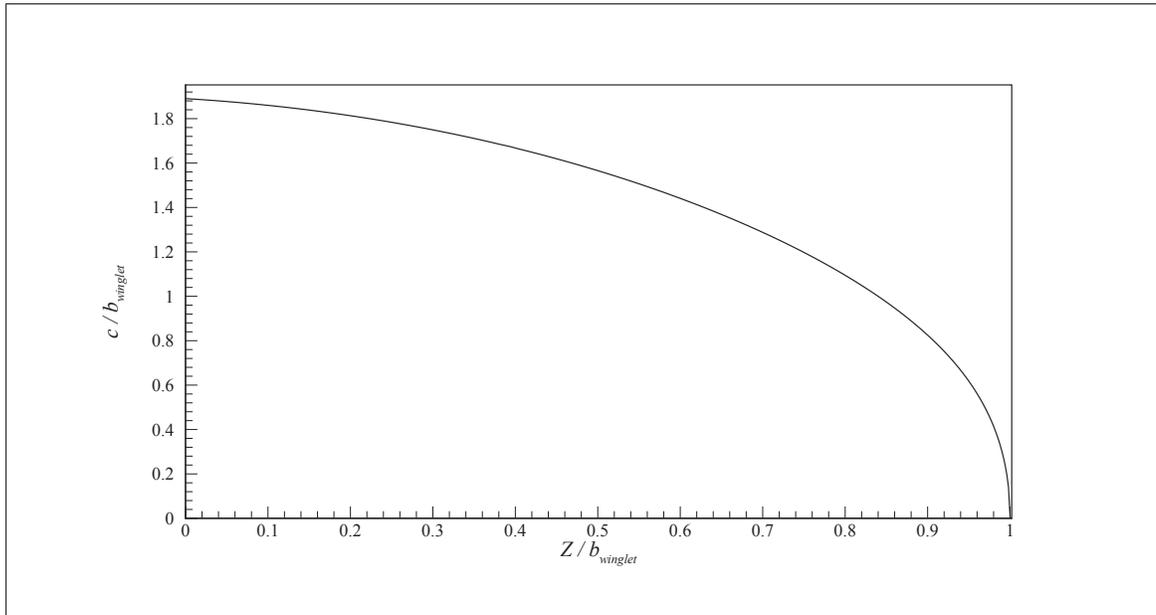
Figure 3.3   Spanwise chord length of the Hydra S45 Bàalam winglet
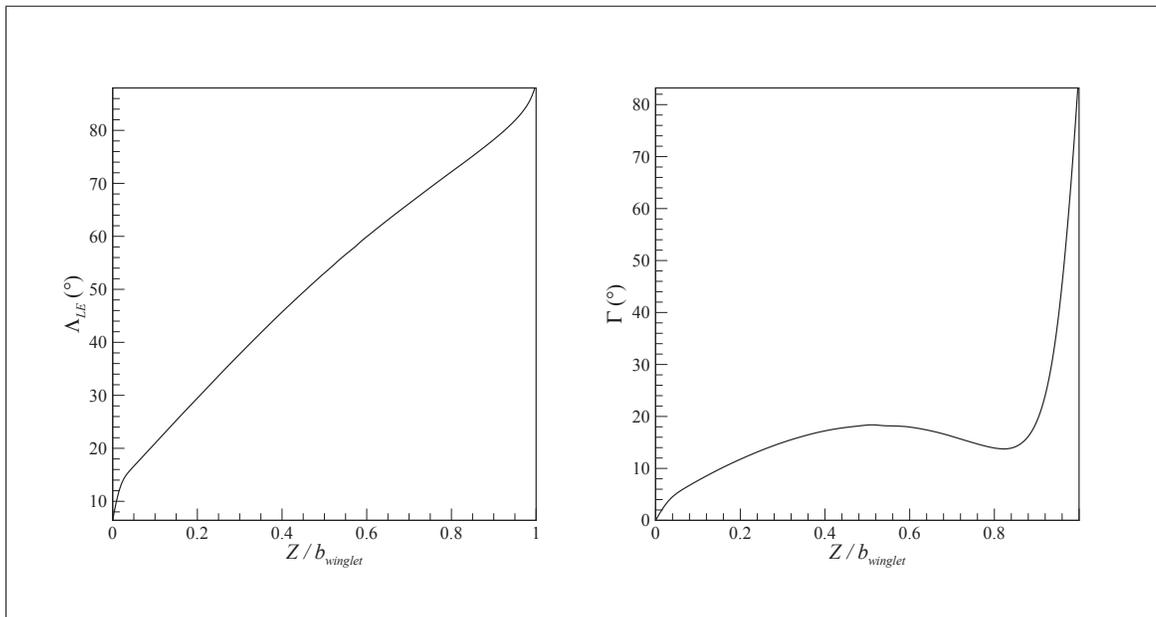
Figure 3.4   Spanwise sweep and dihedral angles for the Hydra S45 Bàalam winglet

The top and side views of the winglet can be identified in Figures 0.1 and 0.2 in the Introduction. The isometric view for the wing with the winglet attached is presented in Figure 3.5.
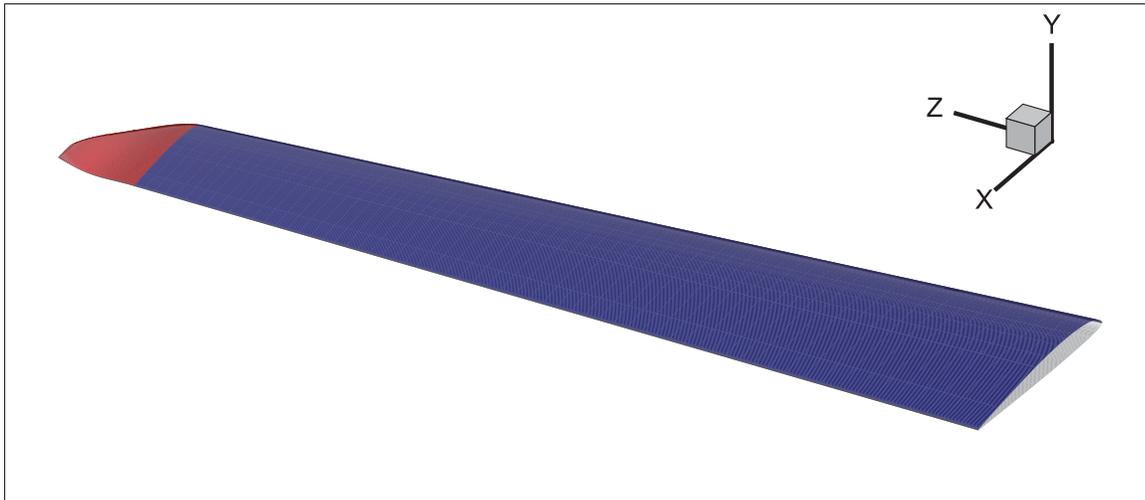
Figure 3.5   Isometric view of the wing to be analyzed including the winglet

3.3   Flight Conditions

To determine the aerodynamic performance of the Hydra S45 Bàalam wing, the flow field imposed around the modeled wing needs to be representative of flight conditions typically encountered during missions. The most important airspeeds in aviation have standard definitions which convey the flight capabilities and normal operation envelope of an aircraft.

The flight characteristics deemed useful to gain an understanding of the flow that a wing is subjected to during flight are the following (Jewel, 1965):

a. Stall speed – this is the minimum steady flight speed at which the aircraft can fly controllably while capable of producing sufficient lift to balance its weight.

b. Takeoff speed – this is the groundspeed at which the aircraft can produce enough lift during the takeoff phase to leave the ground.

c. Cruise speed – this speed is generally where flight is efficient and safe in that it tends to be near both the design point and the centre of the flight envelope.

d. Never-exceed speed – this is the maximum safe speed at which the aircraft can be operated in smooth air.

e. Velocity of normal operations – this is the maximum structural cruising speed, and is set such that structural integrity is maintained even under the influence of substantial gust loads.

An additional speed, the surveillance speed, is critical here: as a surveillance/reconnaissance UAV, this is the design speed for Hydra S45 Bàalam. All the aforementioned airspeed values for the S45 UAV are summarized in Table 3.3. Groundspeed, in knots (abbreviated kt), is the horizontal speed of an aircraft relative to a fixed ground. Indicated airspeed, in knots-indicated airspeed, or kias, is obtained from the dynamic pressure measured by the pitot-static system, and includes wind effects compared to groundspeed.

Table 3.3   Hydra S45 Bàalam flight characteristics

Symbol	Parameter	Value
V_s	Stall speed (kt or kias)	35
V_{TO}	Takeoff speed (kt)	40
V_C	Cruise speed (kt)	$50 - 55$
V_{ne}	Never-exceed speed (kt or kias)	90
V_{no}	Velocity of normal operations (kias)	$80 - 90$
−	Speed of surveillance or patrolling (kias)	$50 - 55$

The typical expected mission profile for a flight for surveillance is illustrated in Figure 3.6. The segments lengths are for representation only and do not indicate relative durations of flight segments. The Hydra S45 Bàalam has an autonomy of approximately 12 hours, most of which are expected to be spent at surveillance or cruise speed. It can be observed that surveillance is carried out at cruise speed.
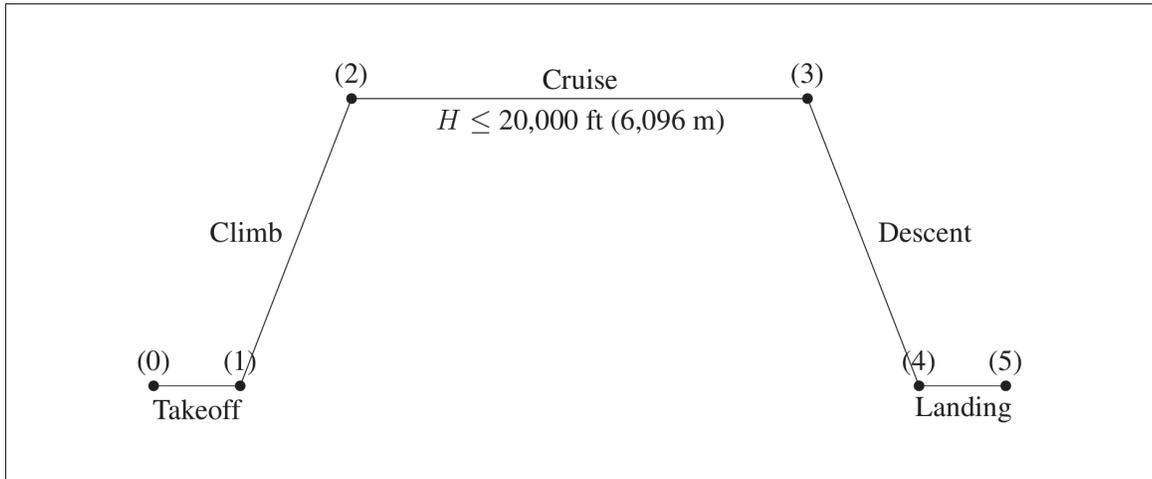
Figure 3.6   Typical mission profile for a surveillance UAV

3.4   Computational Approach

The flow field around the Hydra S45 Bàalam wing is calculated using CFD software. Pressure and wall shear stress acting on the wing surface are integrated to determine the total force acting on the wing. However, if detailed information on the distribution of forces on different regions on the wing is desired, the full wing surface needs to be partitioned into slices before simulating the flow so that integrations can be performed separately for each slice.

For the wing without the winglet, 20 slices of equal span were used to produce 20 spanwise force and moment values. This number of points was deemed sufficient to accurately capture the behaviour of forces and moments along the span of the wing (Figure 3.7). For the wing including the winglet, 12 slices of equal span were used for the main wing with an additional 12 logarithmically-spaced slices along the span of the winglet (Figure 3.8).

The boundary conditions are stated in § 2.2.7. A transient formulation was used to overcome convergence difficulties introduced by the transition model and to allow solutions to be obtained at high angles of attack. With the implicit solver, a physical time step size of 0.001 s was found to retain numerical stability, for which 300 total time steps sufficed to obtain a developed solution at the residual target of 1×10^{-5} on all flow and turbulence variables. The combined choice of timestep size and number of timesteps is justified by the need for the solu-
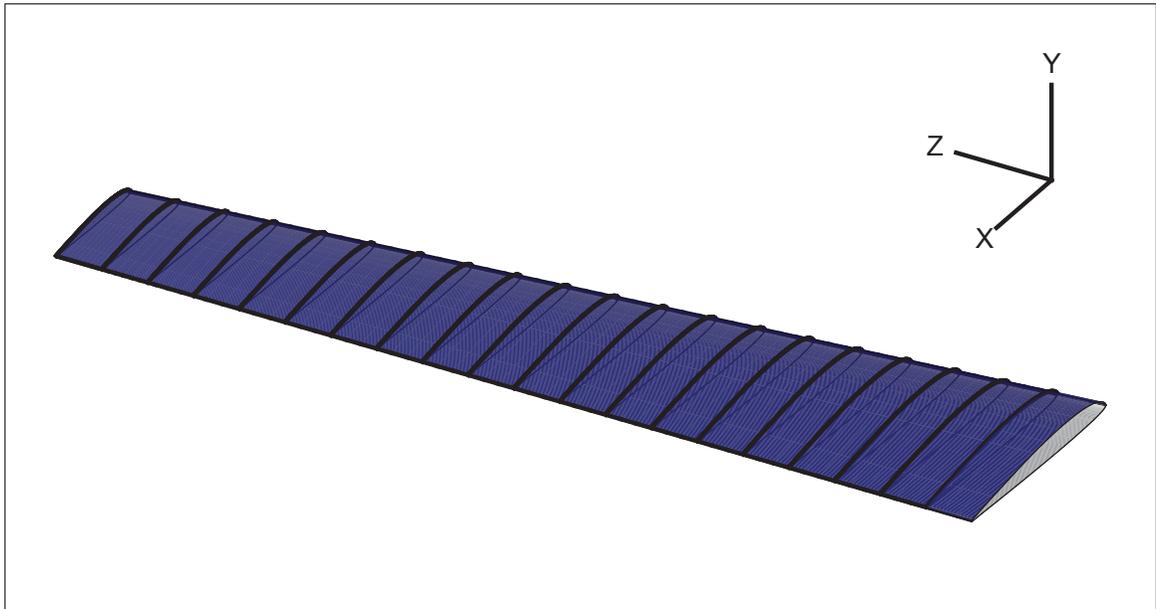
Figure 3.7   Sectioned wing without winglet
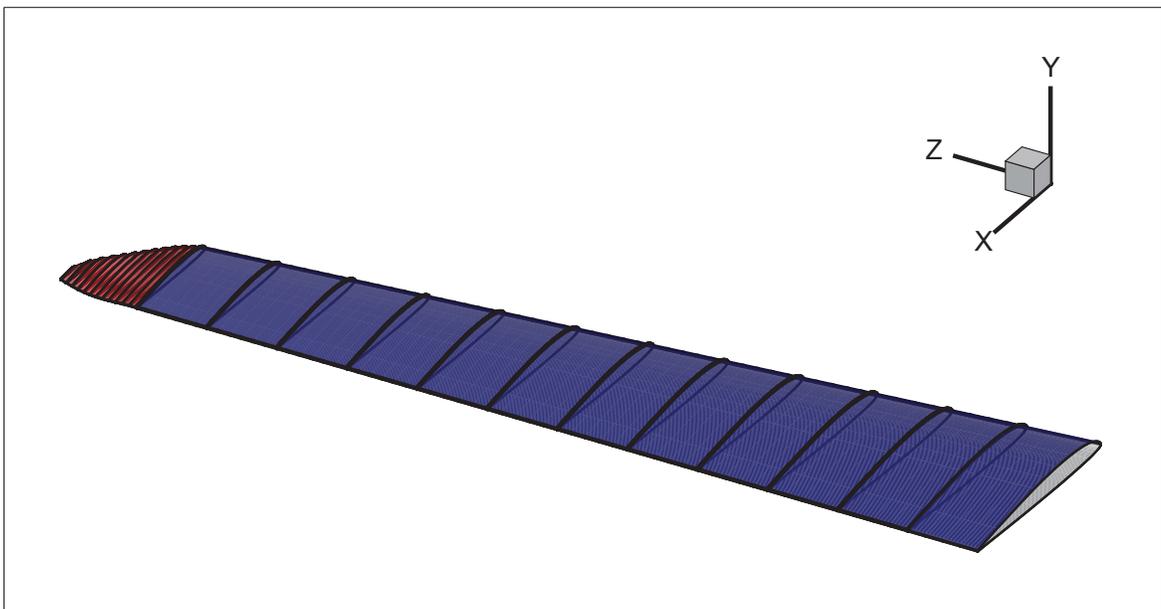
Figure 3.8   Sectioned wing with winglet

tion to converge (particularly in the first few timesteps where divergence occurs more readily) which restricts the maximum timestep size, and by the need to achieve a sufficiently developed wing tip vortex to properly account for the induced drag. This is demonstrated in Figure 3.9,

where a flow visualization image is shown. In this flow visualization, the vortex core can be identified as the thick black line passing in the centre of the shed vortex. The vortex core extraction method used is the λ_2 method proposed by Jeong & Hussain (1995), where λ_2, which always takes a negative value, is the second eigenvalue of the symmetric tensor $S^2 + \Omega^2$. The vortex is represented using an iso-surface of λ_2, where a value of -4275 is used for λ_2. This value was obtained by examining the contour of λ_2 in the vortex region shown in Figure 3.10 and selecting a value for λ_2 where the vortex begins roughly.

Figure 3.9   Flow visualization of the wing tip vortex at $\alpha = 0°$ and $Re = 1.0x10^6$

The transition SST model is used as turbulence model, with curvature correction, and turbulence kinetic energy production limiter and production Kato-Launder enabled in ANSYS Fluent. A coupled pressure-velocity scheme is used with second-order schemes for the pressure, momentum, k, ω, γ, and Re_θ. A second-order implicit time discretization is used with the default Courant number of 200, which serves to control the pseudo-time term, as opposed to the physical-time term which is controlled using the timestep size (ANSYS Inc., 2006) (set
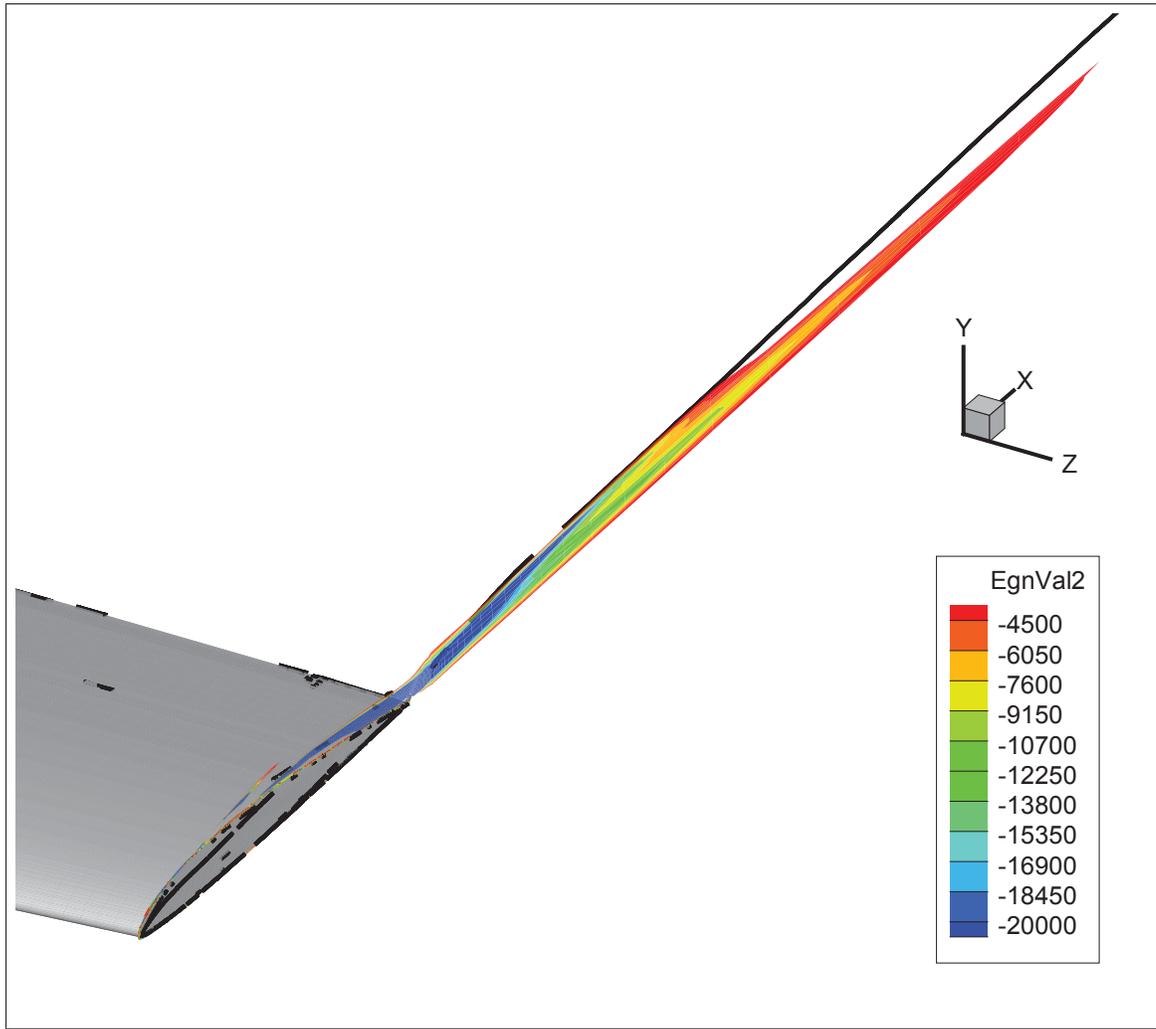
Figure 3.10   Contour of λ_2 near the wing tip at $\alpha = 0°$ and $Re = 1.0x10^6$

to 0.001 s). Final values are obtained by time-averaging the results over the last 10 timesteps to account for numerical dissipation and small flow fluctuations that may be present.

3.5   Results

The force and moment coefficient variations with the angle of attack obtained from the CFD simulations are plotted in Figures 3.11 through 3.20. Force coefficients are obtained by normalizing the force components using the dynamic pressure and the area of the wing without the winglet. Moment coefficients are obtained by normalizing the moment components using the

dynamic pressure, the area of the wing without the winglet, and the mean aerodynamic chord length of the wing without the winglet.

In Figure 3.11, the lift coefficient, C_L is plotted against α. Loss of lift appears very slightly at $\alpha = 12°$ and more evidently at $\alpha = 14°$ as a larger portion of the wing begins to stall. C_L for the wing equipped with the winglet is consistently superior to that for the plain wing. The supplementary C_L takes the shape of an inverted parabola, taking a value of 0.0092 at $\alpha = 0°$ and increasing decreasingly to 0.037 at $\alpha = 14°$. The percentage increase in C_L relative to the plain wing owing to the winglet is largest at $\alpha = 0°$ with 4.23 %, and sporadically decreases to 2.31 % at $\alpha = 10°$, point at which it increases again.
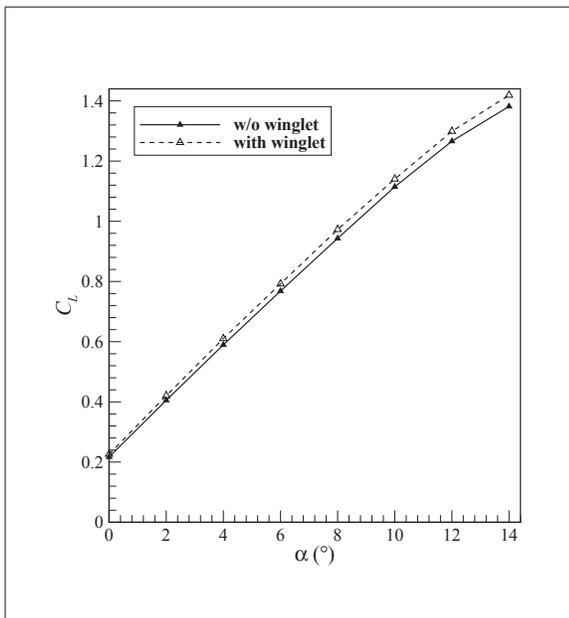
Figure 3.11 Lift curve for the original wing
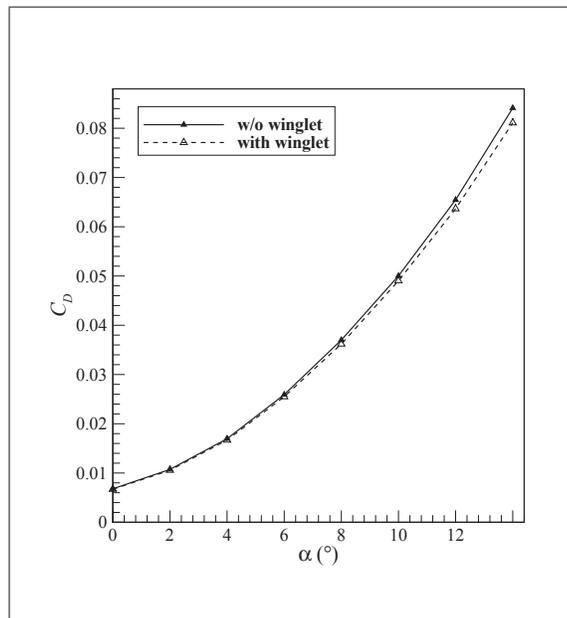
Figure 3.12 Drag curve for the original wing

In Figure 3.12, the drag coefficient, C_D is plotted. This total drag coefficient is the sum of two components, one due to the pressure field, $C_{D,pres}$ and the other due to wall shear stress, $C_{D,visc}$. The $C_{D,pres}$ and $C_{D,visc}$ curves are shown in Figure 3.13 and Figure 3.14, respectively. From this drag breakdown, the belief that all components of drag except for frictional drag vary as C_L^2 is confirmed. This relationship implies that a plot of C_D against C_L^2 is a straight line,

so long as no part of the wing begins stalling. On the horizontal axis, $C_L^2 = 0$, which, when used in the best linear fit equation, yields the zero-lift drag coefficient, $C_{D,0}$. Using values for $\alpha = 0°$ to $10°$, the linear approximation $C_D = 10^{-3} \cdot (36.3C_L^2 + 4.72)$ with a coefficient of determination $R^2 = 0.99973$ is obtained for the wing without the winglet. Similarly, $C_D = 10^{-3} \cdot (34.7C_L^2 + 4.51)$ with $R^2 = 0.99936$ is obtained for the wing equipped with the winglet. As a result, $C_{D,0}$ values are obtained as 4.72×10^{-3} and 4.51×10^{-3} for the wing without and with the winglet, respectively. This difference represents a 4.45 % reduction in $C_{D,0}$ of the plain wing, and is likely due to the distribution of increasingly short chord lengths along the winglet. Shorter local chords are responsible for lower local Reynolds numbers, placing a greater proportion of the wing in a laminar flow regime and thus lowering $C_{D,0}$ overall.
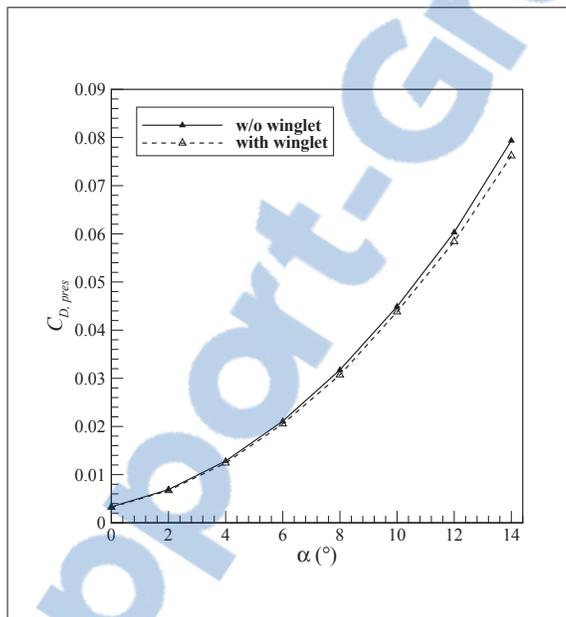
Figure 3.13   Pressure drag curve for the original wing
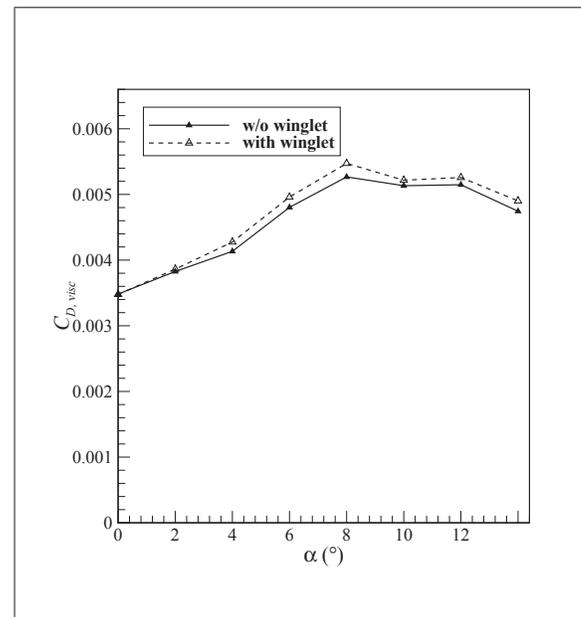
Figure 3.14   Viscous drag curve for the original wing

Values for C_D are observed to be consistently lower when the winglet is used (Figure 3.12). Figure 3.14 demonstrates that the viscous drag, $C_{D,visc}$, behaves in approximately the same way for the wing without or with the winglet. This entails that the differences in C_D are, by and large, sensibly exclusively attributable to $C_{D,pres}$ differences. This implication is in

keeping with the known behaviour of winglets in that their primary objective is to reduce the intensity of wing-tip vortices and therefore the induced drag. Comparing $C_{D,pres}$ values, the reduction obtained increases increasingly with the angle of attack, from 0.09×10^{-3} at $\alpha = 0°$ to 3.17×10^{-3} at $\alpha = 14°$. The percent improvements on $C_{D,pres}$ do not vary much with α and exhibit no particular trend, with values between 2.42 and 3.98 % and an average of 3.06 %, relative to the plain wing. Lastly, comparing C_D values, the reduction obtained increases increasingly with the angle of attack (as was observed with $C_{D,pres}$) from 0.09×10^{-3} at $\alpha = 0°$ to 3.013×10^{-3} at $\alpha = 14°$. The corresponding percent improvements on C_D show a slow increase between $\alpha = 0°$ and $10°$, from 1.39 % to 2.00 %, followed by a more pronounced increase between $\alpha = 10°$ and $14°$, from 2.00 % to 3.58 %. This shift in slope can be explained by considering the relative influence of each drag component on the total drag: at lower α, $C_{D,visc}$ is of greater proportion of the total drag, but, as α increases, $C_{D,pres}$ increases much more quickly and growingly dominates in the total drag. From $\alpha = 0°$ to $14°$, $C_{D,pres}$ goes from constituting 51.3 % of the total drag down to only 5.64 % on the plain wing, and from 51.9 % to 6.04 % on the wing with the winglet.

The glide ratio represents the ratio of lift force to drag force. Its variation is shown in Figure 3.15. It is a direct consequence of the previously discussed results. An increase in C_L accompanied by a decrease in C_D leads to a percent increase in C_L/C_D of the combined individual percent improvements on C_L and C_D. $(C_L/C_D)_{max}$ occurs in the neighbourhood of $\alpha = 2°$ (as is confirmed by drawing a tangent to the curve going through the origin), where C_L/C_D values are 37.77 and 39.82 for the wing without and with the winglet, respectively. This difference represents a 5.42 % increase in $(C_L/C_D)_{max}$. The C_L-C_D plot, better known as the drag polar, is shown in Figure 3.16. This final plot also reflects the previously discussed observations on the enhanced aerodynamic performance of the wing with the winglet.

Figure 3.17 shows the variation of the side force coefficient (C_Y) with α. C_Y during steady level flight for a wing has very little effect on the motion of the aircraft in the absence of crosswinds, mainly because the right and left wing produce equal and opposite side forces in such a symmetrical flow. The presence of the winglet causes a decreasing decrease in C_Y with
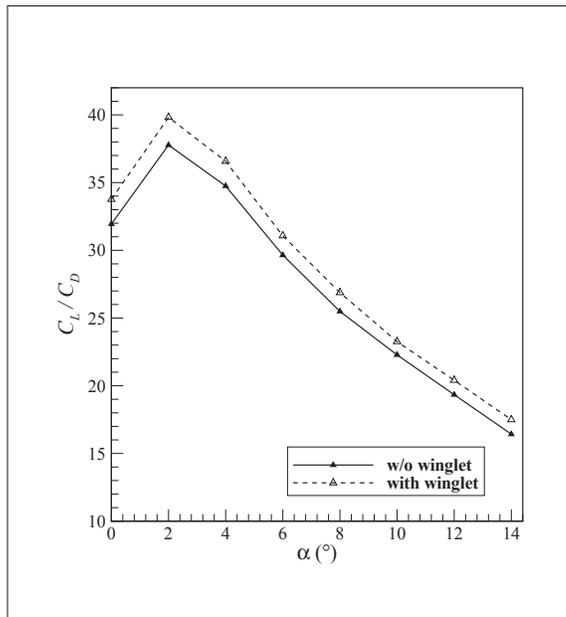
Figure 3.15   Lift-to-drag curve for
the original wing
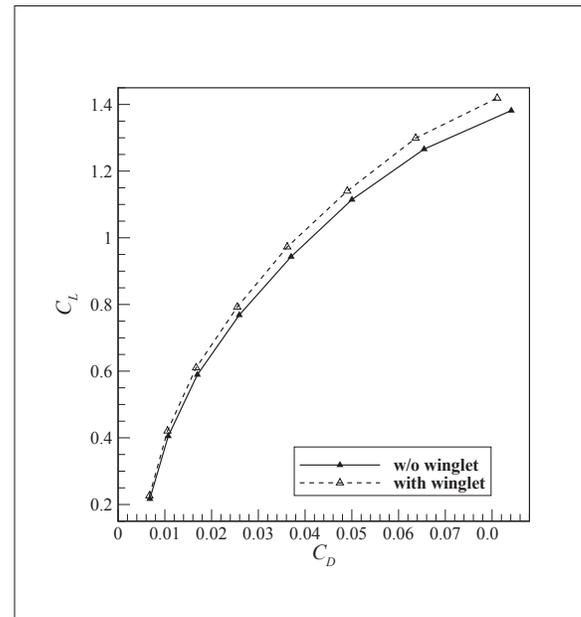
Figure 3.16   Drag polar for the
original wing

α, with a decrement of 1.85×10^{-3} at $\alpha = 0°$ to 6.55×10^{-3} at $\alpha = 14°$. This corresponds to a 66.5 % decrease in C_Y relative to the plain wing at $\alpha = 0°$ which gradually reduces to a 15.0 % decrease at $\alpha = 14°$.

Figure 3.18 shows the yaw moment coefficient (C_n) curve with α. Similarly, Figure 3.19 shows the roll moment coefficient (C_l) curve and Figure 3.20 shows the pitching moment coefficient (C_m) curve with α. The moments are calculated based on the forces on the wing presented previously acting at the centre of pressure. From the coordinate system established, the forces along the x-, y-, and z-axes are non-dimensionally C_D, C_L and C_Y, respectively, while the moments are C_l, C_n, and C_m, respectively. As such, when a force is parallel to the moment axis, it produces no moment. C_l, C_n, and C_m are all greater in magnitude for the wing equipped with the winglet relative to the plain wing. For both the right and left wings in a symmetrical flow, C_l and C_n have a zero resultant. C_m for both wings, however, is twice the value plotted in Figure 3.20. The difference in C_m values introduced by the winglet is nearly linear, such that C_m is, on average, 5.60 % higher for the wing equipped with the winglet relative to the plain wing.

Beyond the relatively global analysis of the impact of the winglet in terms of force and moment coefficients that has been done thus far in this series of results, more can be understood about how the behaviour of the flow changes in the presence of the wingtip device. Specifically, the force along the span of the wing can be plotted to paint a clearer picture of winglet aerodynamics. A force-per-unit-span measure is used, such that the spanwise integral thereof representing the area under the curve yields the total force. In Figure 3.21, the lift force per unit span, L', is plotted for $\alpha = 0°$ to $14°$ every $2°$. Likewise, the drag force per unit span, D', is plotted in Figure 3.22, and shown again in more detail in the wingtip region in Figure 3.23. The side force per unit span, Y', is shown in Figure 3.24.
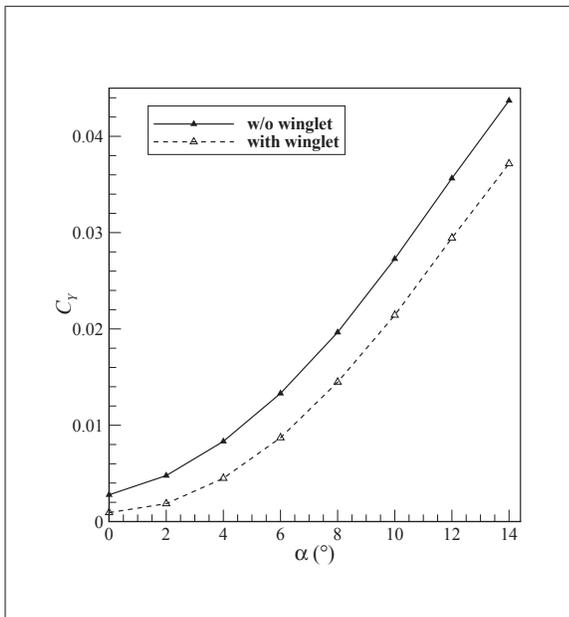
Figure 3.17   Side force curve for the original wing
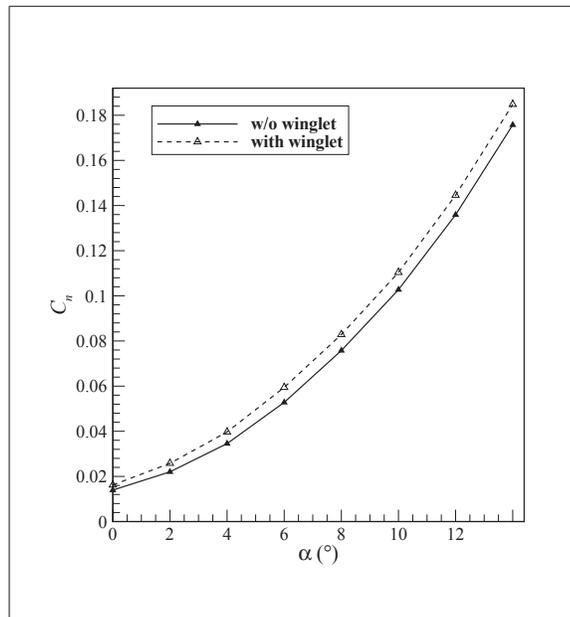
Figure 3.18   Yaw moment curve for the original wing

A prominent feature present in the spanwise force distributions is the jump in properties at the wing-winglet junction, which is likely attributable to the discontinuity in the rate of change of sweep and dihedral angles, and to a greater degree to the sudden rate of change in chord length and therefore area. The L' distribution demonstrates little beyond an extension in the span and a discontinuity in the wing area. The D' distribution shows lower drag on the wing
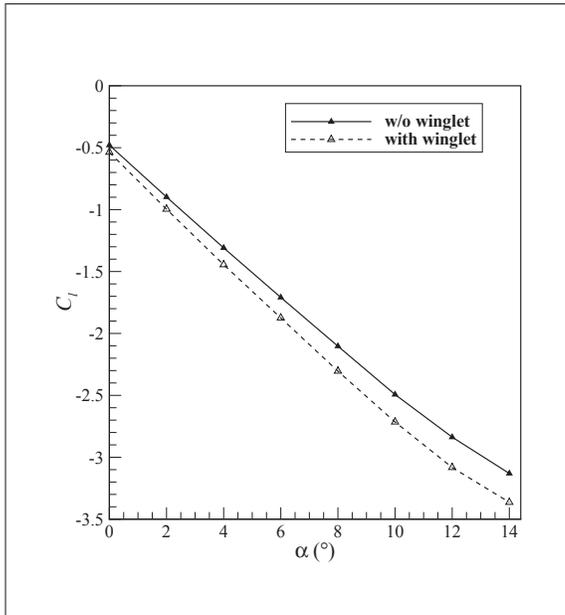
Figure 3.19   Roll moment curve for the original wing
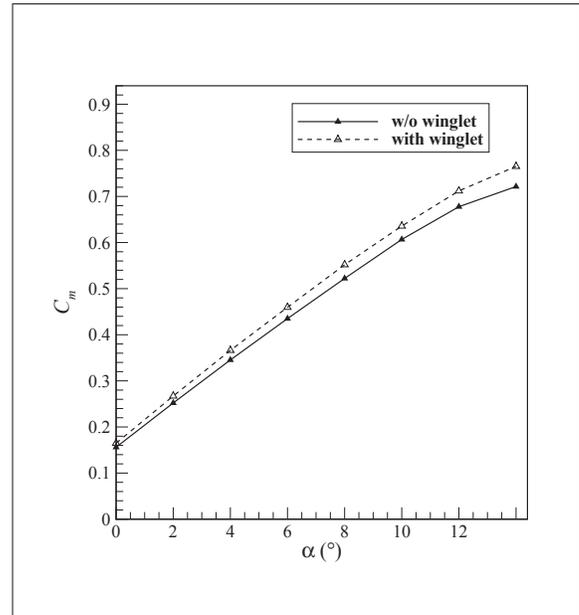
Figure 3.20   Pitching moment curve for the original wing
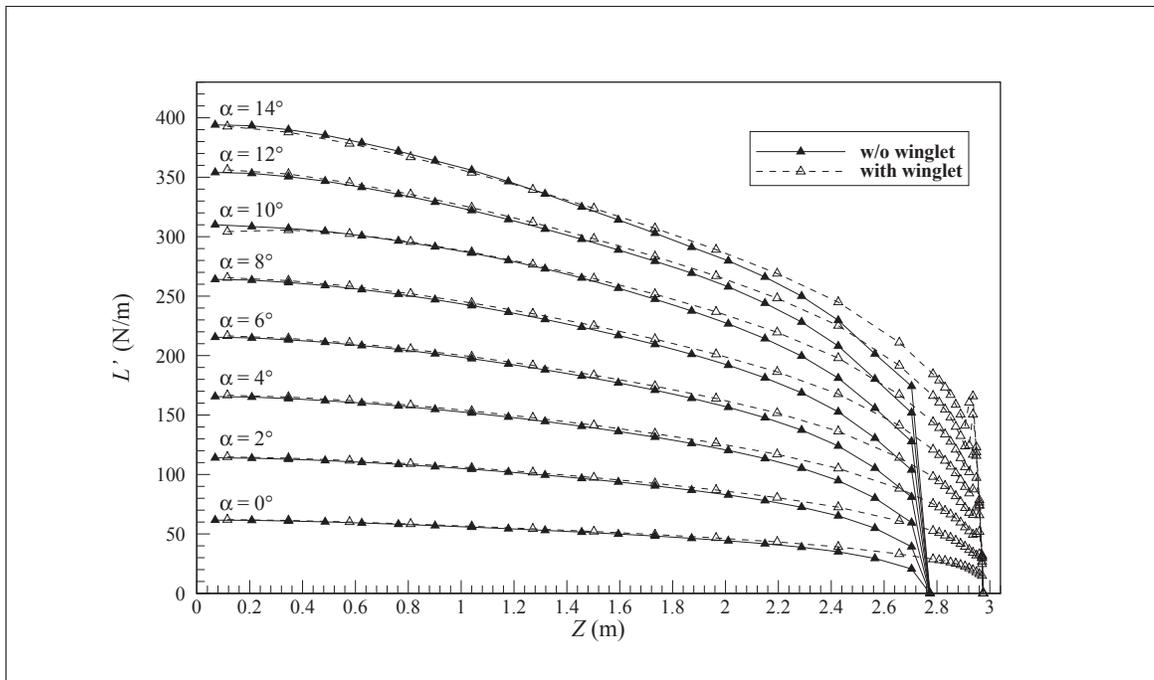
Figure 3.21   Spanwise lift distribution for the original wing
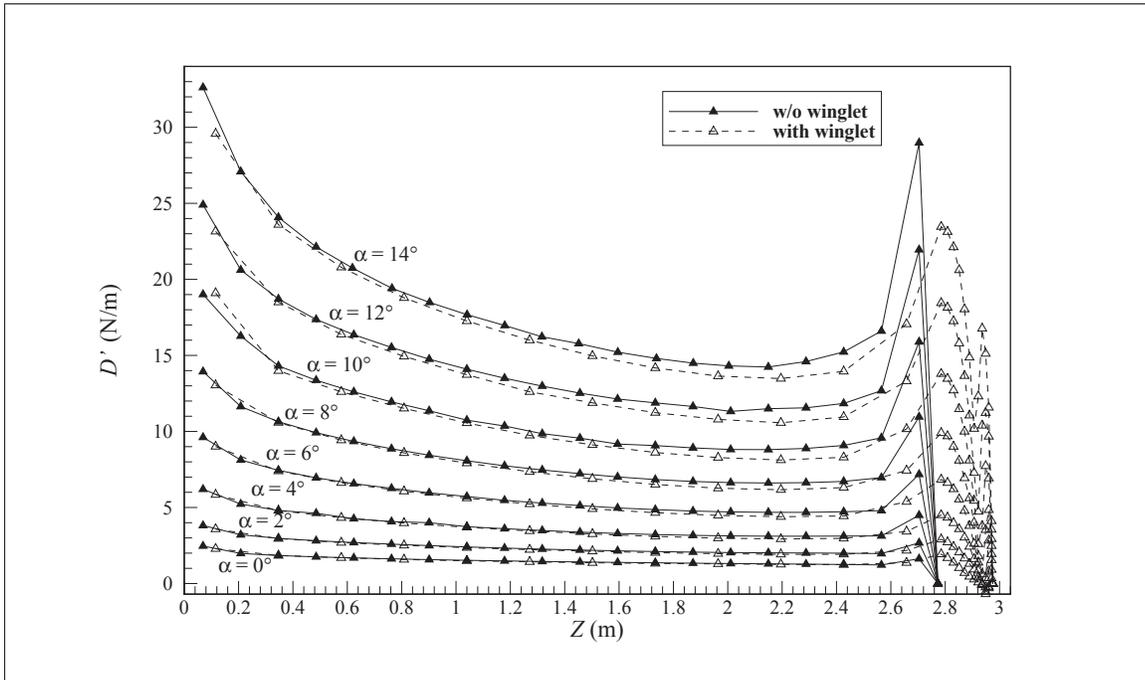
Figure 3.22   Spanwise drag distribution for the original wing
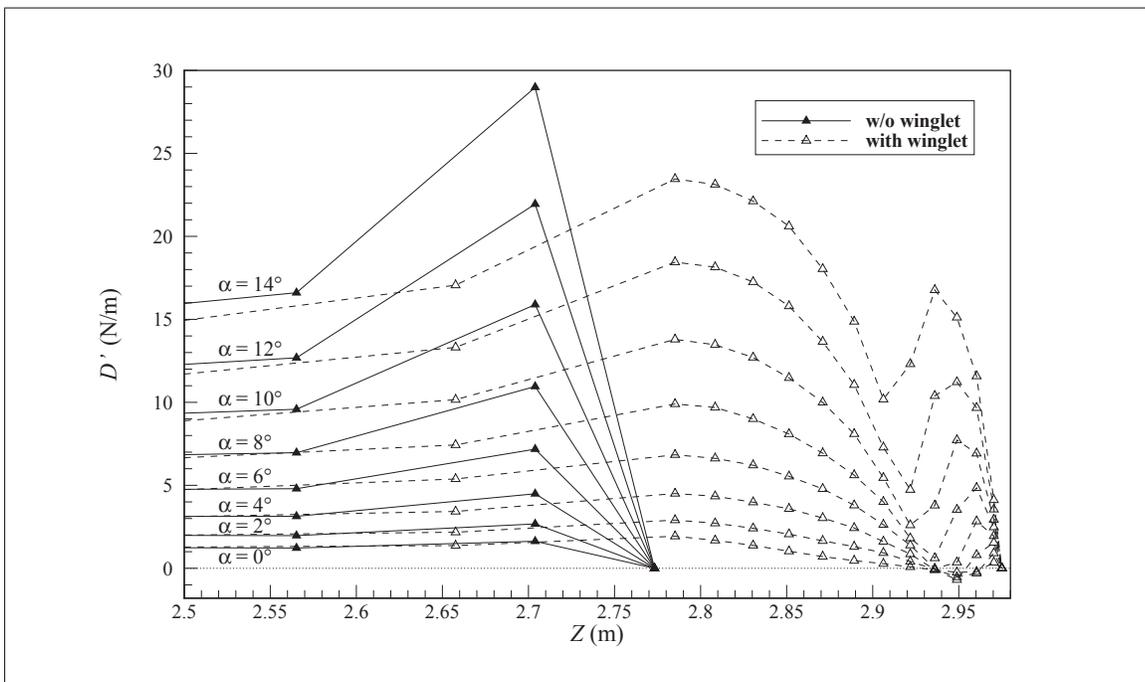
Figure 3.23   Close-up view of the spanwise drag distribution near the wing tip
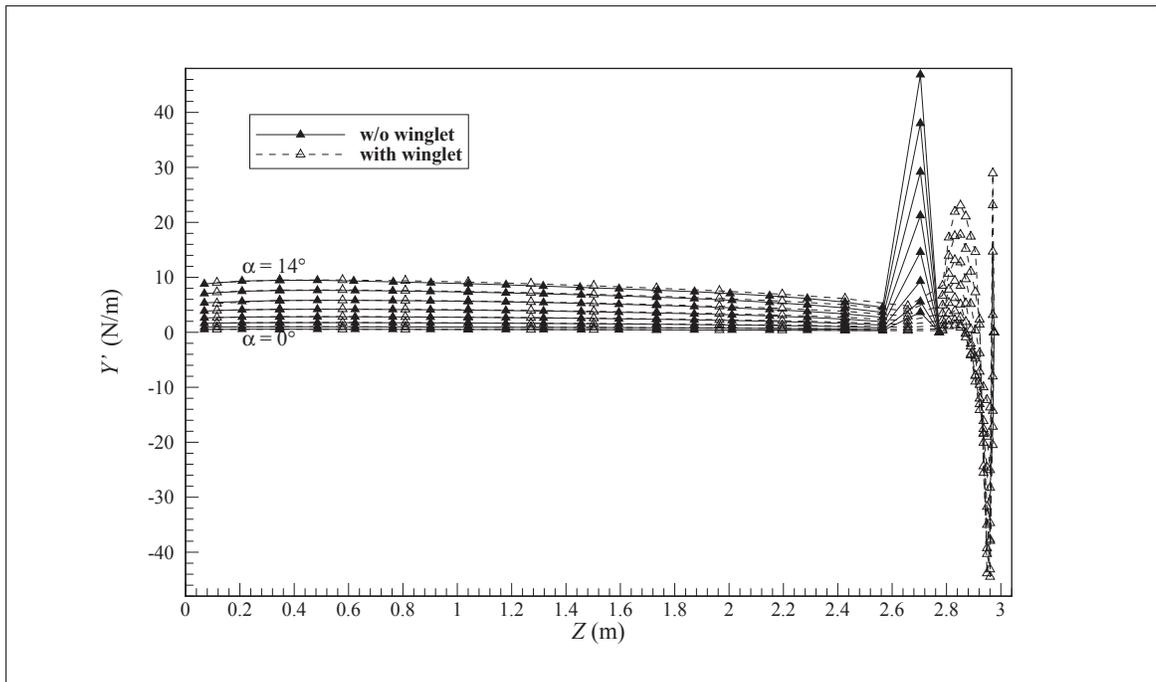
Figure 3.24   Spanwise side force distribution for the original wing

with the winglet, which is representative of the reduction in induced drag. The more detailed D' distribution also indicates that at low angles of attack (at $\alpha = 0°$ and $2°$ in Figure 3.23), the drag for a small portion of the span is negative owing to the surface curvature of the winglet. Considering the Y' distribution, diminished side force values are observed on the winglet relative to the wingtip of the plain wing. The D' and Y' distributions indicate that, in all likelihood, part of the force that would conventionally be the side force acts in the reverse direction of drag when the winglet is affixed to the wingtip of the plain wing. The Y' distribution also shows the development of a negative component induced by the winglet; this supplements the previous observation that C_Y is consistently lower with the winglet by making evident the negative portions that serve to reduce the total side force value.

Finally, images of the wing tip vortices are shown in Figures 3.25–3.32 to illustrate the impact of adding the winglet studied in this chapter and to confirm that these vortices have been properly resolved. The wing tip vortices appear to be consistently weaker for the wing equipped with the winglet relative to the wing without the winglet.

3.6 Conclusions

In this chapter, the first CFD results are explored in detail and presented. From the series of CFD simulations conducted, it is clear that the upswept blended winglet on the S45 Bàalam brings a noteworthy improvement in aerodynamic performance. The moment coefficients for the wing change significantly with the introduction of the winglet, suggesting that there is more to be understood about this winglet in terms of aircraft stability. The results obtained in this chapter suggest that the execution of CFD simulations has been carried out with success, such that the technique can be applied in Chapters 4 and 5 to evaluate aerodynamic coefficients within optimization loops.
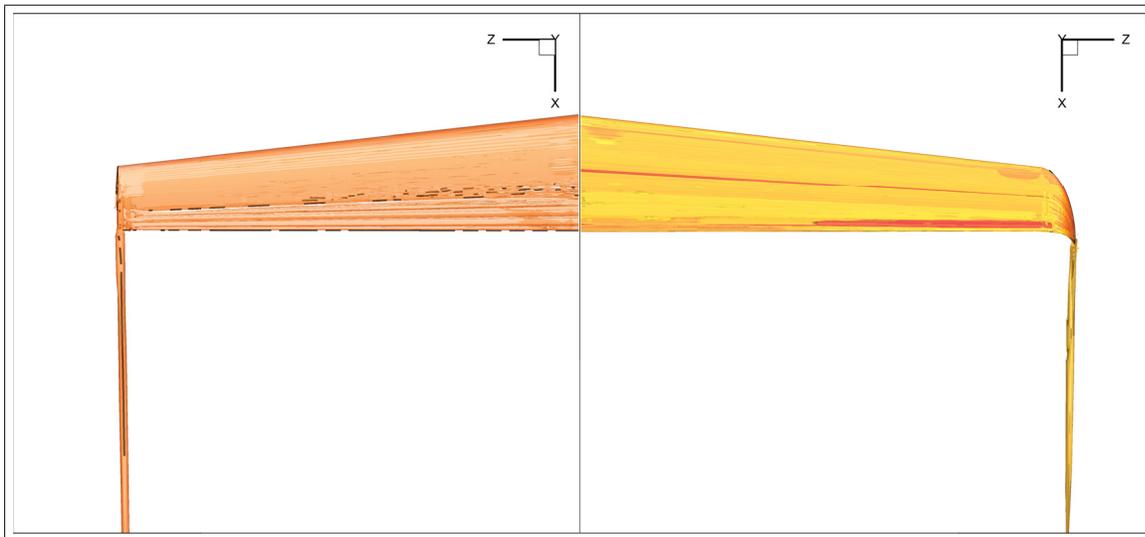
Figure 3.25   Wing tip vortex visualizations without and with the winglet at
$\alpha = 0°$ and $Re = 1.0 \times 10^6$
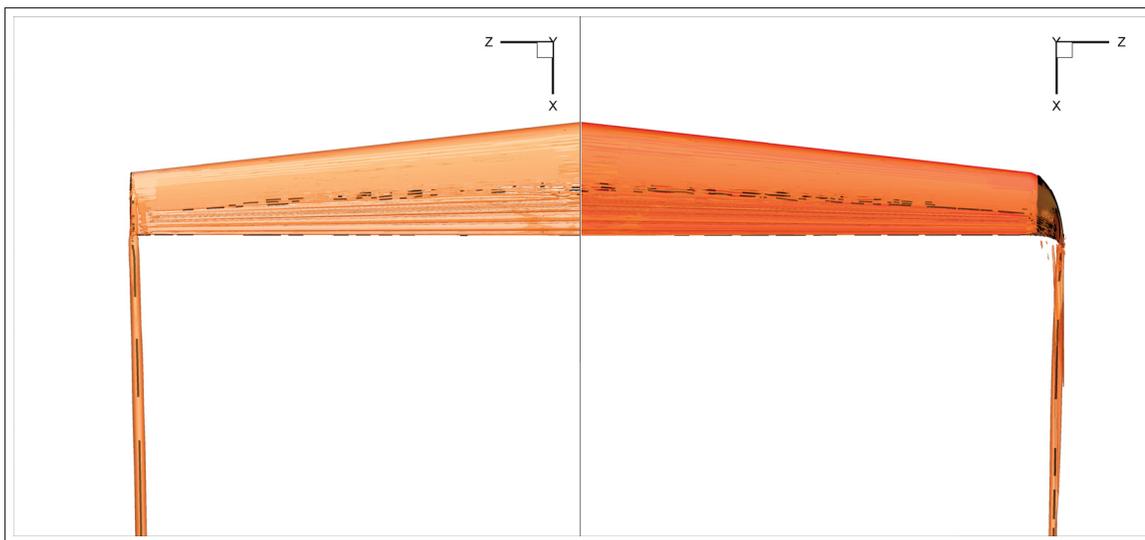
Figure 3.26   Wing tip vortex visualizations without and with the winglet at $\alpha = 2°$ and $Re = 1.0 \times 10^6$
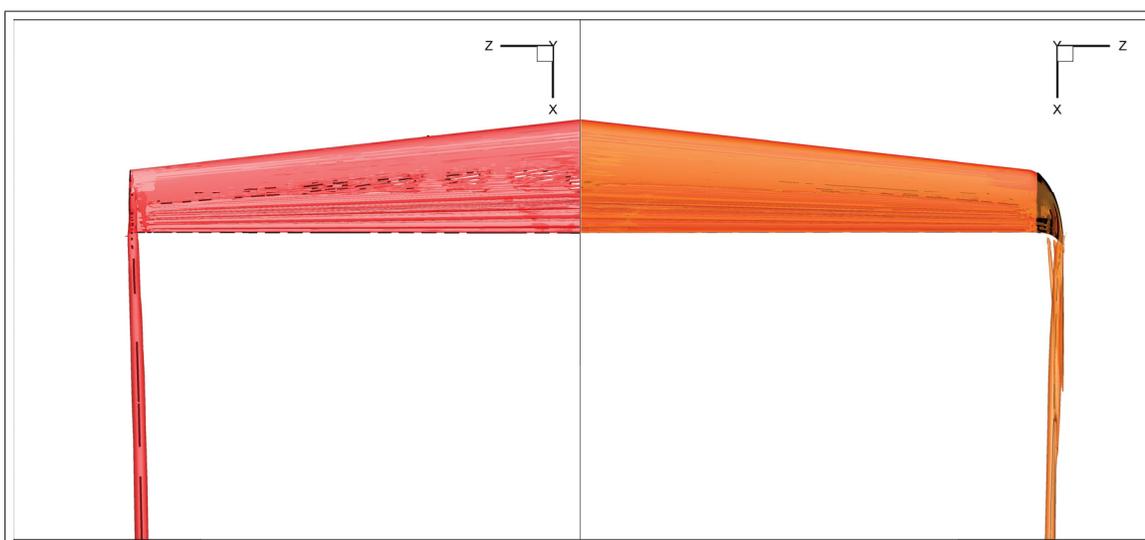
Figure 3.27   Wing tip vortex visualizations without and with the winglet at $\alpha = 4°$ and $Re = 1.0 \times 10^6$
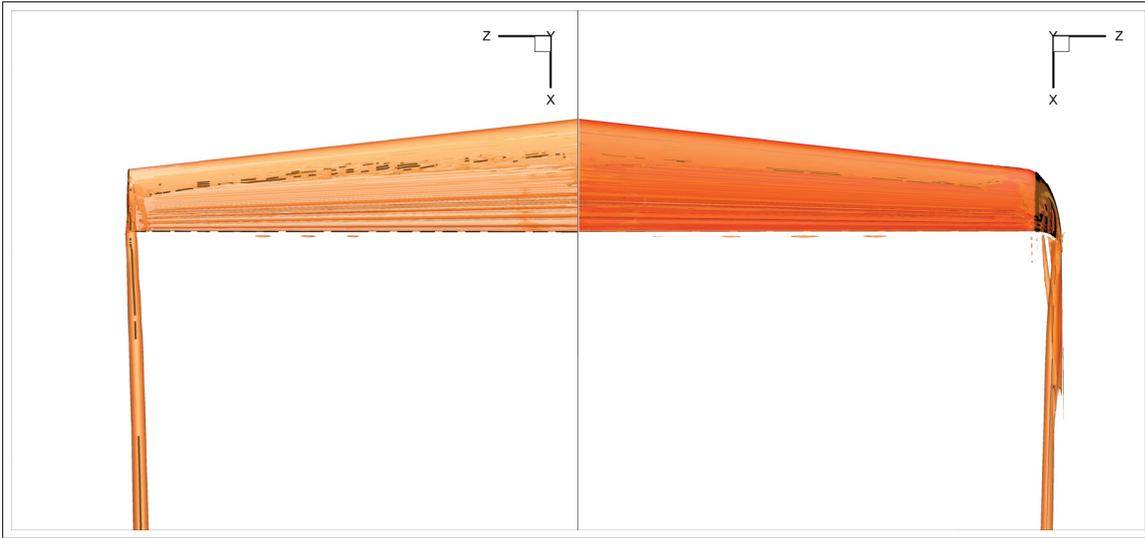
Figure 3.28   Wing tip vortex visualizations without and with the winglet at $\alpha = 6°$ and $Re = 1.0 \times 10^6$
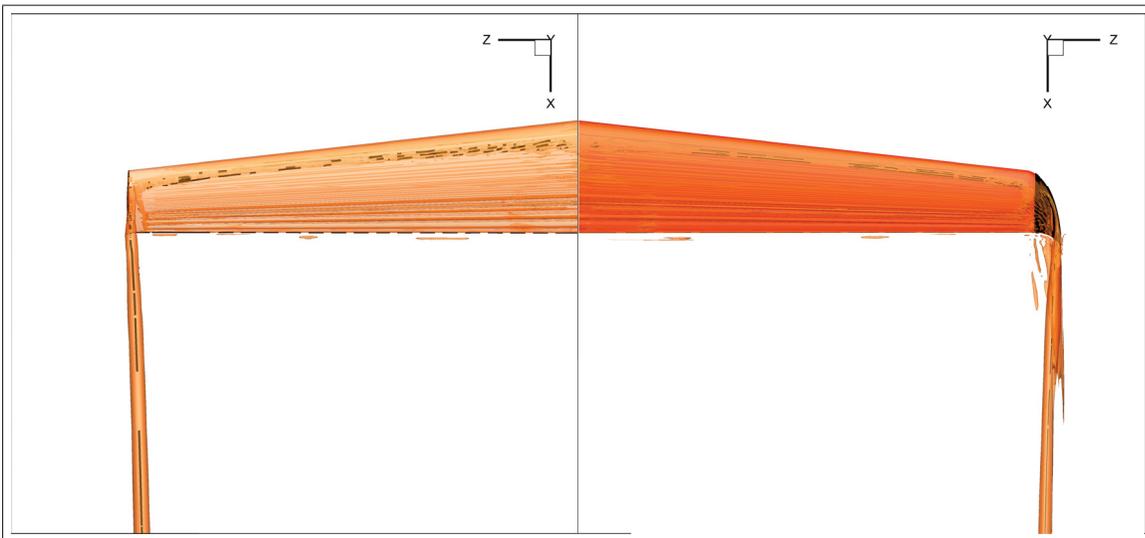
Figure 3.29   Wing tip vortex visualizations without and with the winglet at $\alpha = 8°$ and $Re = 1.0 \times 10^6$
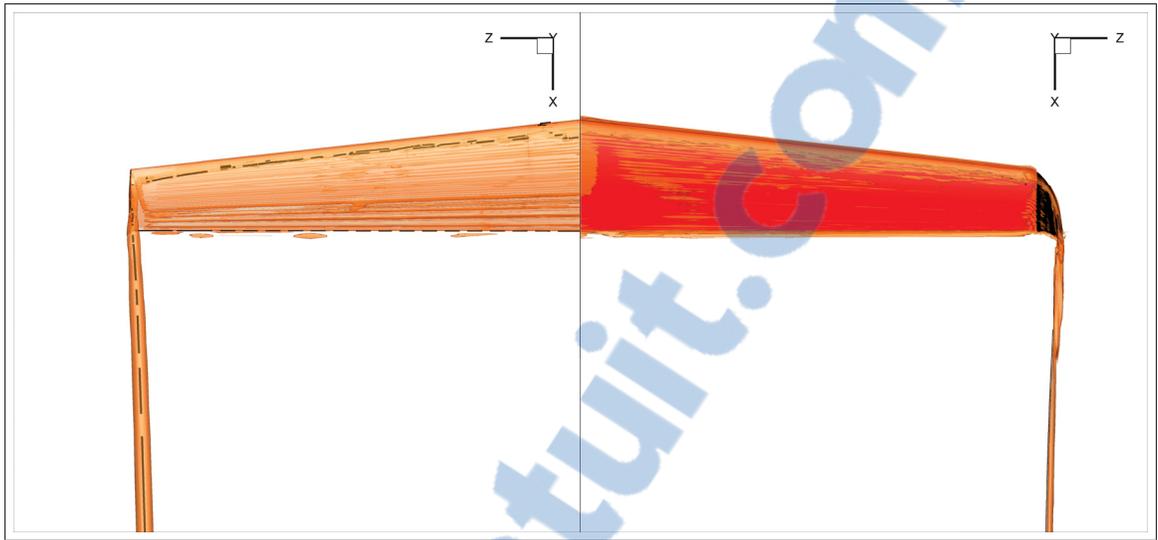
Figure 3.30   Wing tip vortex visualizations without and with the winglet at
$\alpha = 10°$ and $Re = 1.0 \times 10^6$
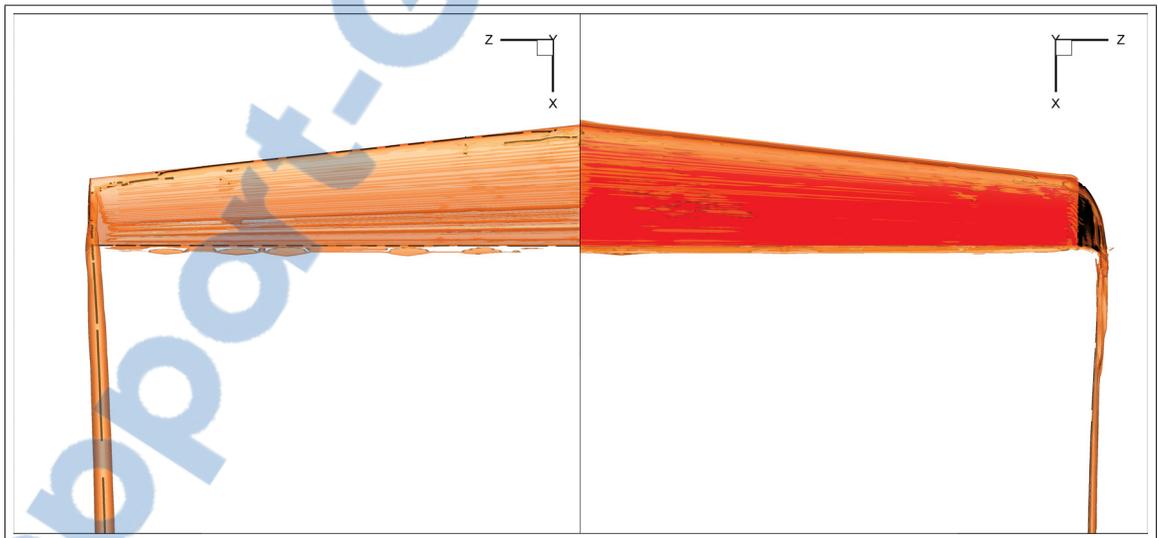
Figure 3.31   Wing tip vortex visualizations without and with the winglet at
$\alpha = 12°$ and $Re = 1.0 \times 10^6$
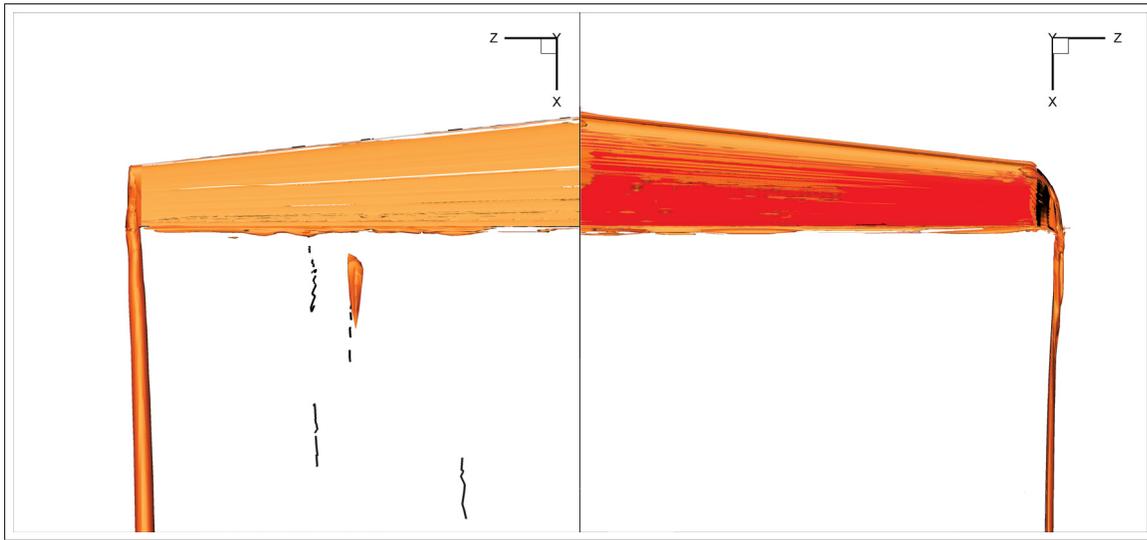
Figure 3.32 Wing tip vortex visualizations without and with the winglet at $\alpha = 14°$ and $Re = 1.0 \times 10^6$

CHAPTER 4

AERODYNAMIC OPTIMIZATION OF THE ORIGINAL WING

In this chapter, an approach to wing parametrization is presented in the first section, wherein chosen geometric parameters of an ESDU wing are allowed to vary while two parameters, namely fuselage width and wing area, are kept constant. The fuselage width is deemed an important constant because of the modular design of the Hydra S45 Bàalam. Modifying the wing area, which directly influences the lifting capacity of the aircraft, represents a significant change in the abilities of the aircraft. Such a change is an undesirable outcome because the objective of this optimization study is to improve the aerodynamics of the existing UAV wing rather than completely redesign this wing. Major design changes can cause sizing issues such as changes in engine thrust requirements or in takeoff and landing distances. In the subsequent sections, optimization bounds are defined for the design variables, and a training set is constructed using the CFD solutions of 60 test wings to develop Gaussian process regression models to emulate the response of the CFD solver. Optimal values for the range and endurance of the aircraft are sought using the expected improvement function in two contexts: the first context is one where the aspect ratio is kept at its original value, and the second is one where the aspect ratio is free to vary. Aspect ratio is treated carefully because, although it is known that a higher aspect ratio leads to lower induced drag, the resulting wing becomes more slender as the aspect ratio increases. The thin, long wing obtained is more susceptible to bending than the relatively short and stubby original wing, which causes structural weight to be larger for the higher aspect ratio wing. This increase in structural weight causes, in turn, an increase in the wing loading, which needs to be constrained for wings with high aspect ratio.

4.1 Wing Parametrization

Using the wing planform geometric planform parameters as shown in Figure 3.1, equations can be derived for appropriate design variables, such that the real wing area (A_{wing}) and imaginary wing span representing the fuselage (b_{fus}) in the ESDU representation of the wing are

kept constant. The design variables deemed appropriate to alter chord lengths and span of the original wing are the aspect ratio and taper ratio.

Equation (4.1) is an expression for the planar area of the portion of the ESDU wing that represents the real wing. Equation (4.2) is an expression for the total ESDU wing area, with separate length components for the wing and the fuselage. Equation (4.3) expresses area of the ESDU wing that makes up the imaginary fuselage portion, and relates the resulting expression to the taper ratio, which is needed as substitution for the fuselage area term in equations (4.2) and (4.4). Finally, the aspect ratio is expressed in equation (4.4) as a function of span lengths and planar areas.

$$A_{wing} = 0.5 \left(c_{root} + c_{tip} \right) b_{fus} \tag{4.1}$$

$$A_{fus} + A_{wing} = 0.5 \left(c_{root,0} + c_{tip} \right) \left(b_{fus} + b_{wing} \right) \tag{4.2}$$

$$A_{fus} = 0.5 \left(c_{root,0} + c_{tip} \right) b_{fus} = 0.5 \left(\frac{c_{tip}}{\lambda} + c_{root} \right) b_{fus} \tag{4.3}$$

$$AR = \frac{\left(2(b_{fus} + b_{wing}) \right)^2}{2A_{wing}} = \frac{2(b_{fus} + b_{wing})^2}{A_{fus} + A_{wing}} \tag{4.4}$$

After substitutions for $c_{root,0}$ and A_{fus} in equations (4.2) and (4.4), the equations can be rearranged to have one side of the equation equal to zero, such that the system of simultaneous equations can be solved for the unknowns using a root-finding method. An iterative nonlinear Newton-Raphson approach has been used in the outlined method to find the solution to the system of equations composed of equations (4.5) through (4.7).

$$0.5 \left(c_{root,0} + c_{tip} \right) b_{fus} - A_{wing} = 0 \tag{4.5}$$

$$0.5 \left(\frac{c_{tip}}{\lambda} + c_{root} \right) b_{fus} + A_{wing} - 0.5 \left(\frac{c_{tip}}{\lambda} + c_{root} \right) \left(b_{fus} + b_{wing} \right)^2 = 0 \tag{4.6}$$

$$AR \cdot 0.5 \left[\left(\frac{c_{tip}}{\lambda} + c_{root} \right) b_{fus} + A_{wing} \right] - 2 \left(b_{fus} + b_{wing} \right)^2 = 0 \tag{4.7}$$

Quarter-chord sweep angle ($\lambda c/4$) is an additional parameter included in this study. Once a wing has dimensions corresponding to the root and tip chords as well as the span, the sweep angle serves to position the tip section relative to the root section in the X-Z plane.

Other than planform parameters, twist angle is a design variable of interest. Linear geometric twist (θ) is used, such that the twist angle is the angle by which the root section is twisted about the quarter-chord, increasing the local incidence of the root-most section by the twist value. The added local incidence decreases linearly in the direction of the tip of the wing until it reaches zero at the wing tip. This orientation for the twist angle, in contrast to the alternative where root-most incidence is negative, is chosen to encourage more favourable stall conditions by allowing the inboard part of the wing to stall before the outboard part, preserving roll control.

4.2 Optimization Bounds

The optimization bounds for parameters x_1, x_2, x_3, and x_4 are listed in Table 4.1.

The range for $\Lambda_{c/4}$ allows some flexibility without drastically modifying the stability characteristics of the aircraft. The range for θ is meant to improve stall performance, but not at the expense of an excessively limited operating envelope. Increases in aspect ratio are accompanied by increases in span, which in turn inevitably increase the structural weight of the wing; it is therefore allowed to vary marginally so long as its impact is captured. Finally, the taper ratio

Table 4.1   Bounds for the global wing optimization

Variable	Parameter	Original Value	Lower Bound	Upper Bound
x_1	$\Lambda_{c/4}(°)$	4.8	0	9.6
x_2	$\theta(°)$	0.0	0	4
x_3	AR (constant-area)	10.14	8.5	12
x_4	λ (constant-area)	0.512	0.3	0.7

is allowed sufficient leeway from the original value to allow the design to achieve an optimal lift distribution.

4.3   Training Set

To build a GPR model, a training set size of $15N$ was observed to adequately model the response of test functions which included univariate, Ackley's, Beale's, Hölder table, and McCormick's functions. For the four-variate problem at hand, 60 samples were therefore deemed a suitable starting point for building a training set. Latin hypercube sampling is used to generate a near-random set of samples with an even spread throughout the defined search space. The 60 samples drawn are listed in Appendix I, and the resulting set of geometries is shown in Figure 4.1.

The training set is constructed for wings at an angle of attack of $2°$. As observed in Figure 3.13, $(C_L/C_D)_{max}$ occurs in the neighbourhood of $2°$, allowing the optimization process to act as a means of manipulating this key parameter. The wings in the training set are tested at a flow speed of 25.4 m/s at MSL, which corresponds to a chord-based Reynolds number of 1.0×10^6.

4.4   Objective Functions

As discussed in § 1.4.3, the objective function to optimize range differs from that to optimize endurance. The range and endurance of the aircraft can be maximized by maximizing C_L/C_D
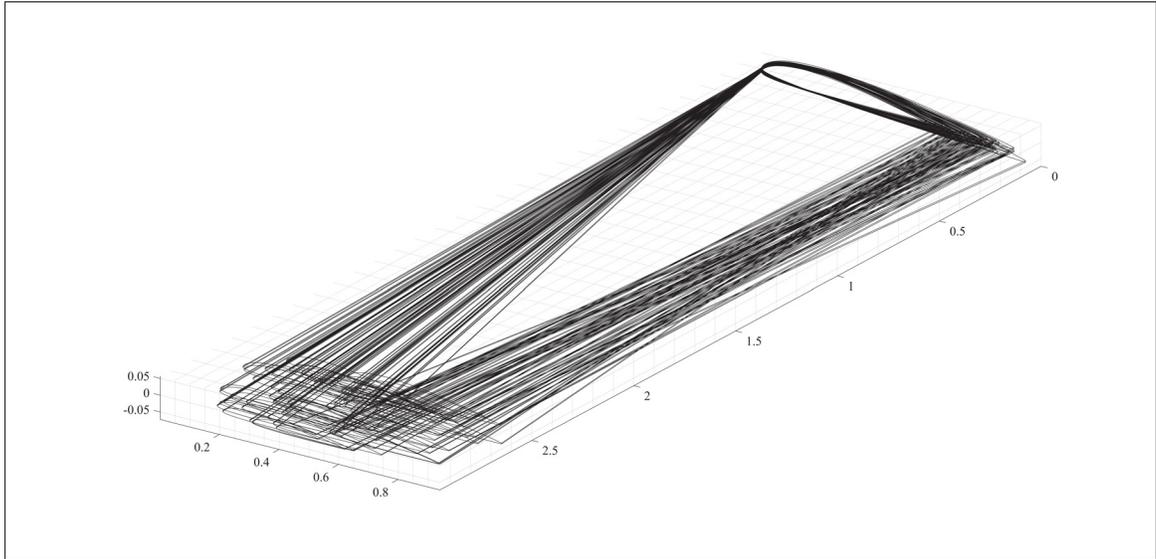
Figure 4.1   Wing optimization training set geometries

and $C_L^{3/2}/C_D$, respectively. These two parameters thus have individual response surfaces which are treated separately.

4.5   CFD Implementation

A mesh is generated for each wing geometry produced using a series of commands written in Tcl/Tk, which stands for Tool Command Language/Toolkit, for use with ICEM CFD. This automated meshing procedure ensures that the same high-quality hexahedral grid used in Chapter 3 is obtained for all test wings in the training set. The transition SST model is used as turbulence model, with curvature correction, and turbulence kinetic energy production limiter and production Kato-Launder enabled in ANSYS Fluent. A coupled pressure-velocity scheme is used with second-order schemes for the pressure, momentum, k, ω, γ, and Re_θ. A second-order implicit time discretization is used with the default Courant number of 200 which controls the pseudo-time term (ANSYS Inc., 2006).

4.6   Kernel Selection and Model Validation

The kernels given mathematically in § 2.2.2 are used to construct GPR models for the range and endurance objectives. The leave-one-out validation results for the models are then compared so that the best kernel can be selected for use in the optimization routine.

4.6.1   Regression model for range optimization

The range objective function is $f = C_L/C_D$, for which GPR model responses are plotted alongside the true responses in Figure 4.2. An error bar representing one standard deviation obtained in the Kriging process is plotted for each prediction. The associated percent errors on the predicted values relative to the true values are plotted in Figure 4.3. It is seen in Figure 4.2 that all four kernels produce reasonable predictions, indicating that hyperparameters have been optimized successfully for the GP.
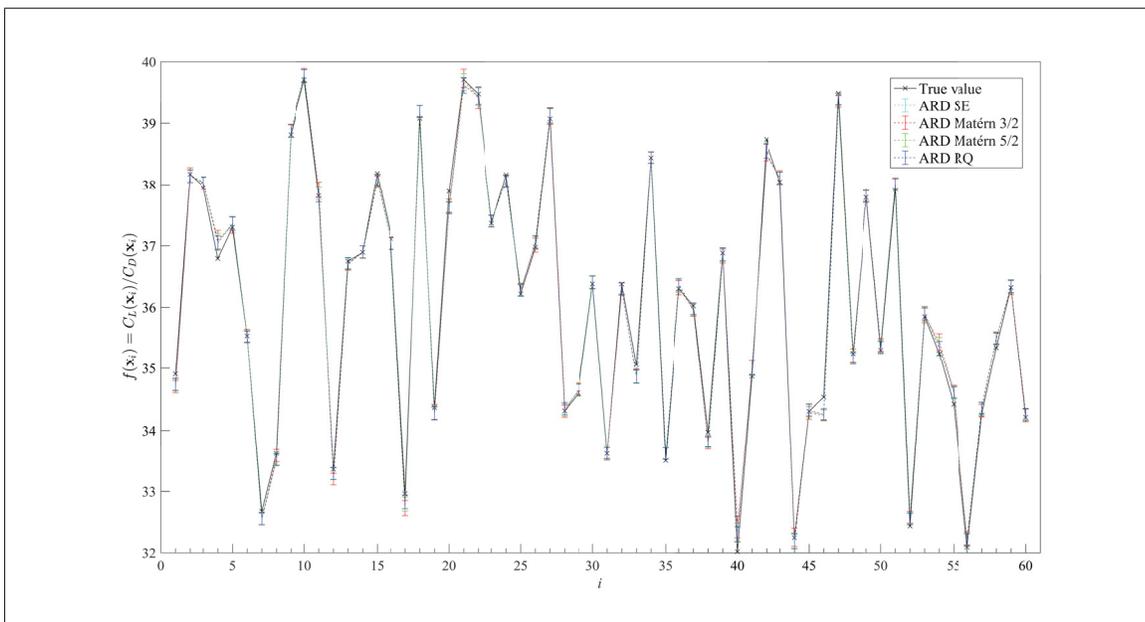
Figure 4.2   Predicted responses for C_L/C_D
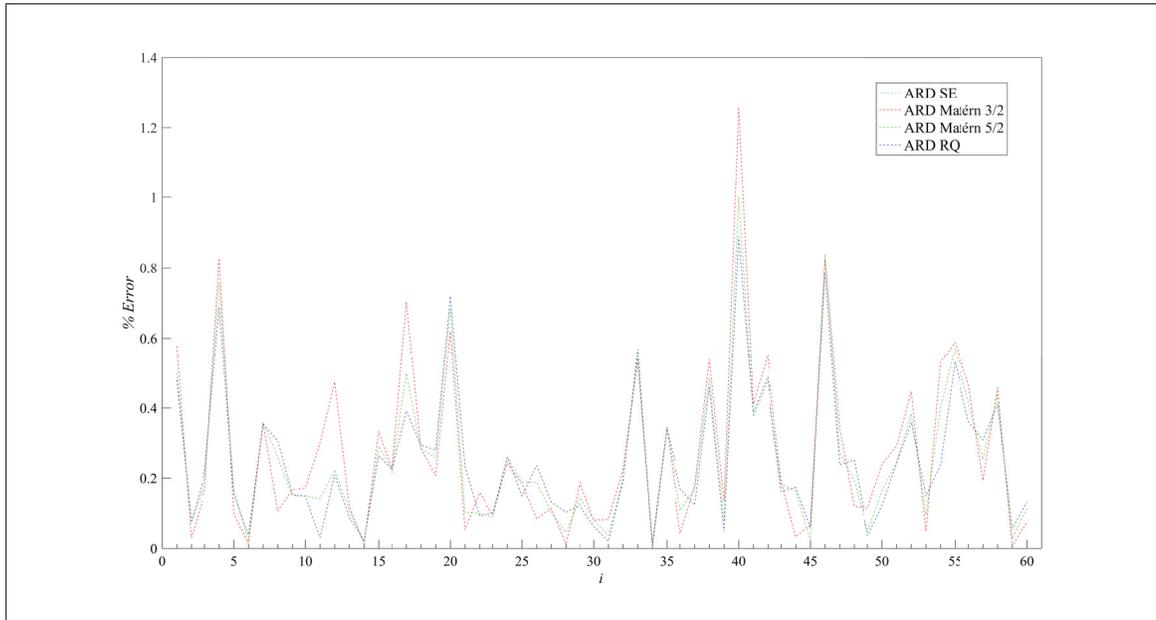
Figure 4.3   Percent errors on the predicted responses for C_L/C_D

The optimized hyperparameter values obtained are listed in Table 4.2. Table 4.3 shows results for the performance metrics used to compare the accuracy of tuned kernels, namely the *MSE* and the maximum percent error over all samples in the training set.

Table 4.2   Hyperparameters for C_L/C_D kernels

θ	ARD SE	ARD Matérn 3/2	ARD Matérn 5/2	ARD RQ
λ_1	201.0	1323	410.9	200.9
λ_2	5.666	44.20	13.07	5.666
λ_3	9.595	72.20	21.42	9.595
λ_4	1.638	10.76	3.479	1.638
σ_n	0.08663	0.07619	0.08490	0.08663
σ_f	7.742	29.33	13.29	7.742
α_{RQ}	–	–	–	7.646×10^5

Table 4.3 Performance metrics of the C_L/C_D kernels

	ARD SE	ARD Matérn 3/2	ARD Matérn 5/2	ARD RQ
MSE	0.01242	0.01635	0.01346	0.01242
max(*%Error*)	0.8886	1.258	1.002	0.8886

The tuned ARD SE and ARD RQ covariance functions are nearly identical. They are both smooth and infinitely differentiable. An RQ kernel is obtained by summing several SE kernels with different length scales. The large value of α_{RQ} causes the ARD RQ kernel to behave like an ARD SE kernel, because the RQ kernel becomes identical to the SE kernel as α_{RQ} tends to infinity. Length scales describe the relevance of parameters. The large value of the first length scale, λ_1, indicates that $\Lambda_{c/4}$ has the least impact on f. The next two length scales, λ_2 and λ_3, show that θ and AR are high-impact parameters. While the last length scale, λ_4, corresponding to λ on the wing, is small, it remains a parameter of moderate impact because λ_4 is large relative to the range of λ.

Considering individual samples, the highest level of error occurs at the 40th sample, for which the value of f is the lowest in the set. The next highest level of error is at the 46th sample, for which the value of f is the highest in the set. These results exemplify a behaviour typical of GPR models: highs are underpredicted, and lows are overpredicted. Over the complete training set, the ARD SE and nearly identical ARD RQ kernels perform best with the lowest *MSE* and maximum percent error. The ARD RQ kernel is thus selected to optimize the range.

4.6.2 Regression model for endurance optimization

Similarly, the responses of GPR models are plotted in Figure 4.4, with the corresponding percent error plots shown in Figure 4.5.

Figure 4.4 shows that GPR models constructed using each of the four kernels under test is capable of closely predicting $C_L^{3/2}/C_D$ values with properly optimized hyperparameters, which
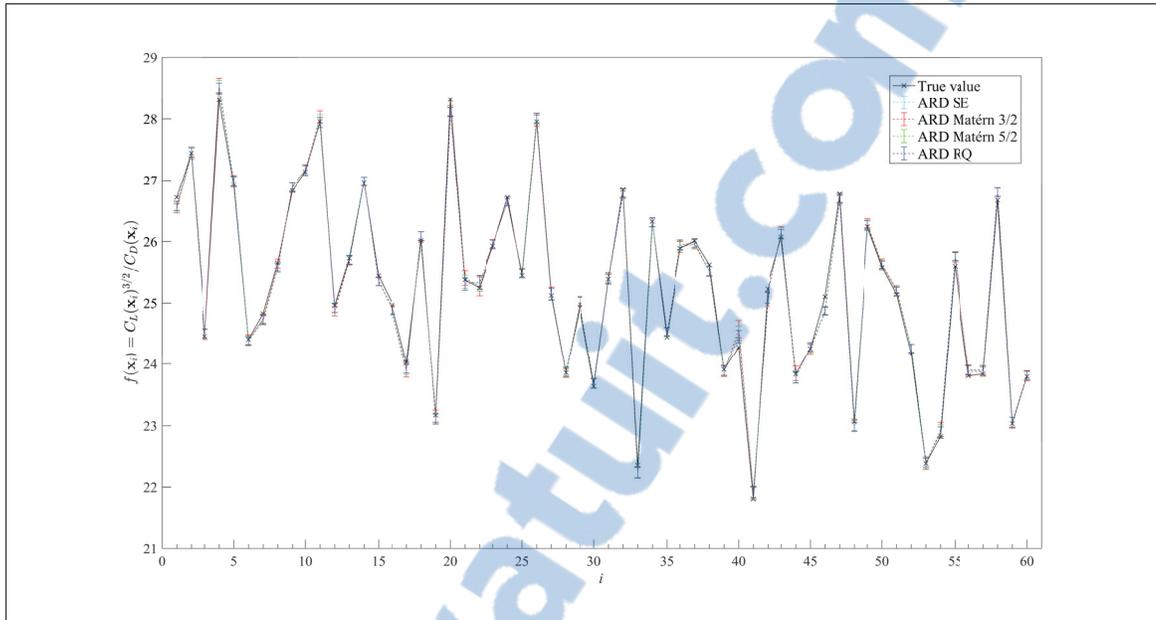
Figure 4.4   Predicted responses for $C_L^{3/2}/C_D$
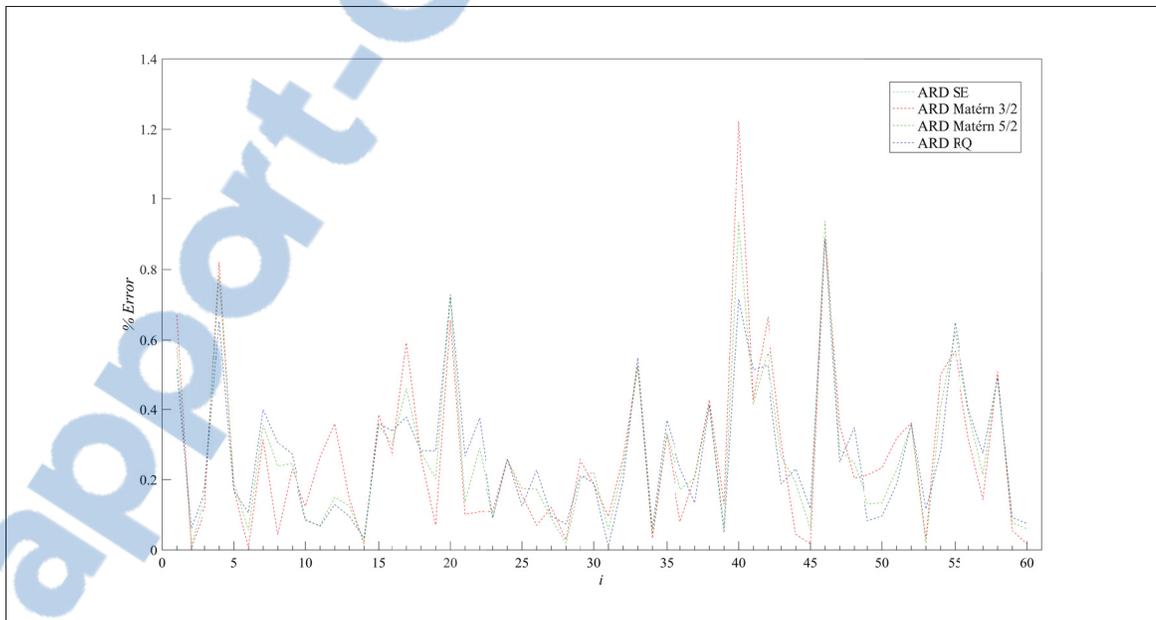
Figure 4.5   Percent errors on the predicted responses for $C_L^{3/2}/C_D$

are listed in Table 4.4. The performance metrics of each of the kernels are presented in Table 4.5.

Table 4.4 Hyperparameters for $C_L^{3/2}/C_D$ kernels

θ	ARD SE	ARD Matérn 3/2	ARD Matérn 5/2	ARD RQ
λ_1	147.2	708.4	257.6	147.2
λ_2	5.879	39.49	12.86	5.879
λ_3	8.838	61.66	19.31	8.838
λ_4	1.633	10.37	3.435	1.633
σ_n	0.06608	0.05378	0.06349	0.06608
σ_f	6.272	20.97	10.19	6.272
α_{RQ}	–	–	–	7.757×10^5

Table 4.5 Performance metrics of the $C_L^{3/2}/C_D$ kernels

	ARD SE	ARD Matérn 3/2	ARD Matérn 5/2	ARD RQ
MSE	0.007188	0.008660	0.007688	0.007188
$\max(\%Error)$	0.8872	1.223	0.9358	0.8872

In the same way as for the C_L/C_D kernels, the large value of α_{RQ} causes the ARD RQ kernel to behave like an ARD SE kernel again. The length scales are marginally smaller for the $C_L^{3/2}/C_D$ models relative to those for the C_L/C_D model. This finding can be attributed to the fact that values for $C_L 3/2/C_D$ are smaller than values for C_L/C_D with values for C_L below unity. It can thus be surmised that the sensitivity of $C_L^{3/2}/C_D$ to the four design parameters echoes that of C_L/C_D.

Considering the individual performance of each kernel, the ARD RQ kernel is chosen to model the $C_L^{3/2}/C_D$ response surface. The superior performance of the smoother ARD SE and ARD RQ kernels indicates smoothness in $C_L^{3/2}/C_D$, as is observed in C_L/C_D.

4.7 Optimizer Settings

An optimization routine is shown as part of the delineation of the research methodology shown in Figure 2.4. However, the number of iterations or samples evaluated per iteration is not specified as such settings are highly problem-dependent and cannot be generalized. The values used in this wing optimization series are shown in Table 4.6. In the expected improvement algorithm, $\mathbb{E}[I(\mathbf{x})]$ is evaluated at successive collections of points to search for the global optimum. At every iteration in the optimization loop, the GPR model is used to predict values for samples in a Latin hypercube. Latin hypercube sampling ensures that values are randomly selected from all regions of the design space. The number of samples for each iteration needs to be strategically chosen in conjunction with the number of iterations to explore the search space sufficiently and efficiently. Computational cost grows exponentially with the number of samples per iteration, as the inversion of large matrices is required. It is therefore more efficient to have fewer samples per iterations with a large number of iterations than the reverse. The acceptable deviation from the true value, or tolerance, and the optimization budget are the stopping criteria in the algorithm. The optimization budget refers to the number of additional high-fidelity evaluations allowed to update the model if the predicted and true values of f do not agree within the specified tolerance.

Table 4.6 Parameters for the wing
optimization algorithm

Setting	Value
Number of samples per iteration	500
Number of iterations	2000
Tolerance (%)	0.5
Optimization budget	4

4.8 Results

Four optimizations results are sought using the training data and GPR models built using the expected improvement algorithm. Optimizations 1 and 2 are performed for range and endurance for aspect ratio values constrained to the original value of 10.14, while Optimizations 3 and 4 are performed for range and endurance with no constraint on the aspect ratio. The first two optimizations endeavour to improve the wing aerodynamics without a change in AR, which expressly prevents the reduction in induced drag owing to an increase in AR from dominating in the results so that the influence of other design parameters can be studied equally.

Progress plots are shown in Figure 4.6 for the constrained-AR optimizations and in Figure 4.7 for the unconstrained-AR optimizations. The original values, which are constant, are represented by the upper line, while the current best value at each iteration is represented by the dashed line. The four optimizations produced results in agreement with the true values within the specified tolerance in a single optimization cycle, as is seen with the number of iterations capped at 2000. If the tolerance was not met in a cycle, a second optimization cycle would continue iterating to 4000 using a GPR model updated with the CFD solution calculated at iteration 2000. Values for the minimum cost attained and percent improvement achieved are presented in Table 4.7, and the wing parameters corresponding to those optima are shown listed in Table 4.8.

Table 4.7   Minimized costs and percent improvements of optimizations

Optimization	Minimized cost	% Improvement
(1) Original AR, $-C_L/C_D$	-38.11	0.8915
(2) Original AR, $-C_L^{3/2}/C_D$	-26.28	9.297
(3) Unconstrained AR, $-C_L/C_D$	-40.56	7.369
(4) Unconstrained AR, $-C_L^{3/2}/C_D$	-28.68	19.27
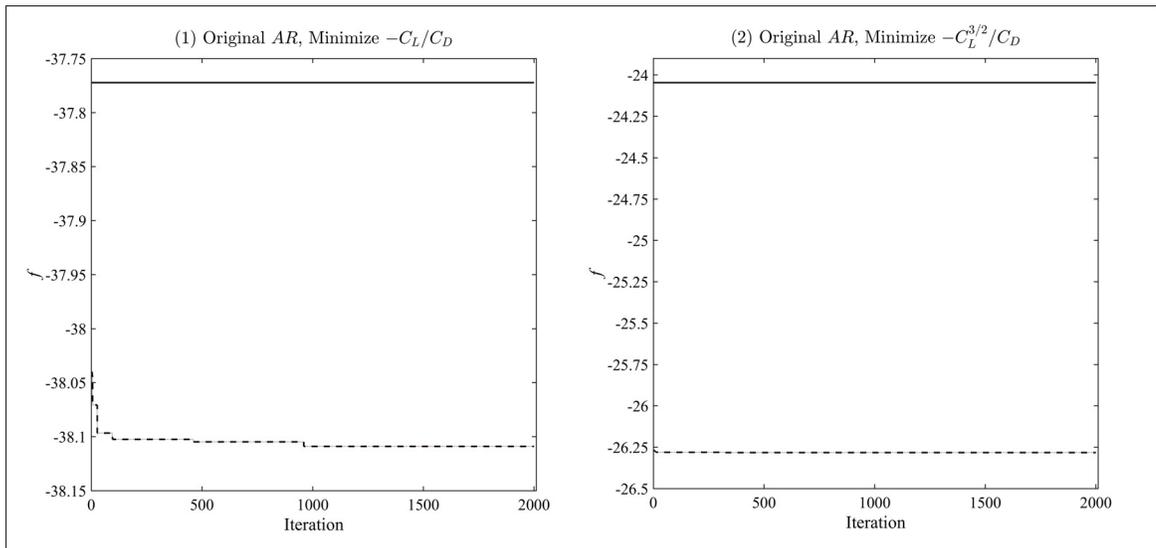
Figure 4.6   Progress plots for constrained-*AR* optimizations
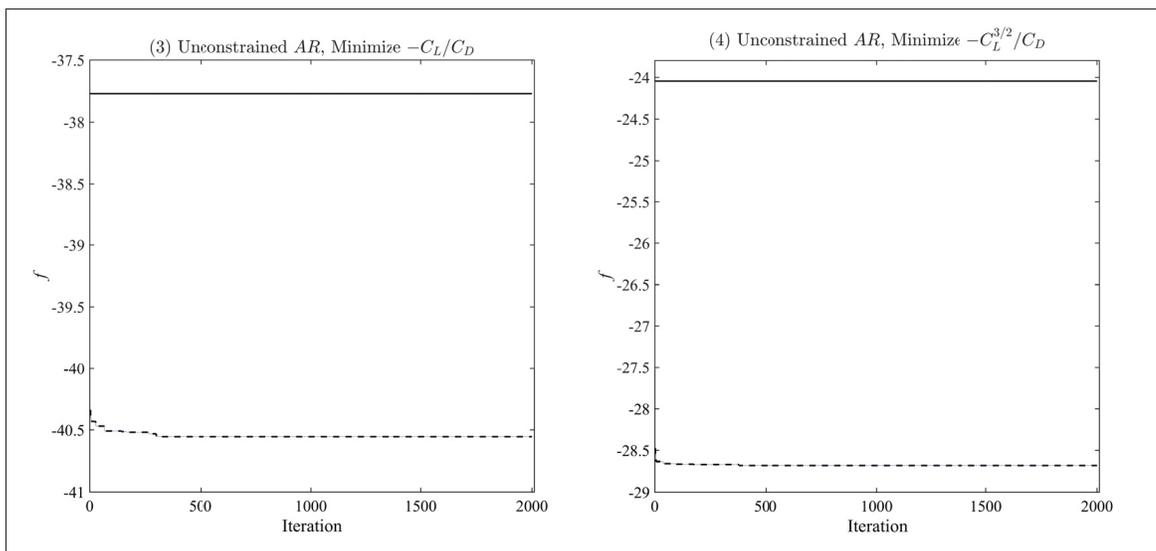
Figure 4.7   Progress plots for unconstrained-*AR* optimizations

Optimization 1 shows that only a very modest improvement can be obtained at fixed *AR* on the original C_L/C_D value. The avenues for increasing C_L/C_D are to bring on either an increase in C_L or a decrease in C_D, or both. The results show that twist is not favoured in this optimization, leaving only planform parameters $\Lambda_{c/4}$ and λ to improve the aerodynamics of the wing. For a constant-area wing with a predefined airfoil section at fixed *AR* in subsonic incompressible

Table 4.8   Wing parameters for range and endurance optimizations

Optimization	$\Lambda_{c/4}(°)$	$\theta(°)$	AR	λ
(1) Original AR, $-C_L/C_D$	9.486	0.001824	10.14	0.3003
(2) Original AR, $-C_L^{3/2}/C_D$	9.342	3.660	10.14	0.6911
(3) Unconstrained AR, $-C_L/C_D$	8.605	0.05861	12.00	0.3096
(4) Unconstrained AR, $-C_L^{3/2}/C_D$	9.574	3.746	11.99	0.5323

flow, no design lever exists among planform parameters to meaningfully increase the lift com-ponent. However, the lift distribution along the span of the wing can be tailored to become closer to an elliptical distribution, thereby reducing its induced drag. The modification in λ contributes largely to this change, as does the change in $\Lambda_{c/4}$, but to a lesser extent because of its larger length scale.

Optimization 2 shows that $C_L^{3/2}/C_D$ can be significantly increased at the conditions for which the optimization is performed, primarily by taking advantage of the influence of θ. This result cannot be fully understood on its own and warrants a deeper investigation of the performance of this optimized wing. Additional CFD simulations are conducted at angles of attack between $0°$ and $14°$ at $2°$ intervals so that the optimized wing can be compared against the original wing. The resulting lift and drag curves are shown in Figures 4.8 and 4.9, respectively. These curves show that greater lift and drag coefficients are obtained for the optimized wing relative to the original, baseline wing, as is to be expected for a positively twisted wing. Overall, wing twist serves to shift the lift and drag curves to yield higher C_L and C_D values relative to the untwisted wing for the same α. In doing so, wing stall is brought about earlier on the twisted wing, al-though it occurs root-first as desired. The lift-curve slope for the twisted wing is inferior to that of the original wing, signaling a reduction in efficiency which is attributable to increased local flow separation on higher-incidence sections near the wing root. The evolution of C_L/C_D and $C_L^{3/2}/C_D$ with α are shown in Figures 4.10 and 4.11, respectively, for the baseline, untwisted wing and for the optimized, twisted wing. The C_L/C_D and $C_L^{3/2}/C_D$ curves for the twisted wing are, for the most part, translations of those for the untwisted wing. For values of α below $3.3°$,

$C_L^{3/2}/C_D$ is effectively increased for the optimized wing, as seen in Figure 4.11. However, the corresponding C_L/C_D values are significantly reduced for values of α exceeding $1.24°$ in the optimized wing relative to the baseline wing, as seen in Figure 4.10.
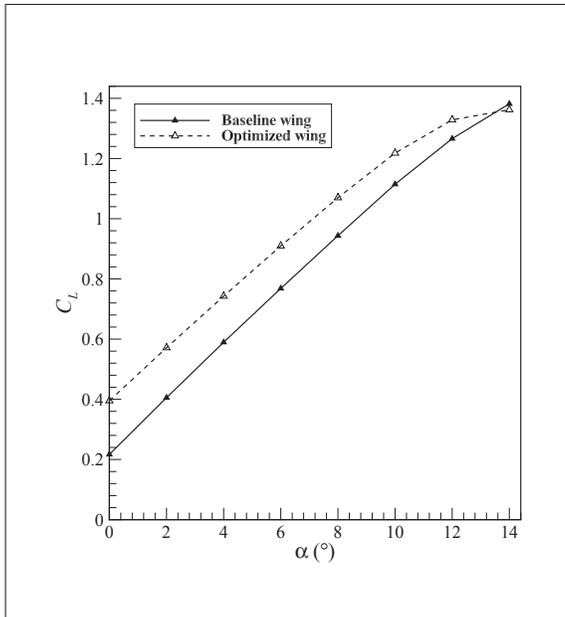
Figure 4.8   Lift curves for the original and optimized wings
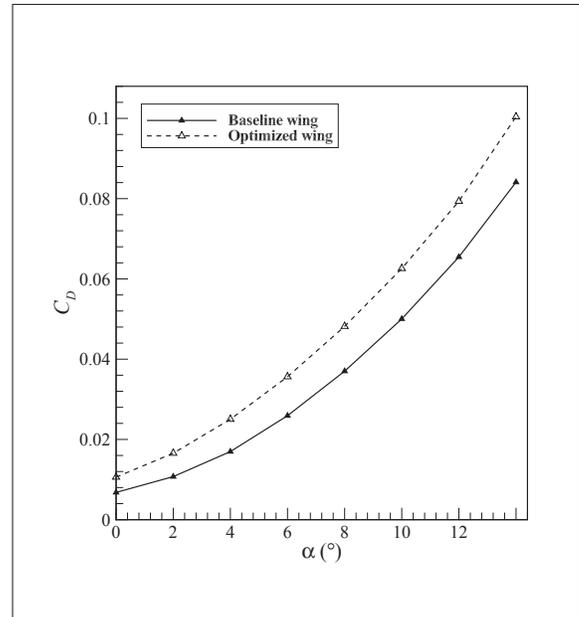
Figure 4.9   Drag curves for the original and optimized wings

Optimization 3 results show that if the AR is unconstrained, and thus free to vary, the parameters associated with optimized range inevitably tend towards the upper limit of the AR which was set at 12. As in Optimization 1, twisting the wing is not favoured in the optimization of C_L/C_D, while a lower taper ratio compared to the original taper ratio is favoured. At the maximum AR, significant improvement is obtained from the optimization algorithm with a 7.37 % increase in C_L/C_D at α of $2°$.

Optimization 4 shows that the maximum AR is again obtained for its associated reduction in induced drag. Greater twist is encouraged relative to Optimization 2. The results show that increases in $\Lambda_{c/4}$, θ, AR, and λ can produce a 19.3 % improvement on $C_L^{3/2}/C_D$. However, the differences between the results from Optimizations 3 and 4 resemble the differences between those from Optimizations 1 and 2, bearing in mind that the Optimization 1 results do not deviate
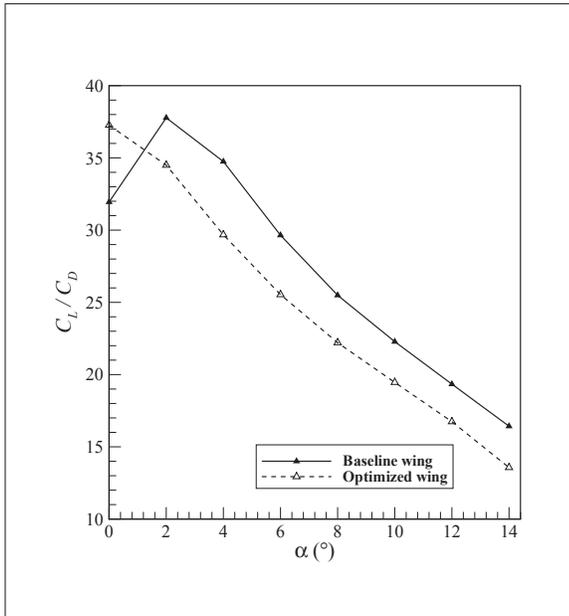
Figure 4.10 C_L/C_D curves for the original and optimized wings
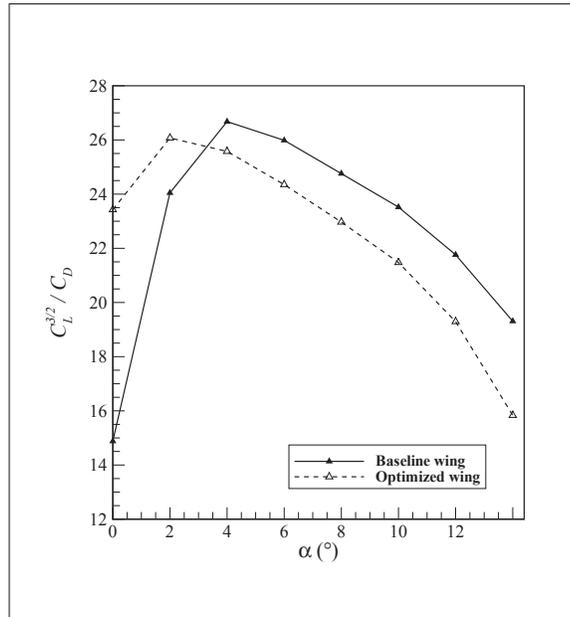
Figure 4.11 $C_L^{3/2}/C_D$ curves for the original and optimized wings

much from the original wing. Earlier stall, reduced lift-curve slope, reduced $(C_L/C_D)_{max}$ and $(C_L^{3/2}/C_D)_{max}$ are to be expected in the twisted wings obtained in Optimizations 2 and 4.

4.9 Conclusions

From the series of optimizations performed, it is evident that very limited improvement can be obtained when the span or aspect ratio of the wing is not allowed to increase. Induced drag can be minimized by favouring greater ellipticity in the lift distribution of the wing. Viscous drag can be near its minimum in this flow regime by avoiding large local chord lengths that cause the Reynolds number to be higher locally and a greater portion of the flow to be turbulent. Wing twist is observed to be a parameter useful in fine-tuning the angle of attack at which it would be most beneficial for $(C_L/C_D)_{max}$ or $(C_L^{3/2}/C_D)_{max}$ to be positioned; this condition corresponds to flight conditions at surveillance. Multi-objective treatment is required to obtain the best compromise between optimized range and optimized endurance.

Using a fixed value for real wing area proved to be a circumspect way of confining wing loading to the same acceptable limits as for the original wing while reducing the optimization problem by one variable. If the winglet studied in Chapter 3 is affixed to the wing tip, an interaction is to be expected between the taper ratio and winglet efficiency because greater outboard loading increases the benefits obtained using the winglet.

When the aspect ratio is free to vary, its optimized value (as seen in Optimization 3 and 4 results) is at its upper limit, set at 12 in the problem definition. This corresponds to a half-span of 3 m, and, compared to the original half-span of 2.77 m, represents an increase of 8.3 % in the span over the original value. Such an increase in wing span is inevitably structurally costly, which justifies the need for Optimizations 1 and 2 at fixed aspect ratio of 10.14.

The use of GPR models and the expected improvement algorithm was seen to be economically advantageous for the four-variate problem where four optimization results were sought. Additionally, the use of automatic relevance determination kernels allowed the sensitivity of the variables through their respective length scales. It was observed that wing sweep has the least impact, followed by the taper ratio. The aspect ratio and twist angle demonstrated the most influence on both the range and the endurance objectives.

Finally, because a type of wing morphing is addressed in the next chapter, the results can be further interpreted since they indirectly point to what improvements could be expected of a wing capable of variable twist. Such designs exist and were covered in § 1.5. A variable-twist wing would be capable of adjusting $(C_L/C_D)_{max}$ or $(C_L^{3/2}/C_D)_{max}$ values to the current flight condition, thus controlling the range and endurance trade-off significantly.

CHAPTER 5

MORPHING WING AERODYNAMIC OPTIMIZATION

Morphing technologies for aircraft have become of great interest to aircraft designers, particularly with the advent of increasingly sophisticated control architectures. To continue on the research efforts at the LARCASE to advance morphing technology, the previously tested concept of using actuators underneath a flexible composite skin to achieve pointwise deformations (Koreanschi *et al.*, 2017) is extended. The proposed morphing approach is presented and studied in this chapter.

5.1 Morphing Approach

In the proposed morphing concept, an actuated rod is made to rotate to produce a displacement under the flexible skin of the wing as shown in Figure 5.1. The cross-section of the rod is shown as an ellipse with semiminor axis r_0 and semimajor axis $r_0 + \delta_{max}$, where r_0 corresponds to the unaltered surface to which a deformation of amplitude δ can be applied. For the point of contact between the wing surface and the rod to remain unchanged as the rod is rotated, the axis of rotation needs to be positioned at a slight, determinable, offset from the geometrical centreline of the rod. While the implementation illustrated in Figure 5.1 is meant to be conceptually easier to grasp, there is no requirement for the actuated rod to be non-axisymmetric; a cylindrical rod can effect the same displacements when rotated about an axis offset from the axis going through its centre. To give more meaning to the design variables in connection with the morphing process, it is strategic to allow the dimensions of the cross-section of the rod to vary as the chord length, such that the displacement relative to the chord length at any spanwise location is the same. Such a definition has the useful consequence that the same morphed airfoil shape is obtained throughout most of the wing where the rod is active, the exceptions to this being at either end of the rod where deformations taper off smoothly into the undeformed airfoil shape.
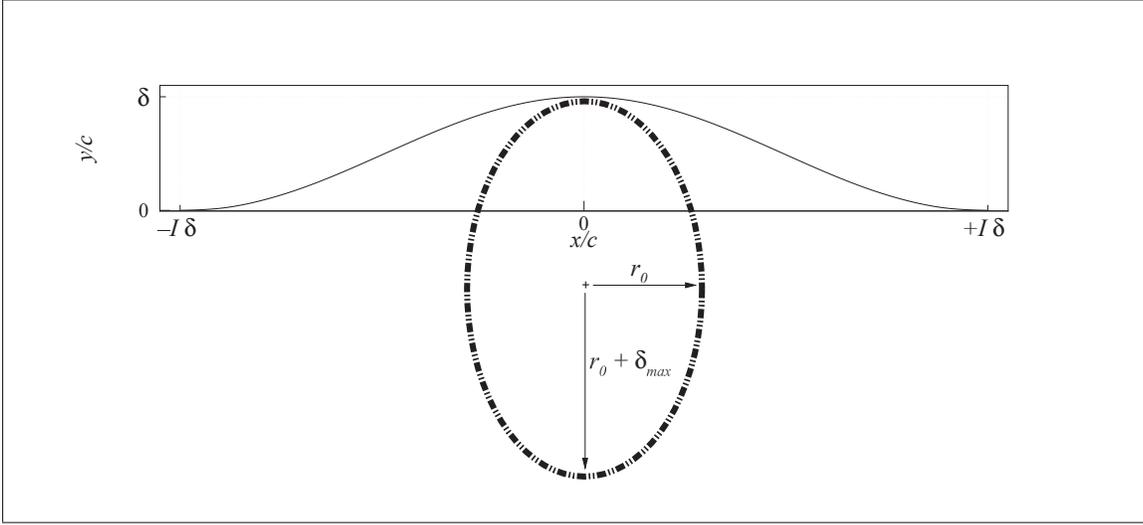
Figure 5.1   Bounds and amplitude of a morphing deformation

The deformation is assumed to produce sinusoidally-distributed displacements described by Equation (5.1). The generic formulation for the displacement in the Y-direction, δ_y, is a function of x and is centred about zero; it can be translated to the nondimensional chordwise position (x/c) chosen. The amplitude of deformation is δ. The width of deformation is taken as a function of an impact factor I. A nominal value of 20 is used for I to obtain realistic deformations. However, the actual value of I is contingent on the design of the composite skin subject to the movements of the actuated rod. The resulting deformation bounds are $-I\delta$ and $+I\delta$.

$$\delta_y(x) = \delta \left[\cos\left(\frac{x}{0.2\pi I\delta}\right) \right]^2, \quad -I\delta \leq x \leq I\delta \tag{5.1}$$

Three actuated rods, positioned at x/c values of 25 %, 37.5 % and 50 % are considered in this morphing wing study. Figure 5.2 illustrates the cross-section of the wing in the morphing region on a nondimensional scale. The rationale for choosing the positions of the actuated rods is illustrated in Figure 5.3, where it is made evident that careful consideration must be given to the presence of the flap and the aileron on each wing. The amplitude of deformation of the actuated rods are denoted by δ_1, δ_2 and δ_3, which are set to the maximum extent of deformation of 1 % of the chord length in Figure 5.2. To model overlapping displacement regions, cosine

interpolation is used between the point of deformation and point of intersection of the two displacement curves to retain smoothness. Sufficient granularity is achieved by shifting only up to 12 points in the displaced airfoil coordinates; this allows smooth splines to be produced based on the displaced points to represent the morphed wing surface.
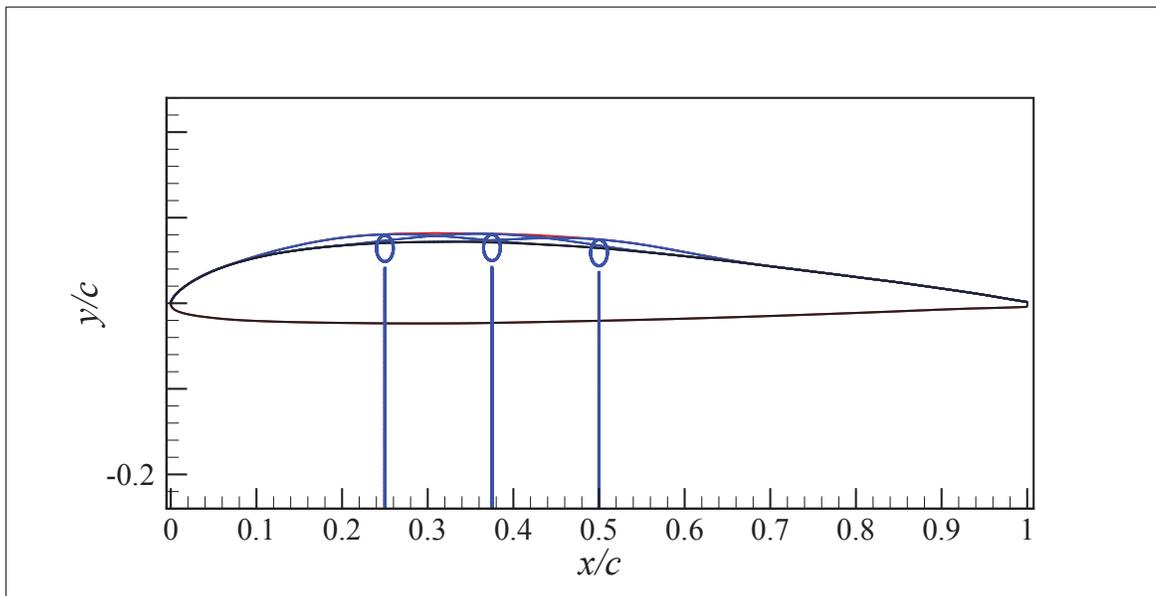
Figure 5.2   Deformation limits of the morphing wing concept
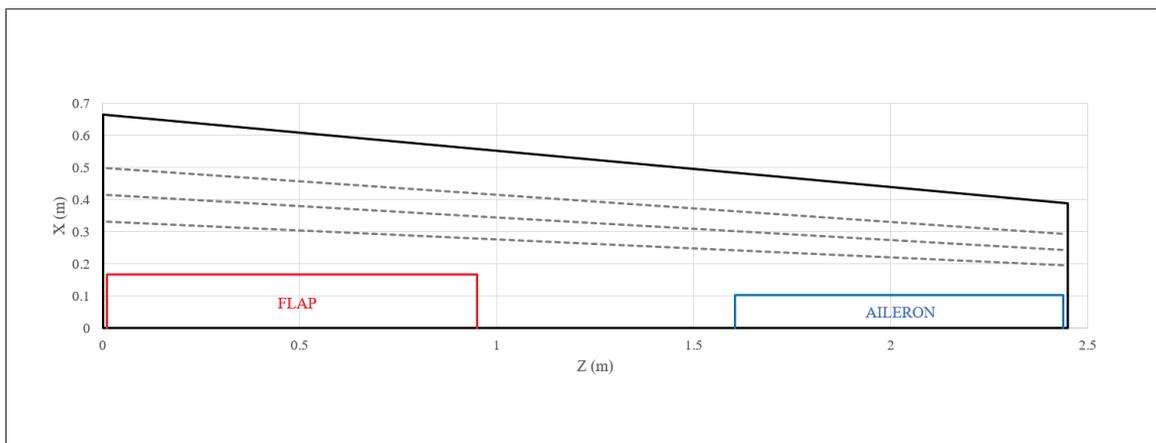
Figure 5.3   Positions of the actuated rods in the morphing wing

5.2 Optimization Bounds

As in Chapter 4, a training set needs to be built so that a surrogate model can be developed. Five variables are deemed to be relevant to this morphing wing study. Deformation amplitudes δ_1, δ_2 and δ_3, each vary between the original shape at 0 and a maximal displacement defined as being 1 % of the chord length. Because the objective of actively changing the shape of the wing in flight is to improve performance at more than one flight condition, a range of angles of attack is tested between $0°$ and $12°$ (before stall). Additionally, a range of mean sea-level (MSL) velocities (V_{MSL}) corresponding to the operational Reynolds number range of the UAV of 5.82×10^5 to 1.07×10^6 is considered. The bounds for each variable in the study are shown in Table 5.1.

Table 5.1   Training set bounds for morphing wing optimizations

Variable	Parameter	Original Value	Lower Bound	Upper Bound
x_1	δ_1	0	0	0.01
x_2	δ_2	0	0	0.01
x_3	δ_3	0	0	0.01
x_4	$\alpha(°)$	—	0	12
x_5	V_{MSL} (m/s)	—	15.4	28.3

5.3 Training Set

An initial training set size of $15N$ obtained through Latin hypercube sampling is used to model the morphing process. It is known beforehand that a validation step requires reference results for comparison. Combinations of values for angles of attack between $0°$ and $12°$ in steps of $2°$ and MSL velocities corresponding to Reynolds numbers of 0.6, 0.8 and 1.0×10^6 with $\delta_1 = \delta_2 = \delta_3 = 0$ required in the validation step are used to supplement the data set. The number of samples used to construct the surrogate model is thus the combination of 75 samples of the

morphed wing and 21 unmorphed values, totaling 96 samples. Values of the five variables for these 96 samples constituting the training set are listed in Appendix II.

5.4 Objective Functions

The objective functions are again those discussed in § 1.4.3 and used in Chapter 4. The objective for optimal range is C_L/C_D while that for optimal endurance is $C_L^{3/2}/C_D$. The two objectives are given separate treatment in the sections that follow.

5.5 CFD Implementation

A series of curves is generated using MATLAB to represent the geometry of the morphed wing, as shown in Figure 5.4. These curves are then imported into ICEM CFD where a quilted surface of the morphed wing is produced as shown in Figure 5.5.

A mesh is generated for each morphed wing geometry using a series of commands written in Tcl/Tk. Such an automated process ensures uniformity in the high-quality hexahedral grids obtained between test wings. The turbulence model used is the transition SST model with curvature correction, and turbulence kinetic energy production limiter and production Kato-Launder enabled in ANSYS Fluent. A coupled pressure-velocity scheme is used with second-order schemes for the pressure and momentum. A third-order monotonic upwind scheme for conservation laws (MUSCL) scheme is used for the turbulence model variables, k, ω, γ, and Re_θ to achieve the highest possible accuracy in the determination of transition location and boundary layer modeling with the CFD solver. A second-order implicit time discretization is used with the default Courant number of 200.

The blocking used in ICEM CFD around the morphing wing in ICEM CFD is shown in Figure 5.6. The resulting mesh is as shown in Figures 2.1 and 2.2, and the boundary conditions discussed in § 2.1.7 are enforced.
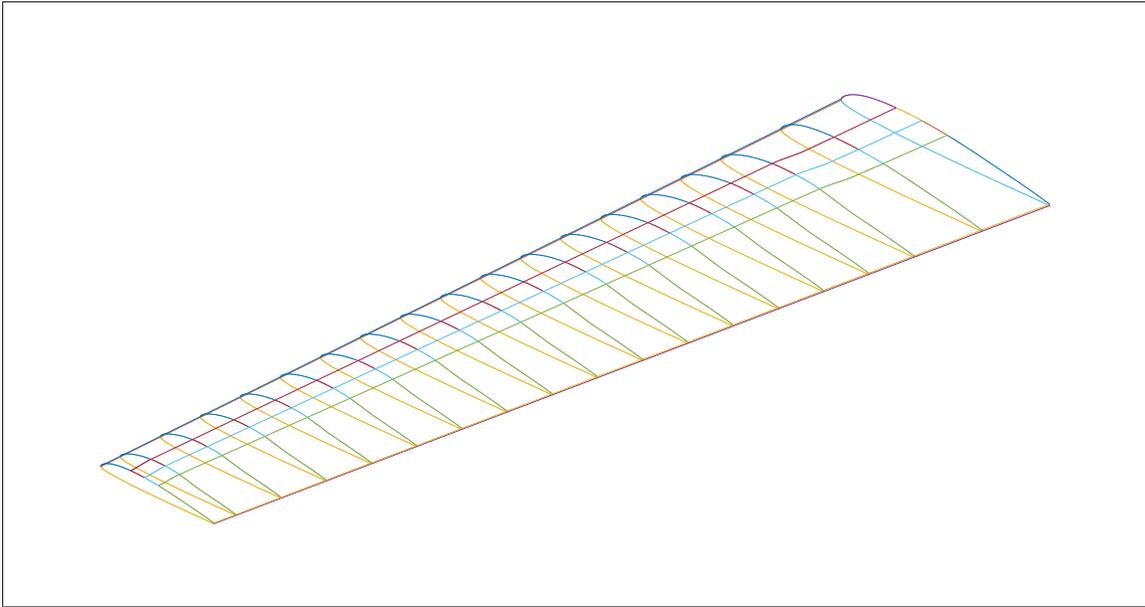
Figure 5.4   Creation of curves to represent a morphed wing

5.6   Kernel Selection and Model Validation

The ARD kernels presented in § 2.2.2 are used to construct GPR models for the range and endurance objectives. Leave-one-out validation is used to evaluate the performance of the models to determine which model performs best.

5.6.1   Regression model for range optimization

Predicted responses for the objective function $f = C_L/C_D$ are considered based on each of the four kernels under test. Responses with their corresponding error bars of one standard deviation are plotted in Figure 5.7 together with the true responses for the 96 values in the data set. It is observed that the four models are capable of closely predicting values for C_L/C_D. The associated percent errors are plotted in Figure 5.8.

The corresponding optimized hyperparameter values are listed in Table 5.2. The influence of the amplitudes of displacements is seen through their length scales, λ_1, λ_2 and λ_3. The four GPR models unanimously demonstrate that $\lambda_1 < \lambda_2 < \lambda_3$, such that δ_1 is the most influential
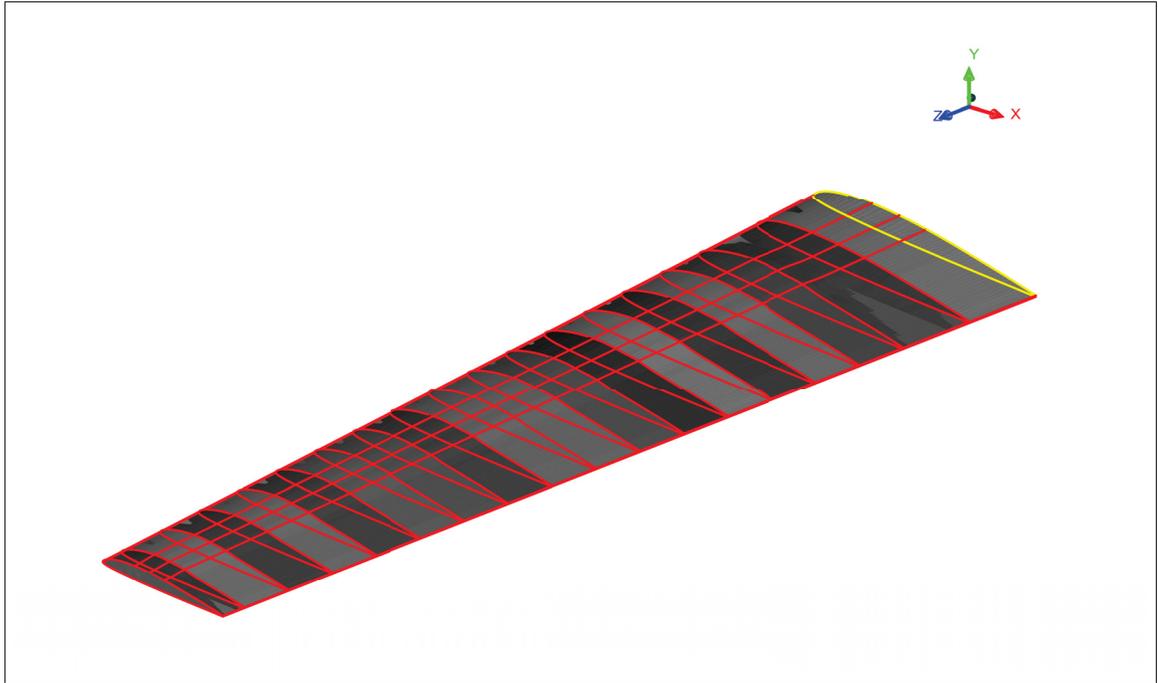
Figure 5.5   Quilted surface of a morphed wing
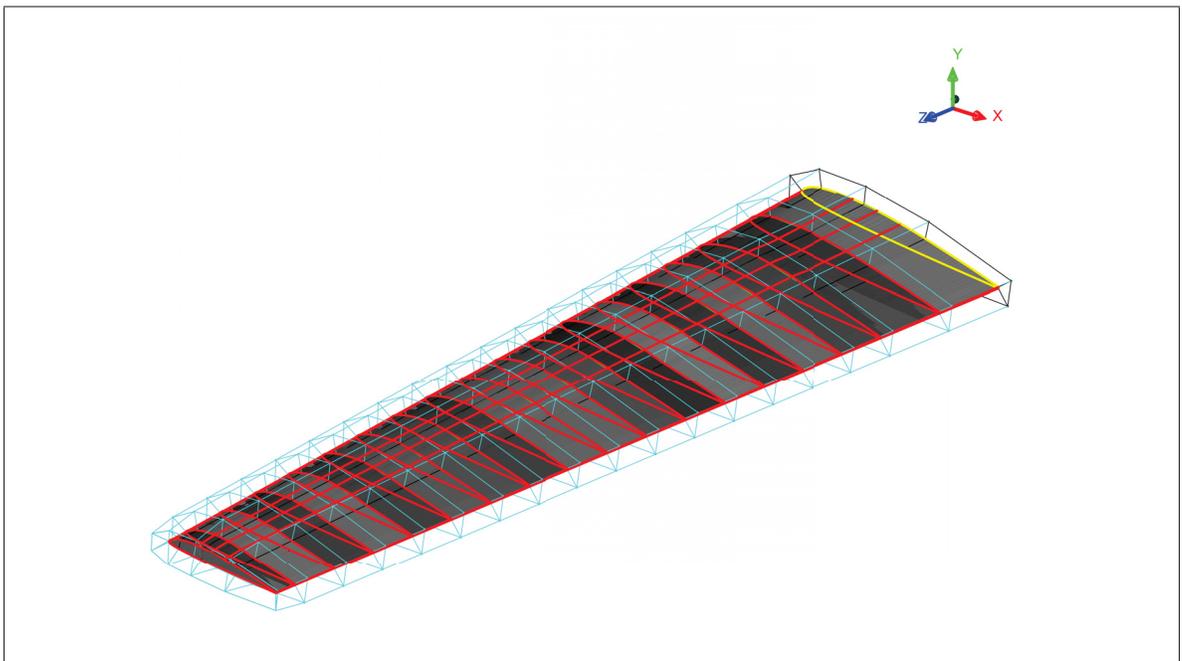
Figure 5.6   Blocking around a morphing wing
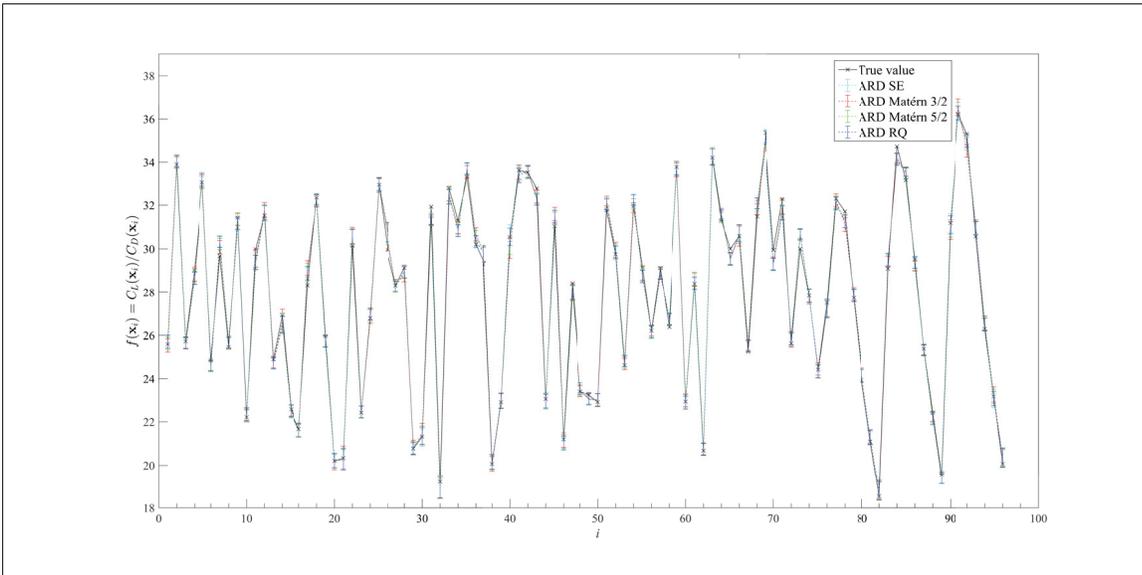
Figure 5.7   Predicted responses for C_L/C_D
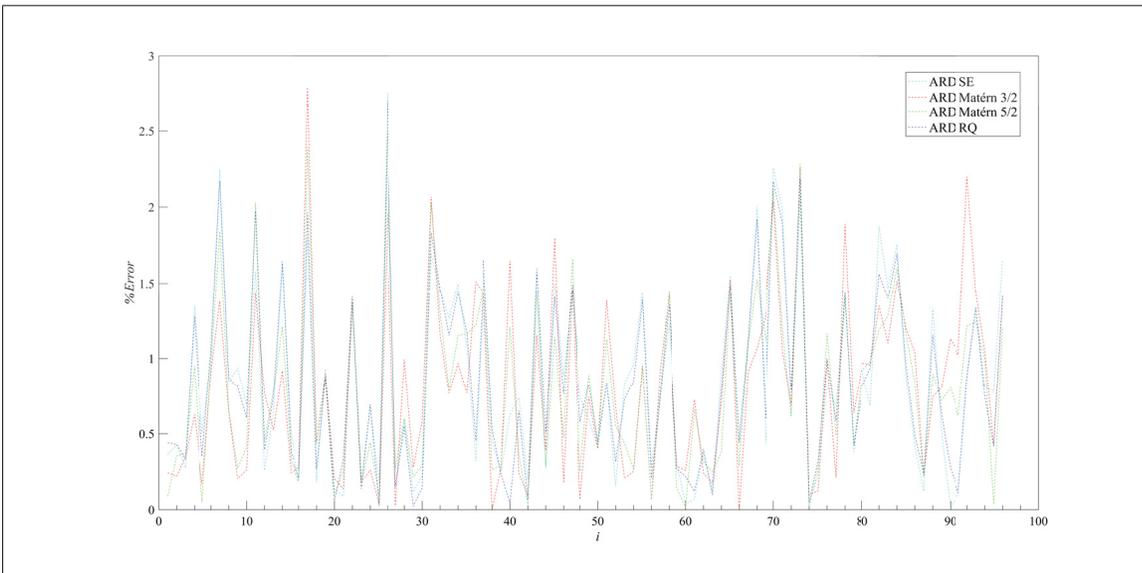
Figure 5.8   Percent errors on the predicted responses for C_L/C_D

morphing parameter while δ_3 is the least influential morphing parameter. The MSL velocity length scale (λ_4) is observed to be large, indicating low to moderate influence on f.

Values for *MSE* and maximum percent error for each kernel are shown in Table 5.3. The percent errors on the predicted values are seen to differ largely among the tuned kernels. The

ARD Matérn kernel with 5/2 degrees of freedom shows the best performance with the lowest MSE and the lowest maximum percent error. This value of ν means that the ARD Matérn 5/2 kernel is twice-differentiable, compared to the ARD Matérn 3/2 kernel which is once-differentiable and the ARD SE and ARD RQ kernels which are infinitely differentiable. The GPR model based on the ARD Matérn 5/2 kernel is selected to optimize the range in the next section.

Table 5.2   Hyperparameters for C_L/C_D kernels

θ	ARD SE	ARD Matérn 3/2	ARD Matérn 5/2	ARD RQ
λ_1	0.01101	0.03962	0.02099	0.01224
λ_2	0.07618	0.1849	0.1100	0.07705
λ_3	0.1122	0.3302	0.1855	0.1165
λ_4	4.805	16.76	9.594	5.320
λ_5	45.69	130.6	79.59	48.87
σ_n	0.2359	0.1304	0.1992	0.2272
σ_f	9.365	13.56	11.84	9.720
α_{RQ}	–	–	–	4.074

Table 5.3   Performance metrics of the C_L/C_D kernels

	ARD SE	ARD Matérn 3/2	ARD Matérn 5/2	ARD RQ
MSE	0.09316	0.09086	0.08649	0.09219
max($\%Error$)	2.760	2.796	2.504	2.705

5.6.2   Regression model for endurance optimization

In the same way as for the range optimization, GPR model responses are plotted with their corresponding error bars for standard deviation alongside the true responses. These responses are shown in Figure 5.9, with the corresponding percent errors shown in Figure 5.10. The

optimized hyperparameters and performance metrics for each of the four kernels tested are listed in Tables 5.4 and 5.5.
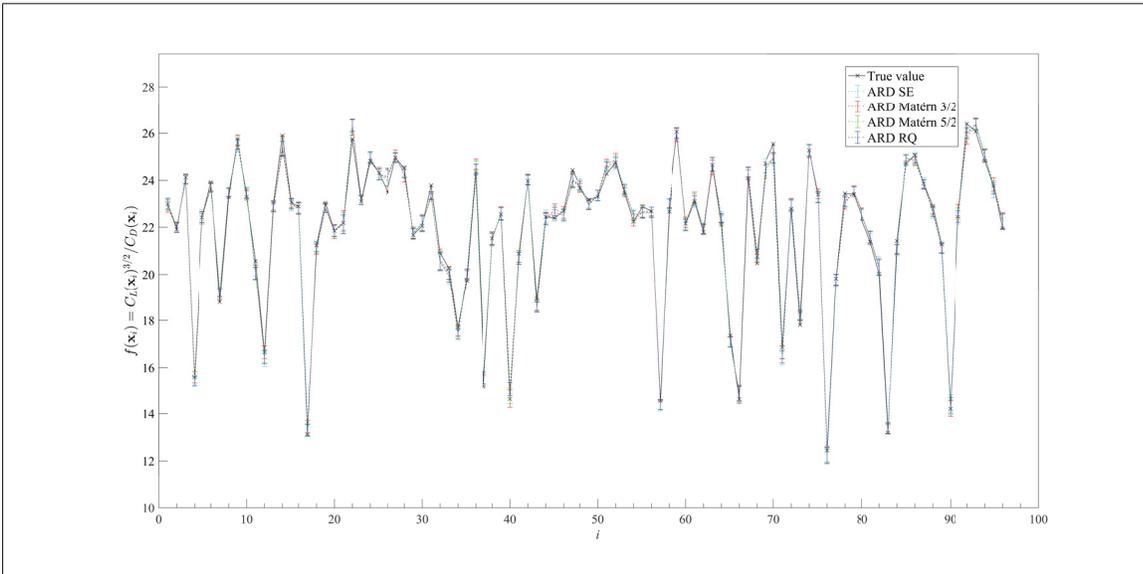
Figure 5.9   Predicted responses for $C_L^{3/2}/C_D$
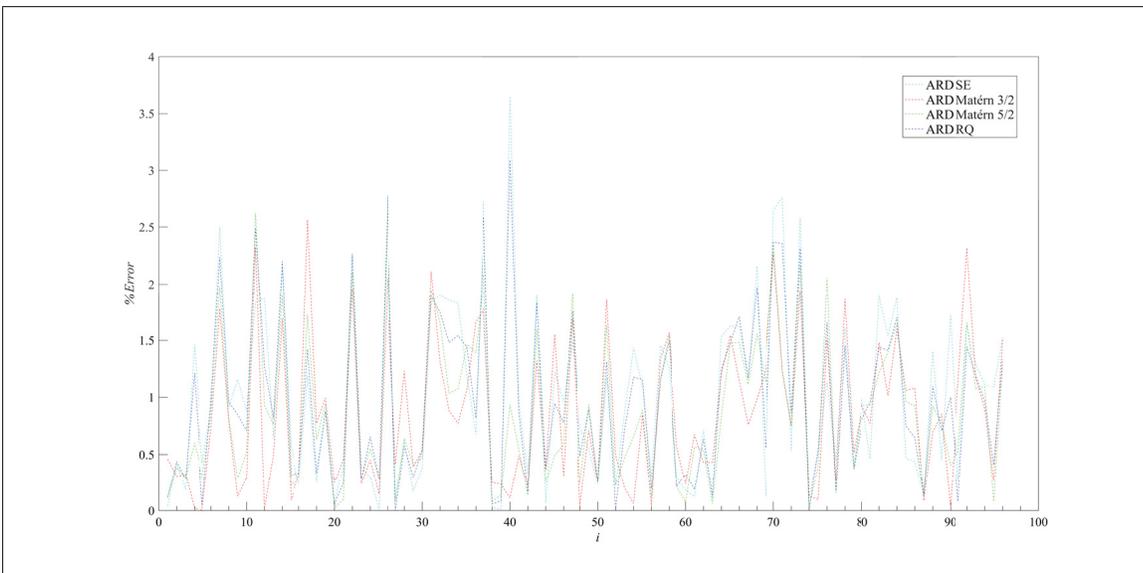
Figure 5.10   Percent errors on the predicted responses for $C_L^{3/2}/C_D$

Table 5.4 Hyperparameters for $C_L^{3/2}/C_D$ kernels

θ	ARD SE	ARD Matérn 3/2	ARD Matérn 5/2	ARD RQ
λ_1	0.01292	0.05741	0.02587	0.01567
λ_2	0.05292	0.2245	0.09912	0.06551
λ_3	0.1408	0.4533	0.2414	0.1626
λ_4	5.167	21.78	11.44	6.630
λ_5	44.59	156.5	87.44	56.65
σ_n	0.1872	0.08945	0.1514	0.1714
σ_f	8.769	16.25	12.91	10.28
α_{RQ}	–	–	–	1.476

Table 5.5 Performance metrics of the $C_L^{3/2}/C_D$ kernels

	ARD SE	ARD Matérn 3/2	ARD Matérn 5/2	ARD RQ
MSE	0.07082	0.05557	0.05603	0.06428
$\max(\%Error)$	3.653	2.563	2.626	3.091

The length scales show that $\lambda_1 < \lambda_2 < \lambda_3$ for all kernels, showing that the relative influence of δ_1 is the highest while that of δ_3 is the lowest in the morphing process. The ARD Matérn 3/2 kernel is chosen to model $C_L^{3/2}/C_D$ because it has the lowest MSE and the lowest maximum percent error. It also has the lowest tuned noise variance, which entails that the model fits the data more closely that the other models which have higher σ_n values.

5.7 Optimizer Settings

The parameters used to control the behaviour of the expected improvement optimization algorithm are explained in § 4.7. Table 5.6 lists the settings chosen for the morphing wing optimizations. This series of optimizations is performed with an optimization budget of 2 to

limit the number of additional evaluations allowed because of the number of optimizations envisaged.

Table 5.6   Parameters for the morphing wing
optimization algorithm

Setting	Value
Number of samples per iteration	500
Number of iterations	2000
Tolerance (%)	0.5
Optimization budget	2

5.8   Results

Twelve optimization runs for each objective function are used to find the best values for δ_1, δ_2 and δ_3 at α of $0°$, $4°$, $8°$ and $12°$ and MSL velocities of 15.87, 21.16 and 26.45 m/s, which correspond to Reynolds numbers of 0.6, 0.8 and 1.0×10^6. Contours of expected improvement for C_L/C_D and $C_L^{3/2}/C_D$ are shown in Figures 5.11 and 5.12, respectively. Each contour plot contains twelve validated values, with additional predicted values in the surrounding search space to fill the plot. Among the validated values, maximum improvement of 3.81 % is observed on C_L/C_D at $\alpha = 0°$ and V_{MSL} of 15.87 m/s. Likewise, the highest validated expected improvement on $C_L^{3/2}/C_D$ is of 3.95 % at $\alpha = 0°$ and V_{MSL} of 21.16 m/s.

It is observed that improvements are not reported for all flow conditions tested. There are ostensibly two possible underlying reasons in connection with the optimization process: the improvements have small, non-positive values within the specified tolerance, or the optimization budget is insufficient to find a suitable optimum. Additionally, it is to be noted that the functionality of the morphing model is restricted in that only three displacement locations are used as shown in Figure 5.2, limiting the deformation region. Improvements are found more frequently as the Reynolds number increases owing to the increasingly larger turbulent portion
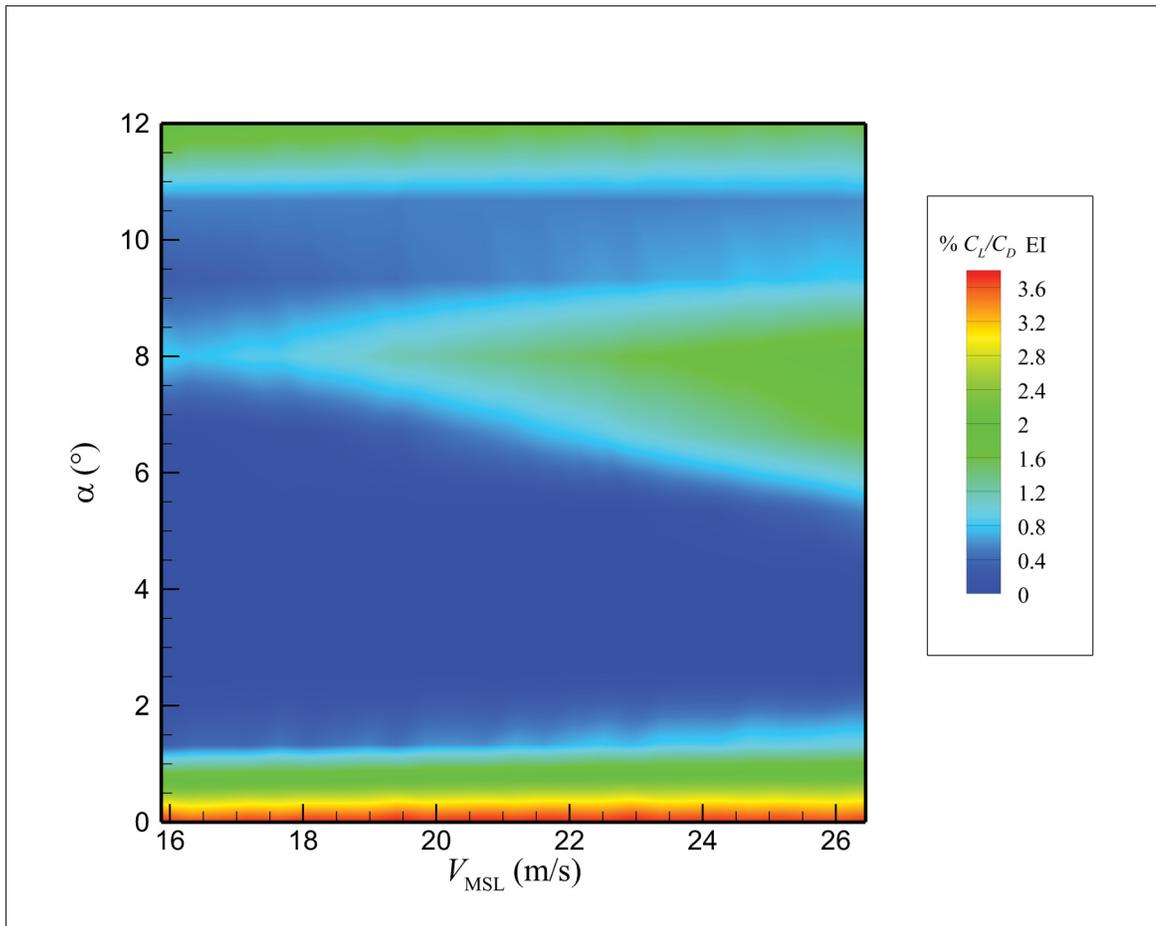
Figure 5.11   Contour of percent expected improvement through wing morphing
on C_L/C_D

of the associated boundary layer on the wing. At lower angles of attack, a greater proportion of the total drag is due to the viscous component. A delay in the onset of transition yields appreciable improvements in such cases as seen in Figure 5.13.

A sample case is chosen at α of 8° and MSL velocity of 26.45 m/s to be studied in greater detail because of the significant improvement observed in the previous results. Plots of turbulent kinetic energy in m^2/s^2 are used in Figure 5.13 to demonstrate the delay of the onset of laminar-to-turbulent transition within the boundary layer of the upper surface of the wing. The contour of turbulent kinetic energy for unmorphed wing is shown on the left in Figure 5.13 while that for the morphed wing is shown on the right. When the flow is laminar, there is no turbulent
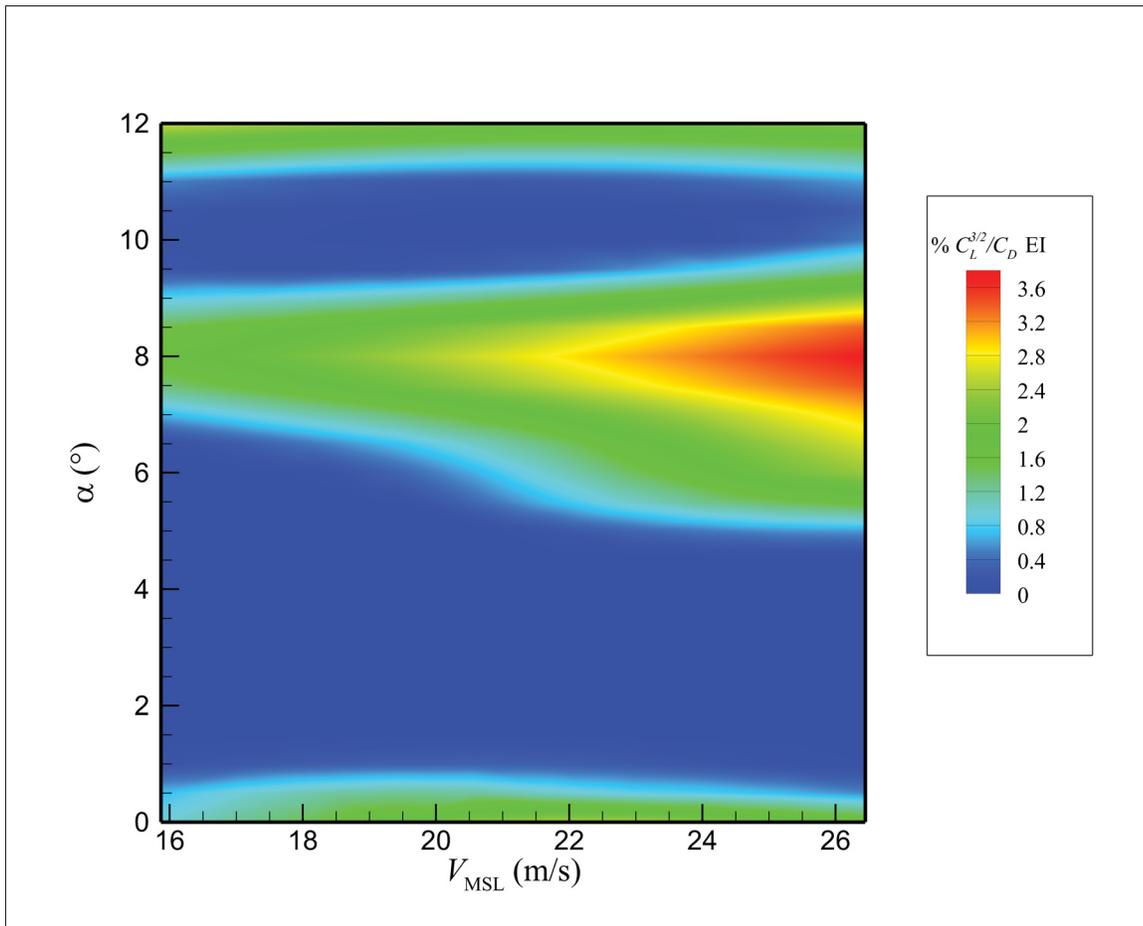
Figure 5.12   Contour of percent expected improvement through wing morphing on $C_L^{3/2}/C_D$

kinetic energy. The development of turbulence is characterized by a sudden jump in turbulent kinetic energy. This jump is observed on both the unmorphed and morphed wings; however, it can be noted that transition has successfully been delayed on the morphed wing. It can thus be surmised that a lower viscous drag coefficient is achieved based on the increased boundary layer laminarity of the morphed wing.

For the chosen sample case, pressure contours extracted at spanwise location $Z = 1.2$ m are shown in Figure 5.14 for the unmorphed wing on the left and for the morphed wing on the right. The change in pressure field due to the morphing process is noticeable, and is further investigated. In Figures 5.15 and 5.16, plots for the coefficient of pressure, C_P, are drawn at
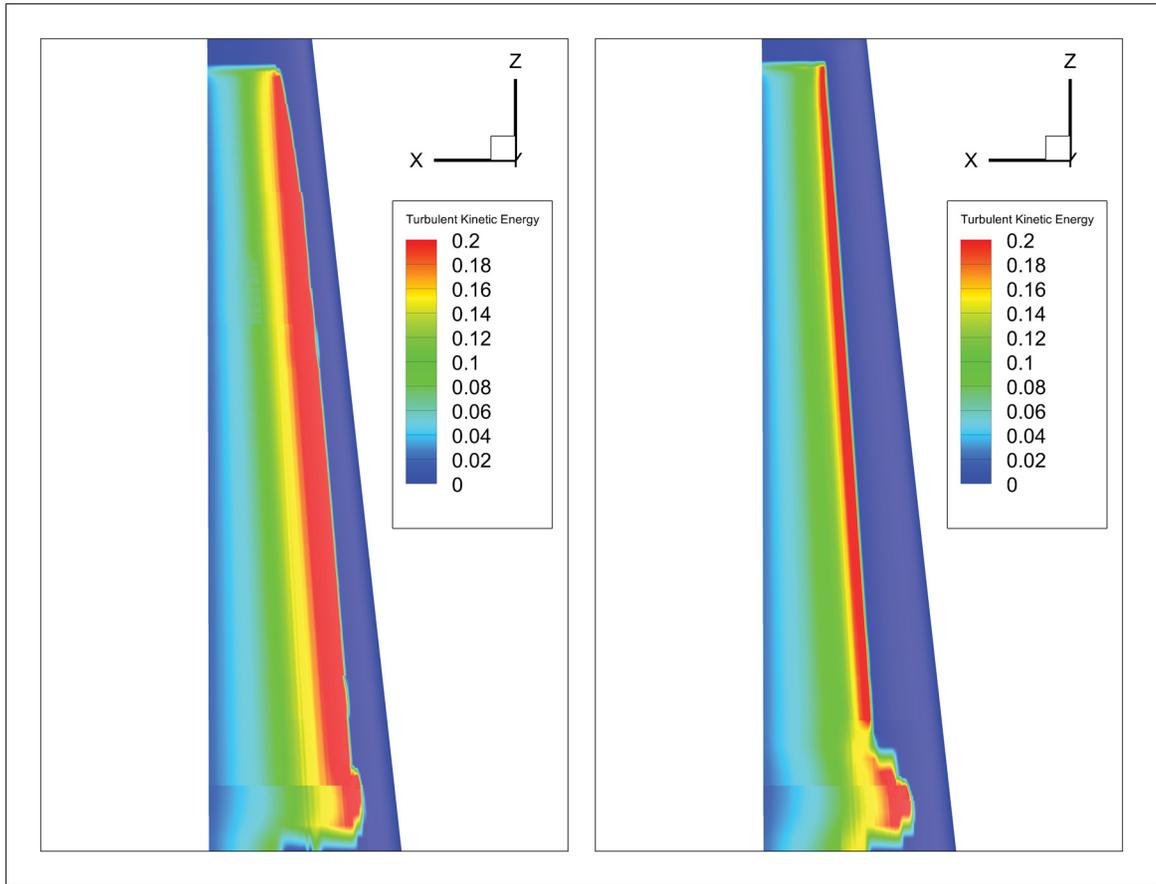
Figure 5.13   Turbulent kinetic energy for the unmorphed and morphed wings
at $\alpha = 8°$ and $V_{MSL} = 26.45$ m/s

seven evenly-spaced spanwise slices between $Z = 0.5$ m and $Z = 2.5$ m. This selection of slices allows insight into the pressure-related changes in the portion of the wing affected by the morphed geometry. The colour of each C_P curve matches a slice of the same colour drawn on the wing surface in the figure. The C_P curves show that greater suction is achieved on the upper surface of the wing by the morphed cross-section relative to the unmorphed cross-section, while the lower section is relatively unchanged; the morphed section is thus observed to generate more lift.
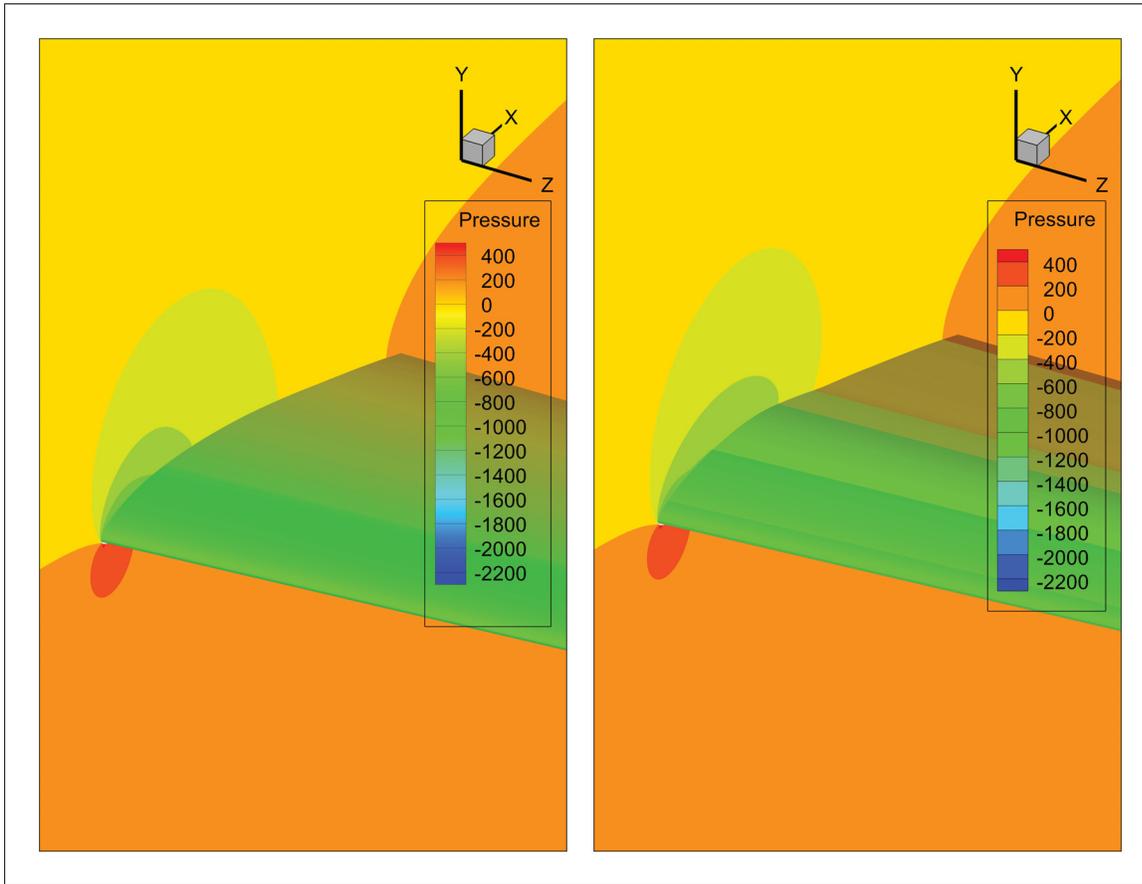
Figure 5.14   Pressure contours for the unmorphed and morphed wings
at $Z = 1.2$ m

5.9   Conclusions

The conceptual model for wing morphing tested in this chapter shows limitations for certain flight conditions where the optimization algorithm cannot locate improved solutions. Greater control of the upper surface of the wing through the use of more actuated rods could be conducive to better results. However, additional variables in modeling the morphing process would need to be introduced, making the construction of a reliable surrogate model more computationally intensive. The lack of convergence to an improved solution in cases where no improvement is obtained, and the use of both additional simulations allowed in the optimization budget at each optimization run suggest that the surrogate model may benefit from a larger initial training set than the one used. A higher optimization budget or an alternative acquisition function in
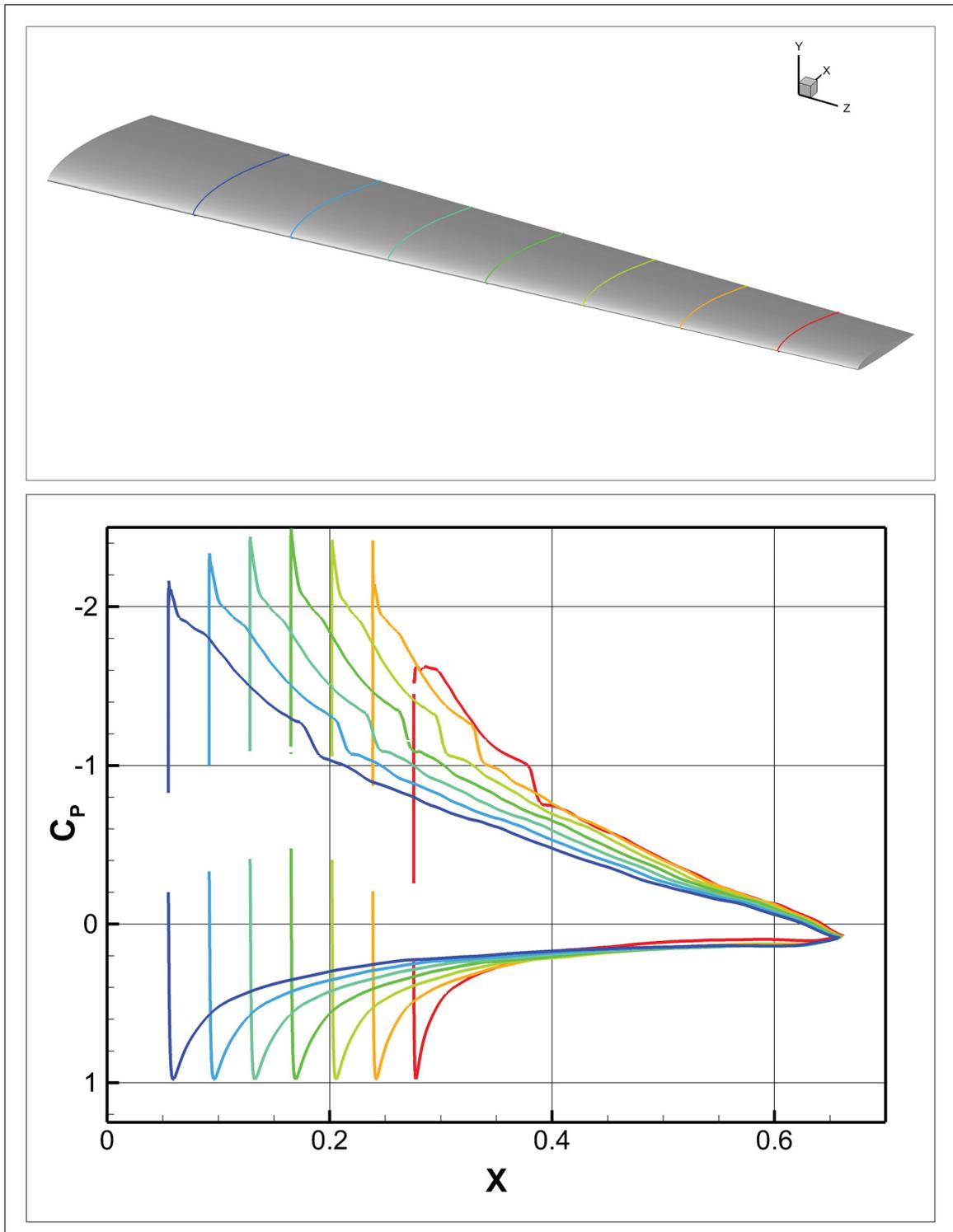
Figure 5.15   Pressure coefficients over seven slices of the unmorphed wing
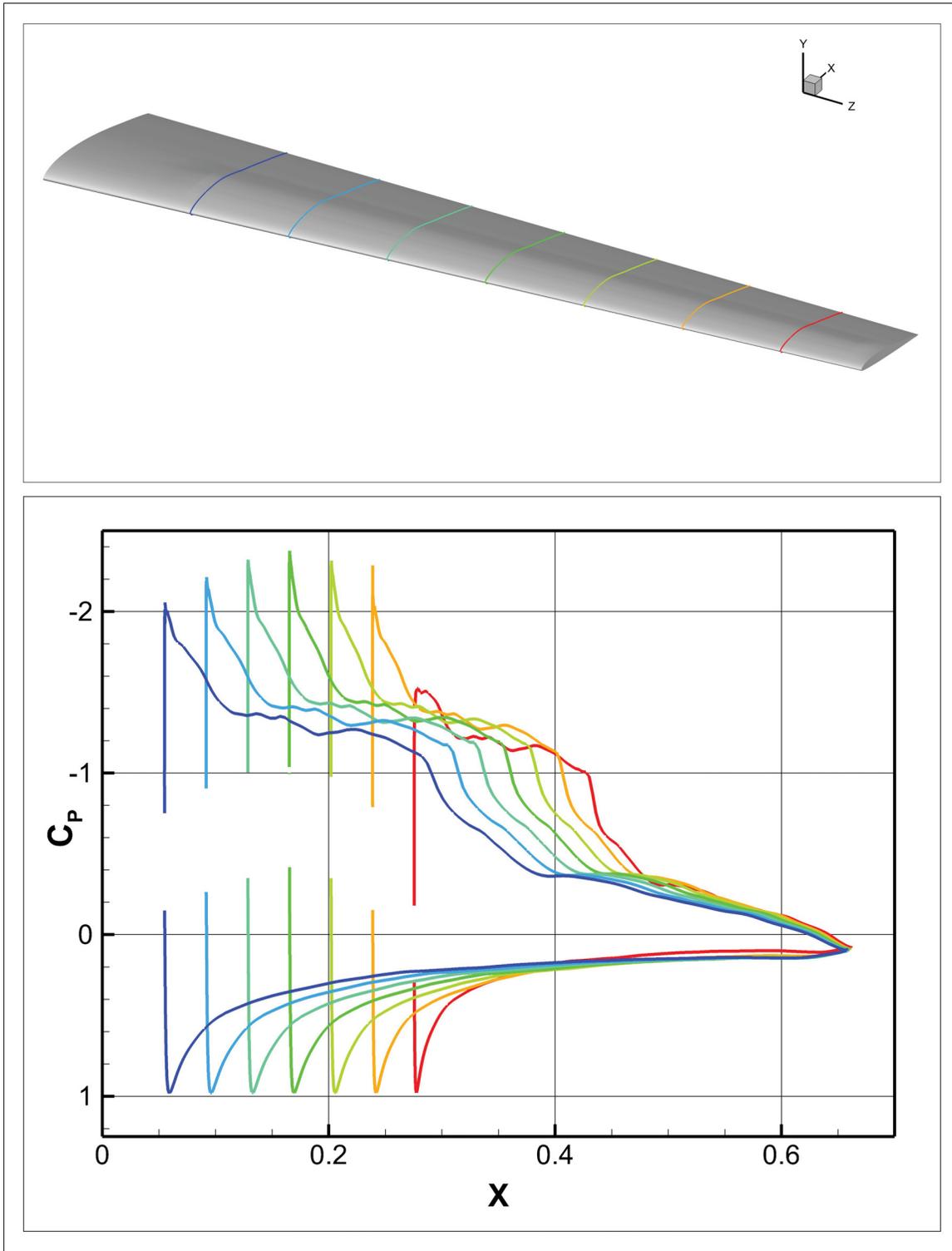
Figure 5.16   Pressure coefficients over seven slices of the morphed wing

the optimization algorithm could be used to further encourage convergence towards the optimal morphed geometry. However, there is no guarantee that an optimal morphed solution exists at every point in the flight envelope considered; improvements are obtained more consistently as the Reynolds number becomes higher, suggesting that more consistent improvements over all angles of attack can be obtained if the Reynolds number is sufficiently increased. To improve the surrogate model, a treed Gaussian process approach could be used to fit GPR models with distinct covariance structures in different regions of the design space so that each region can be locally tuned to better emulate the response of the CFD solver.

From an aerodynamic standpoint, two mechanisms capable of improving the aerodynamics of the wing have been shown in detail in the results. The delay in the onset of laminar-to-turbulent transition in the boundary layer of upper surface of the wing, which results in a reduction in viscous drag, was demonstrated using contours of turbulent kinetic energy. An altered pressure distribution on the morphed surface which results in greater suction, and therefore higher lift, was shown to occur in the sample case chosen. In the sample case presented, the combined increase in lift and reduction in viscous drag outweighed the increase in lift-induced drag, yielding an overall aerodynamic improvement. A third mechanism, flow separation delay, exists at angles of attack higher than those tested. This mechanism allows the boundary layer to remain attached to the surface longer, reducing drag significantly. In the raw results, the displacements δ_1 and δ_2 tend towards the upper morphing limit; such a pattern suggests that the optimization of the baseline airfoil shape could be a valuable precursor to the implementation and testing of a morphing wing model so that the morphing process can yield greater aerodynamic enhancements.

Finally, the range of percent improvements obtained in this morphing wing study is in agreement with results obtained at the LARCASE by Sugar Gabor *et al.* (2015), who reported up to about 4 % improvement on C_L/C_D for morphed wing configurations. Improvements were obtained for all angles of attack considered in these tests conducted at higher Reynolds numbers.

CONCLUSIONS

High-fidelity numerical simulations were conducted in this thesis to evaluate three approaches to maximize the aerodynamic performance of the Hydra Technologies S45 Bàalam wing. Gaussian processes were used to construct surrogate models which allowed several opimization results to be obtained from the same set of simulations. They proved to be an effective method for optimization using the expected improvement acquistion function. The use of GPR models allowed the optimization process to be carried out under uncertainty by incuding a hyperparameter for noise; this noise term holistically takes into account errors inherent to most computational results, such as round-off error, spatial discretization error, and iterative convergence error. The relative influence of design parameters was established by comparing their corresponding length scales; this process is more economical than sensitivity studies which require separate sets of results to obtain gradient information.

The impact of an upswept blended winglet on the aerodynamic performance of the UAV wing was studied in Chapter 3 by comparing simulation results for the baseline wing without the winglet against those with the winglet. Improvements were observed through the general increase in lift and reduction in pressure drag. A global optimization of the wing geometry in Chapter 4 showed that the only effective approach to significantly impact the aerodynamic efficiency of the wing using planform parameters is to increase the wing aspect ratio. Aspect ratio modifications present major structural changes because they are achieved by either reducing the wing area, which increases wing loading, or by increasing the wing span, which increases the bending moment of the wing. Wing twist was found to be instrumental in the compromise between maximized range and maximized endurance, highlighting the need for the inclusion of other disciplines in the design process. Chapter 5 presented a morphing wing study and paved the way for future analyses with the developed tools. The need for an optimized baseline airfoil was identified and a dependency on the Reynolds number for obtaining improvements was established.

RECOMMENDATIONS

Additional investigations of the impact of the tested winglet for flows with a spanwise component are recommended. The additional out-of-plane area of the wing owing to the winglet makes the wing particularly susceptible to the development of side forces in asymmetric flow fields, thereby affecting the stability derivatives of the wing. The morphing wing model can be refined by implementing an impact factor which is representative of the flexible morphing skin. Such a deformation model can be obtained after the design of the composite skin through finite element analysis or bench tests. The model can be validated experimentally through wind tunnel tests. The training set can be used further in conjunction with results from a different-fidelity emulator, such as a vortex lattice method or experimental results obtained through wind tunnel testing, to develop a multi-fidelity model capable of predicting the true response more accurately. Bayesian partitioning of the search space to construct treed GPR models could be effective, allowing different length scales, noise terms and scale factors to be used at different locations in the search space. The expected improvement algorithm is known to be a greedy algorithm – that is, it selects the best immediate solution at each step, which may not be ideal given the uncertainty on the CFD results. Modifications to its acquisition function have been proposed in the literature, or alternatives such as entropy search methods can be used.

APPENDIX I

TRAINING SET FOR GLOBAL WING AERODYNAMICS

Table-A I-1   Training set values for global wing aerodynamic optimization

Sample No.	x_1	x_2	x_3	x_4
1	3.8318	3.6931	10.5282	0.5171
2	9.0315	2.2241	11.3123	0.5350
3	2.8344	0.3773	10.3322	0.4397
4	4.1977	3.5334	11.8882	0.4564
5	1.3466	2.4688	11.0446	0.6901
6	5.2000	1.6771	9.3732	0.5260
7	6.5761	3.8562	9.2506	0.5730
8	6.7020	3.7538	9.8140	0.4853
9	8.8420	1.4707	11.3594	0.5645
10	4.3756	1.1719	11.9442	0.5497
11	5.0675	2.6267	11.6591	0.3439
12	8.7024	3.3631	9.3899	0.4189
13	6.9611	1.8553	10.1742	0.4826
14	8.0243	2.5159	10.8870	0.3389
15	3.5637	0.8836	10.5639	0.4588
16	6.0722	1.1293	9.9680	0.4070
17	6.0722	1.1293	9.9680	0.4070
18	2.4875	0.7735	11.2580	0.4284
19	1.0742	1.5049	8.6505	0.3922
20	2.1762	2.9184	11.7883	0.4739
21	5.7384	0.0684	11.7749	0.5791
22	0.4826	0.1477	11.1838	0.3110

23	7.9209	1.6070	10.4487	0.3902
24	1.8672	1.7711	11.0712	0.5999
25	3.0296	2.0331	10.0415	0.6176
26	4.9620	3.2602	11.5203	0.5580
27	2.2193	0.2290	11.4750	0.6479
28	3.3234	1.9717	8.9801	0.3779
29	0.2114	2.7088	9.5837	0.6060
30	9.4765	0.7237	9.5998	0.6749
31	7.2420	3.4545	9.7568	0.3619
32	4.4970	2.7765	10.7232	0.4141
33	0.8938	0.5650	8.5398	0.5154
34	4.7345	1.2929	10.9720	0.4419
35	5.5741	3.0006	9.1330	0.5903
36	9.3232	2.1397	10.2412	0.3023
37	3.7570	2.4137	10.2659	0.3676
38	7.5934	3.5986	9.6999	0.6095
39	8.3450	0.6247	9.9418	0.6985
40	2.7639	3.9956	9.0670	0.6814
41	6.2249	0.2591	8.6268	0.6665
42	8.5838	0.4663	10.6650	0.3256
43	1.7632	1.3392	10.8051	0.3509
44	7.0592	3.2165	8.8429	0.3200
45	0.6162	2.3269	9.1796	0.5074
46	0.1497	2.8962	9.5183	0.6569
47	1.5957	1.0541	11.6115	0.4952
48	5.8079	0.9374	8.8832	0.6312
49	0.8865	1.6768	10.8466	0.6203
50	1.7881	2.7409	9.9606	0.6873

51	3.3174	0.8178	10.4554	0.4254
52	3.8090	3.5125	8.9914	0.5769
53	5.1726	0.1096	9.1934	0.6506
54	5.9450	0.7378	8.7285	0.3881
55	2.8767	3.1413	9.9984	0.4399
56	2.5615	3.4159	8.8379	0.4871
57	5.9629	1.9769	8.9451	0.3807
58	5.0798	3.3862	10.5886	0.5562
59	1.2920	0.3186	9.2910	0.4932
60	4.9303	2.0210	8.8743	0.5021

APPENDIX II

TRAINING SET FOR MORPHING WING AERODYNAMICS

Table-A II-1   Training set values for morphing wing aerodynamic optimization

Sample No.	x_1	x_2	x_3	x_4	x_5
1	4.698E-03	7.833E-04	6.428E-04	7.135	17.659
2	7.688E-03	3.476E-03	8.203E-04	2.428	26.853
3	5.193E-05	6.183E-03	9.969E-04	7.888	21.964
4	3.905E-03	3.576E-03	3.656E-03	1.062	16.592
5	2.307E-03	3.375E-04	9.090E-03	2.909	25.260
6	1.256E-03	4.394E-03	5.314E-03	8.474	22.708
7	2.609E-03	5.834E-03	5.662E-03	2.342	15.667
8	4.462E-03	4.076E-03	8.708E-03	7.398	19.846
9	4.568E-03	9.412E-03	2.268E-03	5.285	23.788
10	5.948E-03	4.977E-03	4.042E-03	10.538	27.393
11	5.014E-03	8.441E-03	6.925E-03	3.097	15.542
12	6.848E-03	1.496E-03	9.592E-03	0.817	27.972
13	2.957E-03	1.640E-03	6.087E-03	7.715	18.678
14	8.982E-03	7.542E-03	4.210E-04	8.151	27.555
15	6.345E-04	3.162E-03	8.199E-03	9.926	22.468
16	6.583E-03	1.772E-03	3.266E-03	10.814	25.868
17	4.879E-03	8.856E-03	8.349E-03	0.013	21.742
18	6.132E-03	2.551E-03	4.827E-03	2.631	22.995
19	1.959E-03	6.885E-03	9.204E-03	6.816	17.384
20	2.691E-03	6.802E-03	8.146E-03	11.554	22.252
21	8.431E-03	7.760E-03	5.730E-03	11.783	24.640
22	9.731E-03	5.570E-03	2.498E-03	5.955	26.253

23	4.128E-03	7.002E-03	1.244E-03	10.137	24.686
24	7.483E-03	2.799E-03	2.166E-03	7.565	24.212
25	8.747E-03	2.292E-03	1.008E-03	3.879	26.435
26	9.254E-03	8.123E-03	1.849E-03	4.717	18.047
27	1.141E-03	3.708E-03	3.034E-03	6.637	23.473
28	7.297E-04	9.757E-03	7.514E-03	5.763	20.363
29	2.409E-03	5.824E-03	5.976E-03	10.660	19.131
30	9.058E-03	5.249E-03	1.404E-04	10.352	19.699
31	1.476E-03	9.647E-04	1.802E-03	4.085	19.381
32	5.208E-03	9.534E-03	9.396E-03	11.930	17.795
33	9.630E-03	3.950E-03	6.182E-03	1.989	22.746
34	5.747E-03	4.829E-03	2.835E-03	1.354	20.205
35	7.202E-03	3.234E-03	3.715E-03	1.667	27.725
36	4.330E-03	2.026E-03	7.711E-03	5.101	23.661
37	7.113E-03	8.270E-03	2.682E-03	0.696	16.846
38	8.521E-03	4.542E-03	6.767E-03	11.365	20.009
39	1.925E-04	8.148E-05	9.792E-03	9.086	18.481
40	8.077E-03	5.077E-03	8.971E-03	0.201	25.429
41	9.856E-03	2.340E-03	3.480E-03	2.037	26.611
42	7.842E-03	4.199E-03	5.031E-03	3.481	27.183
43	3.362E-03	7.995E-03	7.309E-03	1.405	23.194
44	8.191E-03	2.882E-03	8.623E-03	8.820	17.273
45	1.650E-03	8.589E-03	2.530E-03	3.681	16.954
46	5.391E-03	5.342E-03	2.816E-04	11.194	26.058
47	9.383E-03	2.964E-04	1.503E-03	6.181	21.031
48	3.732E-03	9.122E-03	4.956E-03	9.587	25.644
49	3.533E-03	6.153E-03	7.078E-03	9.310	21.589
50	1.828E-03	9.929E-03	6.448E-03	9.725	24.265

51	3.716E-04	1.982E-03	4.182E-03	4.405	20.924
52	6.711E-03	1.228E-03	9.939E-03	5.566	24.917
53	3.123E-03	9.200E-03	6.594E-03	8.205	21.260
54	3.290E-03	6.384E-03	4.581E-03	3.247	20.727
55	5.561E-03	5.390E-04	5.344E-03	4.835	18.364
56	9.330E-04	7.368E-03	7.915E-03	6.409	15.842
57	6.201E-03	7.192E-03	7.381E-03	0.466	19.024
58	2.092E-03	8.762E-03	3.851E-03	6.305	16.179
59	6.370E-03	6.529E-03	1.495E-03	4.397	28.294
60	7.502E-03	1.062E-03	4.413E-03	8.729	16.451
61	4.170E-03	6.705E-03	9.835E-04	5.375	16.720
62	7.203E-03	4.173E-03	4.211E-03	10.903	20.741
63	1.144E-06	5.587E-03	9.579E-03	3.523	24.358
64	3.023E-03	1.404E-03	5.332E-03	3.453	20.743
65	1.468E-03	1.981E-03	6.919E-03	1.560	16.044
66	9.234E-04	8.007E-03	3.155E-03	0.232	22.313
67	1.863E-03	9.683E-03	6.865E-03	8.146	23.963
68	3.456E-03	3.134E-03	8.346E-03	2.540	22.042
69	3.968E-03	6.923E-03	1.829E-04	3.187	27.585
70	5.388E-03	8.764E-03	7.501E-03	5.899	22.967
71	4.150E-03	8.857E-03	9.790E-03	0.634	26.783
72	6.852E-03	8.504E-04	7.482E-03	6.889	17.173
73	2.024E-03	3.866E-04	2.776E-03	1.743	17.025
74	8.781E-03	1.698E-03	7.893E-03	7.072	25.815
75	2.739E-04	8.781E-03	1.032E-03	8.397	20.530
76	0	0	0	0.000	15.868
77	0	0	0	2.000	15.868
78	0	0	0	4.000	15.868

79	0	0	0	6.000	15.868
80	0	0	0	8.000	15.868
81	0	0	0	10.000	15.868
82	0	0	0	12.000	15.868
83	0	0	0	0.000	21.158
84	0	0	0	2.000	21.158
85	0	0	0	4.000	21.158
86	0	0	0	6.000	21.158
87	0	0	0	8.000	21.158
88	0	0	0	10.000	21.158
89	0	0	0	12.000	21.158
90	0	0	0	0.000	26.447
91	0	0	0	2.000	26.447
92	0	0	0	4.000	26.447
93	0	0	0	6.000	26.447
94	0	0	0	8.000	26.447
95	0	0	0	10.000	26.447
96	0	0	0	12.000	26.447

BIBLIOGRAPHY

Anderson, J. D. (1999). *Aircraft performance and design*. McGraw-Hill Science/Engineering/Math.

Anderson Jr, J. D. (2010). *Fundamentals of aerodynamics*. Tata McGraw-Hill Education.

ANSYS Inc., F. (2006). Introductory FLUENT Training: Solver Settings, FLUENT v6.3. Fluent User Services Center.

ANSYS Inc., F. (2016). ANSYS FLUENT 17.0 Theory Guide. ANSYS. Inc.

Back, T. (1996). *Evolutionary algorithms in theory and practice: evolution strategies, evolutionary programming, genetic algorithms*. Oxford university press.

Barbarino, S., Bilgen, O., Ajaj, R. M., Friswell, M. I. & Inman, D. J. (2011). A review of morphing aircraft. *Journal of intelligent material systems and structures*, 22(9), 823–877.

Batchelor, G. (1970). An Introduction to Fluid Dynamics. Cambridge University Press.

Beckert, A. (2000). Coupling fluid (CFD) and structural (FE) models using finite interpolation elements. *Aerospace Science and technology*, 4(1), 13–22.

Bernardo, J., Berger, J., Dawid, A., Smith, A. et al. (1998). Regression and classification using Gaussian process priors. *Bayesian statistics*, 6, 475.

Chattot, J. J. & Hafez, M. M. (2015). *Theoretical and Applied Aerodynamics: And Related Numerical Methods*. Springer.

Chen, S. & Doolen, G. D. (1998). Lattice Boltzmann method for fluid flows. *Annual review of fluid mechanics*, 30(1), 329–364.

Clancy, L. J. (1975). *Aerodynamics*. Halsted Press.

Conley, N. (1980). Winglet toe-out angle optimization for the gates Learjet longhorn wing. *Journal of Aircraft*, 17(12), 851–855.

Conn, A. R., Scheinberg, K. & Vicente, L. N. (2009). *Introduction to derivative-free optimization*. SIAM.

Daude, M. (1984). Winglets for aircraft wing tips. Google Patents. US Patent 4,457,479.

Drela, M. (1989). XFOIL: An analysis and design system for low Reynolds number airfoils. In *Low Reynolds number aerodynamics* (pp. 1–12). Springer.

Ebden, M. et al. (2008). Gaussian processes for regression: A quick introduction. *The Website of Robotics Research Group in Department on Engineering Science, University of Oxford*.

Edwards, P. N. (2012). Entangled histories: Climate science and nuclear weapons research. *Bulletin of the Atomic Scientists*, 68(4), 28–40.

Ehlers, F. E., Epton, M. A., Johnson, F. T., Magnus, A. E. & Rubbert, P. E. (1979). A higher order panel method for linearized supersonic flow. *AIAA Paper 76-381*.

Elger, D. F. & Roberson, J. A. (2013). *Engineering fluid mechanics*. Wiley Hoboken (NJ).

Eppler, R. (1997). Induced drag and winglets. *Aerospace science and Technology*, 1(1), 3–15.

ESDU, I. (1976). Geometrical properties of cranked and straight-tapered wing planforms. London: ESDU 76003.

Falcão, L., Gomes, A. A. & Suleman, A. (2011). Aero-structural design optimization of a morphing wingtip. *Journal of Intelligent Material Systems and Structures*, 22(10), 1113–1124.

Felker, F. F. (2002). Aircraft with elliptical winglets. Google Patents. US Patent 6,484,968.

Finch, R. V. (1978). Vortex reducing wing tip. Google Patents. US Patent 4,108,403.

Floudas, C. A., Pardalos, P. M., Adjiman, C., Esposito, W. R., Gümüs, Z. H., Harding, S. T., Klepeis, J. L., Meyer, C. A. & Schweiger, C. A. (2013). *Handbook of test problems in local and global optimization*. Springer Science & Business Media.

Forrester, A., Keane, A. et al. (2008). *Engineering design via surrogate modelling: a practical guide*. John Wiley & Sons.

Forrester, A. I. & Keane, A. J. (2009). Recent advances in surrogate-based optimization. *Progress in Aerospace Sciences*, 45(1), 50–79.

Galdi, G. (2011). *An introduction to the mathematical theory of the Navier-Stokes equations: Steady-state problems*. Springer Science & Business Media.

Govan, A. (2006). Introduction to optimization. *North Carolina State University, SAMSI NDHS, Undergraduate workshop*.

Gratzer, L. B. (1992). Spiroid-tipped wing. Google Patents. US Patent 5,102,068.

Grigorie, T. L., Botez, R. M. & Popov, A. V. (2012a). Fuzzy logic control of a smart actuation system in a morphing wing. In *Fuzzy Controllers-Recent Advances in Theory and Applications*. InTech.

Grigorie, T. L., Botez, R. M., Popov, A. V., Mamou, M. & Mébarki, Y. (2012b). A hybrid fuzzy logic proportional-integral-derivative and conventional on-off controller for morphing wing actuation using shape memory alloy Part 1: Morphing system mechanisms and controller architecture design. *The Aeronautical Journal*, 116(1179), 433–449.

Härdle, W. (1990). *Applied nonparametric regression*. Cambridge university press.

Hemke, P. E. (1928). Drag of wings with end plates. *NACA Rep. 267*.

Heuveline, V. & Latt, J. (2007). The OpenLB project: an open source and object oriented implementation of lattice Boltzmann methods. *International Journal of Modern Physics C*, 18(04), 627–634.

Heyson, H. H., Riebe, G. D. & Fulton, C. L. (1977). Theoretical parametric study of the relative advantages of winglets and wing-tip extensions. *NASA TP 1020*.

Hinze, J. (1975). Turbulence McGraw-Hill. *New York*, 218.

Jeong, J. & Hussain, F. (1995). On the identification of a vortex. *Journal of fluid mechanics*, 285, 69–94.

Jewel, J. W. (1965). Operational Experiences of General Aviation Aircraft. *Conference on Aircraft Operating Problems, NASA SP-83*.

Johnson, W. (1972). Lifting-surface theory for calculating the loading induced on a wing by a flap. *NASA TN D-6798*.

Jones, D. R., Schonlau, M. & Welch, W. J. (1998). Efficient global optimization of expensive black-box functions. *Journal of Global optimization*, 13(4), 455–492.

Jones, R. T. (1950). *The spanwise distribution of lift for minimum induced drag of wings having a given lift and a given bending moment*.

Jupp, J. A. & Rees, P. H. (1987). Aircraft wing and winglet arrangement. Google Patents. US Patent 4,714,215.

Katz, J. & Plotkin, A. (2001). *Low-speed aerodynamics*. Cambridge university press.

König, B., Fares, E. & Broeren, A. P. (2015, 06). Lattice-Boltzmann Analysis of Three-Dimensional Ice Shapes on a NACA 23012 Airfoil. *SAE Technical Paper*. doi: 10.4271/2015-01-2084.

Kocijan, J. & Petelin, D. (2011). Output-error model training for Gaussian process models. *International Conference on Adaptive and Natural Computing Algorithms*, pp. 312–321.

Koreanschi, A., Şugar Gabor, O., Botez, R. M. et al. (2014). New numerical study of boundary layer behavior on a morphing wing-with-aileron system. *American Institute of Aeronautics and Astronautics AIAA 32nd Applied Aerodynamics Conference, Atlanta, GA, USA*, pp. 16–20. doi: 10.2514/6.2014-3170.

Koreanschi, A., Sugar Gabor, O. & Botez, R. M. (2015). Numerical and experimental validation of an optimized wing geometry using small wind tunnel testing. *33rd AIAA Applied Aerodynamics Conference, AIAA, Houston, TX, USA*. doi: 10.2514/6.2015-3386.

Koreanschi, A., Şugar Gabor, O., Acotto, J., Botez, R. M., Mamou, M. & Mebarki, Y. (2016a). A genetic algorithm optimization method for a morphing wing tip demonstrator validated using infra red experimental data. *34th AIAA Applied Aerodynamics Conference, AIAA Aviation, Washington, DC, USA*. doi: 10.2514/6.2016-4037.

Koreanschi, A., Şugar Gabor, O., Ayrault, T., Botez, R. M., Mamou, M. & Mebarki, Y. (2016b). Numerical optimization and experimental testing of a morphing wing with aileron system. *24th AIAA/AHS Adaptive Structures Conference*, pp. 1083. doi: 10.2514/6.2016-1083.

Koreanschi, A., Gabor, O. S., Acotto, J., Brianchon, G., Portier, G., Botez, R. M., Mamou, M. & Mebarki, Y. (2017). Optimization and design of an aircraft's morphing wing-tip demonstrator for drag reduction at low speeds, Part II-Experimental validation using Infra-Red transition measurement from Wind Tunnel tests. *Chinese Journal of Aeronautics*, 30(1), 164–174.

Koziel, S. & Leifsson, L. (2013). Surrogate-based modeling and optimization. *Applications in Engineering*.

Kuethe, A. M. & Chow, C.-Y. (1997). *Foundations of aerodynamics: bases of aerodynamic design*. John Wiley & Sons, Inc.

La Roche, U. & Palffy, S. (1996). Wing-grid, a novel device for reduction of induced drag on wings. *ICAS PROCEEDINGS*, 20, 2303–2309.

Lamar, J. & Margason, R. (1971). Vortex-lattice FORTRAN program for estimating subsonic aerodynamic characteristics of complex planforms. *NASA TN D-6142*.

Latt, J. Palabos, parallel lattice Boltzmann solver, http://www.palabos.org.

Launder, B. E. & Spalding, D. B. (1972). *Mathematical models of turbulence*. Academic press.

Leschziner, M. (2010). Reynolds-Averaged Navier–Stokes Methods. *Encyclopedia of aerospace engineering*.

Luo, L.-S. (2000). Theory of the lattice Boltzmann method: Lattice Boltzmann models for nonideal gases. *Physical Review E*, 62(4), 4982.

Lyu, Z. & Martins, J. R. (2015). Aerodynamic shape optimization of an adaptive morphing trailing-edge wing. *Journal of Aircraft*, 52(6), 1951–1970. doi: 10.2514/1.C033116.

Mangler, W. (1938). The lift distribution of wings with end plates. *NACA TM-856*.

Marchman, I., Manor, D. & Faery,JR, H. (1978). Whitcomb winglet applications to general aviation aircraft. *Aircraft Systems and Technology Conference*, pp. 1478.

Maughmer, M. D. (2003). Design of winglets for high-performance sailplanes. *Journal of Aircraft*, 40(6), 1099–1106.

Maughmer, M. D. (2006). The design of winglets for low-speed aircraft. *Technical Soaring*, 30(3), 6173.

McBain, G. (2012). *Theory of Lift: Introductory Computational Aerodynamics in MATLAB/Octave*. John Wiley & Sons.

McCormick, B. W. (1995). *Aerodynamics, aeronautics, and flight mechanics*. Wiley New York.

McLean, D. (2012). *Understanding aerodynamics: arguing from the real physics*. John Wiley & Sons.

Menter, F. R., Langtry, R. B., Likki, S., Suzen, Y., Huang, P. & Völker, S. (2006). A correlation-based transition model using local variables—Part I: model formulation. *Journal of turbomachinery*, 128(3), 413–422.

Menter, F. R. et al. (1994). Two-equation eddy-viscosity turbulence models for engineering applications. *AIAA Journal*, 32(8), 1598–1605.

Mestrinho, J., Gamboa, P. & Santos, P. (2011). Design optimization of a variable-span morphing wing for a small UAV. *Proceedings of the 52nd AIAA/ASME/ASCE/AHS/ASC Structures, Structural Dynamics and Materials Conference, Denver, CO, USA*, 47. doi: 10.2514/6.2011-2025.

Moin, P. & Mahesh, K. (1998). Direct numerical simulation: a tool in turbulence research. *Annual review of fluid mechanics*, 30(1), 539–578.

Moore, G. E. (1998). Cramming more components onto integrated circuits. *Proceedings of the IEEE*, 86(1), 82–85.

Moran, J. (1984). *An introduction to theoretical and computational aerodynamics*. Courier Corporation.

Mueller, T. J. & DeLaurier, J. D. (2003). Aerodynamics of Small Vehicles. *Annual Review of Fluid Mechanics*, 35(1), 89-111. doi: 10.1146/annurev.fluid.35.101101.161102.

Munk, M. M. (1923). The minimum induced drag of aerofoils. *NASA TR-121*.

Münsch, M. & Breuer, M. (2011). Numerical simulation of fluid–structure interaction using eddy–resolving schemes. In *Fluid Structure Interaction II* (pp. 221–253). Springer.

Munson, K. (2015). *Jane's unmanned aerial vehicles and targets*. Jane's Information Group Limited.

Murphy, K. P. (2012). *Machine learning: a probabilistic perspective*. MIT press.

Nicolai, L. M. & Carichner, G. (2001). *Fundamentals of aircraft and airship design*. American Institute of Aeronautics and Astronautics.

Oskam, B. (1985). Transonic panel method for the full potential equation applied to multi-component airfoils. *AIAA journal*, 23(9), 1327–1334.

Panagiotou, P., Kaparos, P. & Yakinthos, K. (2014). Winglet design and optimization for a MALE UAV using CFD. *Aerospace Science and Technology*, 39, 190–205.

Pitsch, H. (2006). Large-eddy simulation of turbulent combustion. *Annu. Rev. Fluid Mech.*, 38, 453–482.

Quintana, E. (2008). The ethics and legal implications of military unmanned vehicles. *RUSI, Occasional Paper*.

Rasmussen, C. E. & Williams, C. K. (2004). Gaussian processes in machine learning. *Lecture notes in computer science*, 3176, 63–71.

Rodriguez, A. R. (2007). Morphing aircraft technology survey. *45th AIAA aerospace sciences meeting and exhibit*, pp. 2007–1258.

Roskam, J. & Lan, C.-T. E. (1997). *Airplane aerodynamics and performance*. DARcorporation.

Simpson, R. J., Palacios, R. & Murua, J. (2013). Induced-drag calculations in the unsteady vortex lattice method. *AIAA journal*.

Smith, D., Lowenberg, M., Jones, D. & Friswell, M. (2014). Computational and experimental validation of the active morphing wing. *Journal of Aircraft*, 51(3), 925–937. doi: 10.2514/1.C032262.

Smith, M., Komerath, N., Ames, R., Wong, O. & Pearson, J. (2001). Performance analysis of a wing with multiple winglets. *19th AIAA Applied Aerodynamics Conference, Anaheim, CA, USA*. doi: 10.2514/6.2001-2407.

Snoek, J., Larochelle, H. & Adams, R. P. (2012). Practical bayesian optimization of machine learning algorithms. *Advances in neural information processing systems*, pp. 2951–2959.

Sóbester, A. & Forrester, A. I. (2014). *Aircraft aerodynamic design: geometry and optimization*. John Wiley & Sons.

Spalart, P. R. & Allmaras, S. R. (1992). A one equation turbulence model for aerodynamic flows. *30th Aerospace Sciences Meeting and Exhibit*. doi: 10.2514/6.1992-439.

Stein, M. L. (2012). *Interpolation of spatial data: some theory for kriging*. Springer Science & Business Media.

Succi, S. (2001). *The lattice Boltzmann equation: for fluid dynamics and beyond*. Oxford university press.

Sugar Gabor, O., Koreanschi, A. & Botez, R. M. (2013a). Optimization of an Unmanned Aerial System'wing using a flexible skin morphing wing. *SAE International Journal of Aerospace*, 6(2013-01-2095), 115–121.

Sugar Gabor, O., Koreanschi, A. & Botez, R. M. (2013b). Unmanned Aerial System Hydra Technologies Éhecatl wing optimization using a morphing approach. *AIAA Atmospheric Flight Mechanics (AFM) Conference*. doi: 10.2514/6.2013-5164.

Sugar Gabor, O., Koreanschi, A. & Botez, R. M. (2013c). An efficient numerical lifting line method for practical wing optimization through morphing on the hydra technologies UAS-S4. 30.

Sugar Gabor, O., Koreanschi, A. & Botez, R. M. (2015). Numerical study of UAS-S4 Éhecatl aerodynamic performance improvement obtained with the use of a morphing wing approach. *33rd AIAA Applied Aerodynamics Conference, AIAA AVIATION Forum, Dallas, TX, USA*. doi: 10.2514/6.2015-2259.

Sugar Gabor, O., Koreanschi, A. & Botez, R. M. (2016). A new non-linear vortex lattice method: Applications to wing aerodynamic optimizations. *Chinese Journal of Aeronautics*, 29(5), 1178–1195.

Takenaka, K., Hatanaka, K., Yamazaki, W. & Nakahashi, K. (2008). Multidisciplinary design exploration for a winglet. *Journal of Aircraft*, 45(5), 1601.

Thill, C., Etches, J., Bond, I., Potter, K. & Weaver, P. (2008). Morphing skins. *The Aeronautical Journal*, 112(1129), 117–139.

Torenbeek, E. (2013). *Advanced aircraft design: Conceptual design, technology and optimization of subsonic civil airplanes*. John Wiley & Sons.

Versteeg, H. K. & Malalasekera, W. (2007). *An introduction to computational fluid dynamics: the finite volume method*. Pearson Education.

Von Kármán, T. (2004). *Aerodynamics: selected topics in the light of their historical development*. Courier Corporation.

Wallin, S. (2000). *Engineering turbulence modelling for CFD with focus on explicit algebraic Reynolds stress models*. Royal Institute of Technology, Department of Mechanics.

Wang, W. (2016). *High-dimensional Covariance Learning*. (Ph. D. thesis, Princeton University).

Weisshaar, T. A. (2013). Morphing aircraft systems: historical perspectives and future challenges. *Journal of Aircraft*, 50(2), 337-353. doi: 10.2514/1.C031456.

Whitcomb, R. T. (1976). A design approach and selected wind tunnel results at high subsonic speeds for wing-tip mounted winglets. *NASA TN D-8260*.

Whitcomb, R. T. (1981). Methods for reducing aerodynamic drag. *NASA Conference Publication*, 2211, 10–13.

Wilcox, D. C. (1998). *Turbulence modeling for CFD*. DCW Industries, La Canada, CA.

Williams, C. K. & Rasmussen, C. E. (1996). Gaussian processes for regression. *Advances in neural information processing systems*, pp. 514–520.

Yokozeki, T., Sugiura, A. & Hirano, Y. (2014). Development of variable camber morphing airfoil using corrugated structure. *Journal of Aircraft*, 51(3), 1023–1029. doi: 10.2514/1.C032573.

Zhang, P., Zhou, L., Cheng, W. & Qiu, T. (2014). Conceptual design and experimental demonstration of a distributedly actuated morphing wing. *Journal of Aircraft*, 52(2), 452–461. doi: 10.2514/1.C032739.